FINAL REPORT

Cost-Effective Destruction of Per- and Polyfluoroalkyl Substances from DoD Subsurface Investigation-Derived Wastes Using a New Class of Adsorptive Photocatalysts

SERDP Project ER18-1515

APRIL 2020

Dongye (Don) Zhao
Auburn University

Distribution Statement A
This document has been cleared for public release

SERDP
DOD ▪ EPA ▪ DOE

Page Intentionally Left Blank

This report was prepared under contract to the Department of Defense Strategic Environmental Research and Development Program (SERDP). The publication of this report does not indicate endorsement by the Department of Defense, nor should the contents be construed as reflecting the official policy or position of the Department of Defense. Reference herein to any specific commercial product, process, or service by trade name, trademark, manufacturer, or otherwise, does not necessarily constitute or imply its endorsement, recommendation, or favoring by the Department of Defense.

Page Intentionally Left Blank

REPORT DOCUMENTATION PAGE

Form Approved
OMB No. 0704-0188

Public reporting burden for this collection of information is estimated to average 1 hour per response, including the time for reviewing instructions, searching existing data sources, gathering and maintaining the data needed, and completing and reviewing this collection of information. Send comments regarding this burden estimate or any other aspect of this collection of information, including suggestions for reducing this burden to Department of Defense, Washington Headquarters Services, Directorate for Information Operations and Reports (0704-0188), 1215 Jefferson Davis Highway, Suite 1204, Arlington, VA 22202-4302. Respondents should be aware that notwithstanding any other provision of law, no person shall be subject to any penalty for failing to comply with a collection of information if it does not display a currently valid OMB control number. **PLEASE DO NOT RETURN YOUR FORM TO THE ABOVE ADDRESS.**

1. REPORT DATE ***(DD-MM-YYYY)*** 21-4-2020	**2. REPORT TYPE** SERDP Final Report	**3. DATES COVERED** ***(From - To)*** 05/17/2018 – 05-17-2020
4. TITLE AND SUBTITLE Cost-effective destruction of per- and polyfluoroalkyl substances from DoD subsurface investigation-derived wastes using a new class of adsorptive photocatalysts		**5a. CONTRACT NUMBER** 18-C-0063 **5b. GRANT NUMBER** **5c. PROGRAM ELEMENT NUMBER**
6. AUTHOR(S) Dongye (Don) Zhao		**5d. PROJECT NUMBER** ER18-1515 **5e. TASK NUMBER** **5f. WORK UNIT NUMBER**
7. PERFORMING ORGANIZATION NAME(S) AND ADDRESS(ES) AND ADDRESS(ES) Auburn University, 107 Samford Hall, Auburn, AL 36849		**8. PERFORMING ORGANIZATION REPORT NUMBER** ER18-1515
9. SPONSORING / MONITORING AGENCY NAME(S) AND ADDRESS(ES) Strategic Environmental Research and Development Program 4800 Mark Center Drive Suite 16F16 Alexandria, VA 22350-3605		**10. SPONSOR/MONITOR'S ACRONYM(S)** SERDP **11. SPONSOR/MONITOR'S REPORT NUMBER(S)** ER18-1515

12. DISTRIBUTION / AVAILABILITY STATEMENT
DISTRIBUTION STATEMENT A. Approved for public release: distribution unlimited.

13. SUPPLEMENTARY NOTES

14. ABSTRACT

The overall goal of this SEED project was to develop an innovative "Concentrate-&-Destroy" technology for cost-effective degradation of PFAS from DoD's subsurface investigation-derived wastes. The key findings are: 1) three novel adsorptive photocatalysts were synthesized, characterized and tested based on commercially available low-cost materials; 2) The new materials not only offer superior adsorption rate and capacity for PFAS (PFOA and PFOS), but also great photocatalytic degradation and mineralization efficiency; 3) The *in situ* efficient photodegradation of PFAS also regenerates the materials, allowing for repeated uses of the photocatalysts without chemical regeneration; and 4) Dilute Corexit EC9500A can serve as an effective, environmentally safe extractant for removing PFAS from soil. Based on the compelling preliminary findings, more in-depth follow on studies are warranted to further optimize the new materials and to test the technology under DoD field conditions.

15. SUBJECT TERMS
PFAS, Aqueous film forming foam, Groundwater contamination, Groundwater remediation, PFOA, PFOS, Remediation

16. SECURITY CLASSIFICATION OF:			**17. LIMITATION OF ABSTRACT**	**18. NUMBER OF PAGES**	**19a. NAME OF RESPONSIBLE PERSON**
					Dongye (Don) Zhao
a. REPORT UNCLASS	**b. ABSTRACT** UNCLASS	**c. THIS PAGE** **UNCLASS**	UNCLASS	127	**19b. TELEPHONE NUMBER** ***(include area code)*** 334-844-6277

Standard Form 298 (Rev. 8-98)
Prescribed by ANSI Std. Z39.18

Page Intentionally Left Blank

Table of Contents

Table of Contents i
List of Tables iv
List of Figures v
List of Acronyms viii
Keywords xi
Acknowledgements xii
Abstract 1
Executive Summary 3
1. Objectives 13
2. Background 14
2.1. Environmental issues with PFAS 14
2.2. The state of the technology 15
2.3. The proposed technology 16
3. Materials and Methods 18
3.1. General Technical Approach 18
3.2. Materials and Methods: Fe/TNTs@AC 19
3.2.1. Chemicals and materials 19
3.2.2. Synthesis of Fe/TNTs@AC 19
3.2.3. Characterization of Fe/TNTs@AC 20
3.2.4. Adsorption kinetic and isotherm tests 20
3.2.5. Photodegradation kinetic tests 21
3.2.6. Effect of environmental factors on photodegradation of PFOA by Fe/TNTs@AC and preliminary test of removal PFOS from field groundwater by Fe/TNTs@AC 21
3.2.7. Density functional theory calculations 22
3.3. Materials and Methods: Ga/TNTs@AC 22
3.3.1. Chemicals and materials 22
3.3.2. Synthesis of Ga/TNTs@AC 22
3.3.3. Adsorption and subsequent photodegradation of PFOS by Ga/TNTs@AC 23
3.4. Materials and Methods: FeO@CS 23
3.4.1. Chemicals and materials 23
3.4.2. Synthesis and characterization of FeO/CS 23

3.4.3. Characterization of FeO/CS 24
3.4.4. Adsorption and photodegradation of PFOA by FeO/CS 24
3.4.5. DFT calculations 25
3.5. Materials and Methods: Soil Treatment 25
3.5.1. Chemicals and materials 25
3.5.2. Extraction PFAS in the field soil 26
3.5.3. Desorption and successive desorption of PFOS by oil dispersants 26
3.5.4. Re-adsorption kinetics of desorbed PFOS by Ga/TNTs@AC 27
3.5.5. Photodegradation of re-adsorbed PFOS by Ga/TNTs@AC and re-use of treated dispersant solution 27
3.6. Analytical Methods 27
4. Results and Discussion 30
4.1. Results and Discussion: Fe/TNTs@AC 30
4.1.1. Synthesis and characterization of Fe/TNTs@AC 30
4.1.2. Effects of calcination temperature and Fe content on photoactivity of Fe/TNTs@AC 35
4.1.3. Adsorption and photodegradation of PFOA and PFOS by Fe/TNTs@AC 37
4.1.4. Reusability of Fe/TNTs@AC 39
4.1.5. Mechanisms for enhanced adsorption and photodegradation of PFAS by Fe/TNTs@AC 40
4.1.6. Effects of DOM and ionic strength on PFOA photodegradation 43
4.1.7. Effect of temperature on PFOA photodegradation by Fe/TNTs@AC 44
4.1.8. Effect of material dosage on PFOA photodegradation by Fe/TNTs@AC 45
4.1.9. Preliminary test of PFOS removal from field groundwater using Fe/TNTs@AC 46
4.2. Results and Discussion: Ga/TNTs@AC 47
4.2.1. Introduction 47
4.2.2. Adsorption of PFOS by Ga/TNTs@AC 47
4.2.3. Photodegradation and defluorination kinetics of PFOS by Ga/TNTs@AC 48
4.2.4. Comparison of PFOS defluorination by Fe/TNTs@AC and Ga/TNTs@AC 49
4.3. Results and Discussion: FeO/CS 49
4.3.1. Introduction 49
4.3.2. Characterization of FeO/CS 50
4.3.3. Adsorption and photodegradation of PFOA by FeO/CS 53
4.3.4. Mechanisms for enhanced adsorption and photodegradation by FeO/CS 54

4.3.5. Role of hydroxyl radical in PFOA photodegradation by FeO/CS 60
4.3.6. Intermediate products and reaction pathway in PFOA photodegradation by FeO/CS 62
4.4. Results and Discussion: Soil Treatment 64
4.4.1. Extraction of PFAS from the Willow Grove field soil 64
4.4.2. Batch desorption and successive desorption of PFOS from Willow Grove soil 64
4.4.3. Re-adsorption of desorbed PFOS by Ga/TNTs@AC 68
4.4.4. Photodegradation of re-adsorbed PFOS by Ga/TNTs@AC 69
4.5. Preliminary Process Design and Cost Analysis 71
4.5.1. Costs for Fe/TNTs@AC synthesis 72
4.5.2. Costs for PFOA adsorption 73
4.5.3 Costs for photocatalytic degradation/destruction of PFOA 77
5. Conclusions and Implications for Future Research 80
6. Literature Cited 82
7. Appendices.....89
7.1. Publications and Presentations 89
7.2. Supporting QA/QC Data 92
7.3. Data Used in Various Figures Related to PFOA, PFOS and F^- Concentrations. 95

List of Tables

Table 1. Atomic compositions of Fe/TNTs@AC. **32**
Table 2. XRD pattern powder diffraction file (PDF) number. **33**
Table 3. Surface atomic percentage of AC and TNTs@AC obtained by XPS. **34**
Table 4. Concentrations of PFOA and PFOS in the soil of the Willow Grove site. **64**
Table 5. Characteristics of surfactant compositions in the oil dispersant Corexit EC9500A. **67**
Table 6. Estimated costs of raw materials for synthesizing 1 kg of Fe/TNTs@AC. **72**
Table 7. Itemized capital costs for the adorpion of PFOA using Fe/TNTs@AC. **75**
Table 8. Cost breakdowns for operating labor costs. **76**
Table 9. Summary of itemized operating costs per 1,000 gal of water treated by adsorption. **77**
Table 10. Capital cost breakdowns for the photodegradation system. **78**

List of Figures

Figure 1. Left: Core-shell structure of activated charcoal supported titanate nanotubes (TNTs@AC); Right: HRTEM images of TNT nanotubes on AC **17**

Figure 2. Schematic of the "Concentrate-&-Destroy" concept for removal and destruction of PFAS in water **17**

Figure 3. Schematic for treating PFAS in IDW soil **17**

Figure 4. Flow chart of the research approach and tasks **18**

Figure 5. Synthesis of a novel adsorptive photocatalysts, Fe/TNTs@AC based on commercial activated carbon and TiO_2 with Fe impregnation **19**

Figure 6. Synthesis of Ga/TNTs@AC via an alkaline hydrothermal approach **22**

Figure 7. Synthesis of FeO/CS via a modified one-step hydrothermal method and illustration of the potential use for adsorption and photocatalytic degradation of PFAS under solar light **23**

Figure 8. **(a)** A digital image of Fe/TNTs@AC prepared based on commercial activated carbon (AC) and TiO_2 through an alkaline hydrothermal process (AC:TiO_2 mass ratio = 1:1, Fe = 1 wt.% of TNTs@AC); **(b)** TEM images of nanoscale AC particles attached on titanate nanotubes (TNTs); and **(c)** and **(d)** Close-up TEM images of iron- and AC-modified TNTs with FeO patched on TNTs **31**

Figure 9. SEM image of **(a)** TNTs@AC and **(b)** Fe/TNTs@AC; and EDS spectra of (c) Fe/TNTs@AC **31**

Figure 10. SEM-EDS mapping of the elements of Fe/TNTs@AC **32**

Figure 11. **(a)** XRD patterns of F-400 GAC, TNTs@AC, and Fe/TNTs@AC calcined at 550 ºC; and **(b)** High resolution TEM images of TNTs and iron oxide crystals of Fe/TNTs@AC calcined at 550 ºC **33**

Figure 12. XPS spectra of Fe/TNTs@AC: **(a)** Survey XPS, and **(b)** high resolution of Fe 2p ... **34**

Figure 13. (a) N_2 adsorption-desorption isotherms, and **(b)** pore size distributions of unmodified TNTs@AC and Fe/TNTs@AC. V: Pore volume, and D: pore diameter **35**

Figure 14. Defluorination of PFOA by Fe/TNTs@AC with **(a)** different calcination temperatures, and **(b)** various Fe contents **36**

Figure 15. **(a)** Adsorption, **(b)** photodegradation, and **(c)** defluorination kinetics of PFOA by Fe/TNTs@AC **37**

Figure 16. **(a)** Adsorption, **(b)** photodegradation, and **(c)** defluorination kinetics of PFOS by Fe/TNTs@AC **38**

Figure 17. Adsorption isotherm of PFOA by Fe/TNTs@AC **39**

Figure 18. Reusing Fe/TNTs@AC in six consecutive cycles of adsorption-photodegradation of PFOA **39**

Figure 19. A LC-QTOF-MS chromatogram showing intermediate products during

photodegradation of PFOA by Fe/TNTs@AC **40**

Figure 20. Conceptualized illustration of PFOA adsorption by TNTs@AC and Fe/TNTs@AC: vertical versus parallel adsorption of PFOA. Carbon nanoparticles interact with the tail, and iron oxide nanoparticles attract the head groups, setting up for subsequent photodegradation **42**

Figure 21. **(a)** PFOA, **(b)** Fe(III) dimer, **(c)** mono-dentate complexation, and **(d)** bi-dentate complexation with optimized geometries calculated at B3LYP/6−311+G(d,p) level of theory **43**

Figure 22. Effects of **(a)** dissolved organic matters (DOM) and **(b)** ionic strength (NaCl or $CaCl_2$) on PFOA photodegradation using Fe/TNTs@AC **44**

Figure 23. Effects of temperature on PFOA photodegradation using Fe/TNTs@AC **45**

Figure 24. Effect of material dosage on the mineralization of PFOA using Fe/TNTs@AC **46**

Figure 25. Adsorption and photodegradation of PFOS from the Willow Grove groundwater using Fe/TNTs@AC **47**

Figure 26. **(a)** Ga/TNTs@AC prepared based on commercial AC and TiO_2 (AC:TiO_2 mass ratio = 1:1, Ga = 2 wt.% of TNTs@AC); **(b)** Adsorption kinetics of PFOS by Ga/TNTs@AC **48**

Figure 27. Photodagradation **(a)** and defluorination **(b)** of PFOS by Ga/TNTs@AC **48**

Figure 28. Defluorination of PFOS by Fe/TNTs@AC and Ga/TNTs@AC **49**

Figure 29. SEM **(a, e, i)**, TEM **(b, f)**, HRTEM **(c, g)**, FFT **(d, h)** patterns of neat FeO, FeO/CS(1:1) and neat CS; and EDS elemental mapping **(g)** of FeO/CS(1:1) **51**

Figure 30. XRD patterns of neat CS, FeO, and FeO/CS prepared at various Fe/C molar ratios . **52**

Figure 31. FTIR patterns of synthetic neat FeO, CS and FeO/CS at various Fe/C molar ratios . **52**

Figure 32. UV-vis DRS patterns of prepared neat FeO, CS and FeO/CS at various Fe/C molar ratios **53**

Figure 33. Equilibrium adsorption of PFOA and subsequent photodegradation after 4 h of solar light exposure **(a)**, and defluorination kinetics **(b)** of PFOA by neat CS, FeO and FeO/CS at various Fe/C molar ratios (indicated in the brackets) **54**

Figure 34. FTIR patterns of FeO/CS **(a)** and neat FeO **(b)** after adsorption of PFOA **55**

Figure 35. The O1s XPS patterns of FeO/CS **(a)**, and Fe 2p XPS patterns of FeO/CS **(b)** and neat FeO **(c)** before and after adsorption and photodegradation of PFOA **55**

Figure 36.The Fe 2p XPS spectra of fresh and solar light irradiated FeO/CS(1:1) in the absence of PFOA **56**

Figure 37. F1 s XPS patterns of FeO/CS **(a)** and Fe_2O_3 **(b)** before and after adsorption or photodegradation of PFOA **57**

Figure 38. Calculated iron atom structures of ferrihydrite **(a)** and hematite **(b)**. Blue: Fe; Red: O; Light grey: H **58**

Figure 39. The density of states of PFOA-loaded hematite and ferrihydrite **59**

Figure 40. Molecular orbitals and electron distributions of PFOA. Green: negative phase; Purple: positive phase; Light blue: F; Dark grey: C; Red: O; and light grey: H; HOMO: the highest occupied molecule orbital; and LUMO: the lowest un-occupied molecular orbital **59**

Figure 41. Comparing energy levels of the highest occupied molecule orbital (HOMO) and the lowest un-occupied molecular orbital (LUMO) of PFOA adsorbed on Fh and Ht with energy levels of valence band (VB) and conduction band (CB). The smaller band gap between the respective HOMO and VB or LUMO and CB is more conducive to electron transfer from PFOA to the photocatalysts **59**

Figure 42. **(a)** The charge density difference of PFOA-laden hematite; and **(c)** The charge density difference of PFOA-laden ferrihydrite. The yellow and blue iso-surfaces represent charge accumulation and depletion in the space, respectively **60**

Figure 43. PFOA removal rate in the FeO/CS with or without isopropyl alcohol (ISA) **61**

Figure 44. Electron paramagnetic resonance (EPR) spectra of DMPO–•OH adducts produced by FeO/CS(1:1) under air **(a)** or Ar **(b)** after solar light irradiation for 20 min **61**

Figure 45. The iso-surface plots of frontier orbitals of $C_7F_{15}^{\bullet}$ when combined with $^{\bullet}OH$ or H_2O, change in Gibbs free energy and calculated reaction enthalpy change for $C_7F_{15}OH$ production induced by $^{\bullet}OH$ or H_2O possible pathway of PFOA degradation **62**

Figure 46. ESI/MS spectra of the ion peaks assigned as by-products of PFOA photodegradation by FeO/CS(1:1) **(a)** and neat FeO **(b)** after 4 h of simulated solar light irradiation..... **63**

Figure 47. Proposed pathway for photocatalytic degradation of PFOA by FeO/CS **64**

Figure 48. Batch equilibrium desorption of PFOS from the Willow Grove Soil using two common oil dispersants (Corexit EC9500A and SPC1000) at various concentrations and with or without NaCl **65**

Figure 49. Successive desorption of PFOS from the Willow Grove soil using Corexit EC9500A dispersant solution **66**

Figure 50. Re-adsorption of desorbed PFOS by 2%-Ga/TNTs@AC **68**

Figure 51. Equilibrium desorption of PFOS from the Willow Grove soil using fresh or recycled Corexit EC9500A **69**

Figure 52. Degradation and defluorination of desorbed PFOS using Ga/TNTs@AC (Ga = 2 wt.%) **70**

Figure 53. A conceptualized schematic diagram of the "Concentrate & Destroy" process for adsorption and destruction of PFAS in IDW water **71**

List of Acronyms

AC	Activated carbon
AFFF	Aqueous film forming foam
BET	Brunauer-Emmett-Teller
BJH	Barret-Joyner-Halender
CB	Conduction band
CMC	Critical micelle concentration
CS	Carbon sphere
DFT	Density functional theory
DI	Deionized
DoD	Department of Defense
DOM	Dissolved organic matter
DOS	Density of states
DRS	Diffuse reflectance spectra
EDS	Energy dispersive spectra
EPR	Electron paramagnetic resonance spectroscopy
FeO/CS	Iron oxide/carbon sphere
FeO	Iron oxide
Fe/TNTs@AC	Iron doped activated carbon modified titanate nanotubes
Fh	Ferrihydrite
FTIR	Fourier-transform infrared spectroscopy
Ga/TNTs@AC	Gallium doped activated carbon modified titanate nanotubes
GAC	Granular activated carbon
HA	Humic acid
HDPE	High-density polypropylene
HOMO	Highest occupied molecule orbital
HRT	Hydraulic residence time
Ht	Hematite
IC	Ion chromatography
IDW	Investigation-derived waste
IEFPCM	Integral Equation Formalism Polarized Continuum Model
IS	Internal standard
LC-MS/MS	Liquid chromatography-tandem mass spectrometry
LC-QTOF/MS	Liquid chromatography quadrupole time-of-flight mass spectrometer

LUMO	Lowest un-occupied molecular orbital
M4PFOA	Perfluoro-n-[1,2,3,4-^{13}C4]octanoic acid
M4PFOS	Sodium perfluoro-1-[1,2,3,4-^{13}C4]octanesulfonate
M8PFOA	Perfluoro-n-[1,2,3,4,5,6,7,8-$^{13}C_8$]octanoic acid
M8PFOS	Sodium perfluoro-1-[1,2,3,4,5,6,7,8-$^{13}C_8$]octanesulfonate
MCL	Maximum Contaminant Level
NOM	Natural organic matter
PAC	Powder activated carbon
PAH	Polycyclic aromatic hydrocarbon
PAW	Projector-augmented wave
PBE	Perdew-Burke-Ernzerh
PDF	Powder diffraction file powder diffraction file
PES	Poly (ether sulfones)
PFAS	Per- and polyfluoroalkyl substances
PFBA	Perfluorobutanoic acid
PFCA	Perfluorinated carboxylic acid
PFSA	Perfluorosulfonic Acid
PFHpA	Perfluoroheptanoic acid
PFHxA	Perfluorohexanoic acid
PFHxS	Perfluorohexane sulfonate
PFOA	Perfluorooctanoic acid
PFOS	Perfluorooctane sulfonate
PFPA	Perfluorophosphonic acid
PFPeA	Perfluoropentanoic acid
PZC	Point of zero charge
QA	Quality assurance
QC	Quality control
RPM	Remedial Project Manager
ROS	Reactive oxygen species
RT	Retention time
SEM	Scanning electron microscope
SOP	Standard operating procedure
SPE	Solid phase extraction
TEM	Transmission electron microscopy
TCE	Trichloroethylene

TFA	Trifluoroacetic acid
TNTs	Titanate nanotubes
TNTs@AC	Activated carbon modified titanate nanotubes
TOC	Total organic carbon
UCMR	Unregulated Contaminant Monitoring Rule
UV	Ultraviolet
VB	Valence band
WWTPs	Wastewater treatment plants
XPS	X-ray photoelectron spectroscopy
XRD	X-ray diffractometer

Keywords

Activated carbon
Adsorbent
Adsorption
AFFF
Aqueous film forming foam
Catalysis
Catalyst
Composite material
Concentrate and destroy
Defluorination
Degradation
Desorption
Dispersant
Extraction
Firefighting foam
Groundwater contamination
Groundwater remediation
Investigation derived waste
Iron oxide
Dispersant
Per- and polyfluoroalkyl substance
Perfluorooctanoic acid
Perfluorooctane sulfonate
Persistent organic pollutant
PFAS
PFOA
PFOS
Photocatalysis
Photocatalyst
Photodegradation
Remediation
Soil contamination
Soil remediation
Soil washing
Surfactant
Titanate nanotube
Water quality
Water treatment

Acknowledgements

This work was performed under contract with the U.S. Department of Defense - Strategic Environmental Research and Development Program (SERDP) (ER18-1515). We are grateful to the Program Manager Dr. Andrea Leeson and Ms. Cara Patton for their technical advice and administrative assistances. We would also like to express our gratitude to the SERDP/ESTCP team Dr. Janice Willey, Mr. Jason Speicher, and Ms. Amy Maples for their guidance and assistances on various occasions.

We would thank Dr. Melissa Boersma, Director of the Mass Spectrometry Lab in the Department of Chemistry and Biochemistry of Auburn University, for her dedication and hardworking on the analysis of PFAS involved in this study. Likewise, we would like to thank Dr. Lee Blaney and Dr. Ke He of University of Maryland, Baltimore County, for their help with analyzing the PFAS using LC-MS/MS and developing the associated standard operating procedures.

Last but not least, I would thank all the postdocs and graduate students involved in this work for their sacrifice and day-to-day hard working on this project, in particular, I am indebted to Dr. Tianyuan Xu, Dr. Zongsu Wei, Mr. Fan Li, Mr. Jun Duan, and Ms. Yangmo Zhu, without whom we would not have accomplished so much.

Abstract

Introduction and Objectives. As DoD has been performing various related investigations, large quantities of investigation-derived wastes (IDWs) are and continue to be generated. Yet, a cost-effective technology has been lacking for treatment of per- and polyfluoroalkyl substances (PFAS) in contaminated soil and water including the IDWs. As such, SERDP has been looking for "destructive technologies" "to minimize potential future environmental liability" and to replace current costly practices (landfill and incineration). The overall goal of this SEED project was to develop an innovative "Concentrate-&-Destroy" technology for cost-effective degradation of PFAS from DoD's IDWs (including both water and soil). The specific objectives were to: **1)** Develop a new class of adsorptive photocatalysts, which can facilitate effective adsorption and subsequent in situ photocatalytic degradation of PFAS; **2)** Test the effectiveness and reusability of the new materials for selective adsorption and photocatalytic degradation of PFAS in water without chemical regeneration; and **3)** Develop a new strategy to remove and degrade PFAS from soil.

Technical Approach. The objectives were achieved by carrying out the following research tasks: **1)** Synthesize a series of novel metal-doped, carbon-modified photocatalysts based on commercially available low-cost activated carbon (AC) and photocatalysts; **2)** Test the adsorption rates and capacities of the materials with perfluorooctanoic acid (PFOA) and perfluorooctane sulfonate (PFOS) as model PFAS; **3)** Test the photodegradation rates and extents of the pre-concentrated PFAS, and the material reusability without chemical regeneration; **4)** Examine the effectiveness of low-cost dispersants for "greener" and cost-effective removal of PFAS from soil, and **5)** Conduct a preliminary cost-benefit analysis.

Results. For the first time, we synthesized, characterized and tested three most promising adsorptive photocatalysts, including two AC-supported, metal-doped titanate nanotubes (Fe/TNTs@AC and Ga/TNTs@AC), and a composite carbon sphere (CS) modified iron oxide (FeO/CS). All three materials were able to rapidly (<10 min) and nearly completely adsorb PFOA and PFOS. Subsequently, when subjected to UV, Fe/TNTs@AC was able to photodegrade >90% of the pre-concentrated PFOA and >88% of PFOS within 4 h, of which ~62% (PFOA) and ~46% (PFOS) were completely defluorinated (or mineralized). Even more efficient degradation was observed with Ga/TNTs@AC, which was able to pre-concentrate all PFOS within 10 min and mineralize 66% of the pre-concentrated PFOS under UV within 4 h. FeO/CS mineralized 60% PFOA under *solar light* within 4 h. Upon the photodegradation, the materials can be reused in multiple cycles without chemical regeneration. For instance, after repeatedly used for 6 cycles for PFOA removal, Fe/TNTs@AC did not show significant drop in both adsorption capacity and photocatalytic activity. For treatment of a PFAS-laden field soil from the Willow Grove site, we developed a "green" and cost-effective desorption technique to efficiently elute PFAS from the soil by using a low-cost oil dispersant (Corexit EC9500A). Subsequently, the desorbed PFOS in the spent dispersant was reloaded on the composite material and degraded under UV.

Benefits. The on-site "Concentrate-&-Destroy" technique represents a significant advancement of current practices (adsorption, ion exchange, landfill and incineration) for treating PFAS in IDWs or PFAS-contaminated water and soil at large. Upon further testing and polishing (especially under DoD field conditions), the technology will arm DoD remedial project managers with a more cost-effective technology for handling and disposal of PFAS-laden IDWs and FPAS contaminated soil and groundwater at DoD sites.

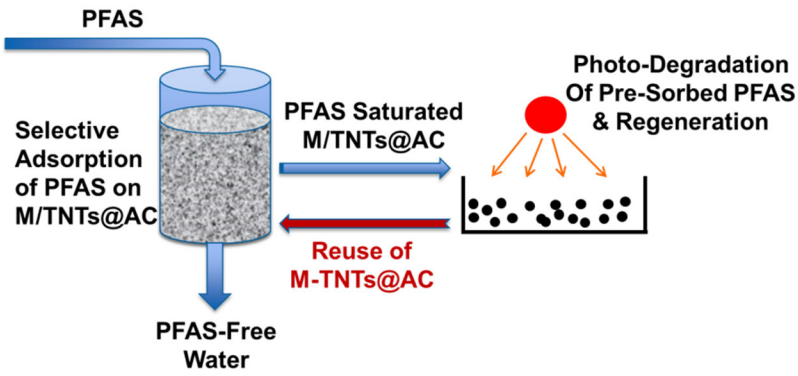

Graphic depiction of the "Concentrate-&-Destroy" technology for real-world utilization.

Executive Summary

Introduction

Environmental issues with PFAS. Per- and polyfluoroalkyl substances (PFAS) have become a class of important contaminants in soil and water due to their wide-spread applications, resistance to environmental degradation, and potential health effects. Perfluorooctanoic acid (PFOA) and perfluorooctane sulfonate (PFOS) are the most detected PFAS. To mitigate human exposure, EPA established a lifetime health advisory level of 70 ng L^{-1} for combined PFOA and PFOS in drinking water in 2016. A recent survey reported that drinking water supplies for 6 million U.S. residents exceeded the advisory level.

Human exposure to PFAS has been linked to cancer, elevated cholesterol, obesity, immune suppression, and endocrine disruption. Health concerns in the early 2000s prompted manufacturers in Europe and North America to phase out production of some long-chain PFAS.

The EPA's third Unregulated Contaminant Monitoring Rule (UCMR 3) requires close monitoring of PFAS. In addition to the EPA health advisory, EPA unveiled a PFAS Action Plan that will move forward with the Maximum Contaminant Level (MCL) process for PFOA and PFOS. As part of the Action Plan, U.S. EPA will continue their enforcement actions and clarify clean up strategies, and expand monitoring of PFAS in the environment. Meanwhile, many states have initiated stringent drinking water standards on PFAS.

Aqueous film-forming foams (AFFFs) have been a vital tool to fight large hydrocarbon fires. Due to their surface-tension lowering properties, fluorinated surfactants are often added in the formulations to enhance their firefighting capabilities. Historical reports of uncontrolled spills and repeated uses of AFFFs during fire training and for AFFF performance testing have been correlated with elevated concentrations of PFAS in biota, surface water, or groundwater.

AFFF formulations have been used by DoD since the 1970s, and the military use accounted for 75% of the U.S. market. Consequently, hundreds of the military sites have been contaminated with PFAS. Groundwater at sites impacted by AFFF uses has the greatest recorded concentrations of PFAS of any aqueous environment. The vast majority of the AFFF formulations used by DoD contain PFOS and related perfluoroalkyl sulfonates such as perfluorohexane sulfonate (PFHxS). As a result, the use of PFOS-based AFFFs has been a major environmental liability of DoD.

In the last decade or so, DoD has been increasingly investigating the extent of PFAS contamination across its portfolio of sites. Consequently, large quantities of investigation-derived wastes (IDWs) were (and will continue to be) generated. Yet, cost-effective technologies are lacking to treat the IDWs including both PFAS-laden water and soil. To a large extent, current practices rely on landfilling and incineration of these wastes, which are both costly and pose additional transportation requirements and secondary contamination issues. As such, SERDP has been looking for "alternative innovative technologies that would permit unrestricted disposal, discharge, and/or reuse of IDW on-site".

The state of the technology. Due to the strongly polarized carbon–fluorine bonds and the amphiphilic nature, PFAS are uniquely persistent (biological half-life = ~3 years), mobile, bio-accumulative in the environment. Conventional treatment technologies are not effective for degrading PFAS, such as standard biological, Fenton and photochemical processes. Numerous studies have examined remediation methods for treatment of PFASs (mainly PFOA and PFOS). Yet, cost-effective technologies remain lacking. Sorption has been one of the most cited methods to remove PFAS, and various adsorbents have been investigated, including AC, carbon nanotubes,

ion exchange resins, synthetic magnetite nanoparticles and biomaterials. However, these adsorbents bear with some critical drawbacks, such as low adsorption capacity, high material cost, costly regeneration, and/or generation of large volumes of process waste residuals. For instances, AC has been tested/used at several sites to remove PFOA and PFOS from contaminated water; however, the cost-effectiveness of AC systems remains questionable due to costly regeneration and disposal of the spent regenerant. Moreover, while adsorption concentrates PFAS, it does do not degrade them.

Past efforts to induce photochemical transformations of PFASs employed persulfate ions ($S_2O_8^{2-}$) or TiO_2 particles as sensitizers, but the reactions are very slow. For instance, degradation of PFOA using $S_2O_8^{2-}$ as a sensitizer was found slow and costly due to the large amount of $S_2O_8^{2-}$ required and because persulfate activation is energy demanding. Sonochemical oxidation was also studied, but it is energy-demanding and its feasibility has not been tested under realistic field conditions.

Treating PFAS-bearing IDW soil is even more challenging because the soil-sorbed PFAS are not directly accessible. For typical IDW soil, the conventional disposal methods have been landfill (upon proper treatment and permission), containment, or incineration. With the rapidly mounting environmental regulations, however, landfill/containment of IDW is facing growing challenges, whereas incineration is cost-inhibitive. In fact, many common soil remediation techniques are ineffective for treating PFAS contaminated soil, including air sparging, soil-vapor extraction, bioremediation, and hydrolysis.

For soil remediation, in situ soil flushing or soil washing using a flushing agent has been often practiced. For instance, anionic surfactant (SDBS) has been used to desorb soil-sorbed chlorinated solvents. However, because desorption of PFAS is often more difficult, more aggressive solvents (e.g., methanol) were used to elute PFAS from soil or other adsorbents, which is not only costly, but environmentally prohibitive. In a prior work, the PI observed that the addition of 43.4 mg L^{-1} of SDBS increased the water solubility of PFOS by >2 times and lowered the soil adsorption by 31%. These findings suggest that low-cost and nontoxic surfactants or oil dispersants may effectively desorb PFAS from soil in a more cost-effective and environmentally benign manner.

The proposed technology. This project aimed to develop an innovative "Concentrate-&-Destroy" technique that can highly effectively adsorb/concentrate and degrade PFAS in water. The key to this technology is to develop a new class of carbon-modified photocatalysts (Fe/TNTs@AC, Ga/TNTs@AC, and FeO/CS) that can serve as both an adsorbent and a photocatalyst. As an adsorbent, the composite materials offer not only rapid adsorption rate, but also high adsorption selectivity towards PFAS, thanks to the concurrent hydrophobic interactions (between the carbons and PFAS tails) and Lewis acid-base interactions (between metals and PFAS head groups) as well as the unique structures of the composite materials. As a photocatalyst, the materials provide superior photocatalytic activity over conventional photocatalysts (e.g., TiO_2) owing to the carbon-mediated electron transfer and enhanced generation of reactive species. **Figure A1** illustrates the core-shell structure of activated carbon (AC) supported/modified titanate nanotubes (TNTs@AC) and shows a high resolution TEM (transmission electron microscopy) image of the tubular structure of TNTs on AC.

The effective adsorption concentrates trace levels of PFAS from large volumes of contaminated water onto a small amount of the photocatalyst, facilitating subsequent photochemical destruction of PFAS in a more efficient and cost-effective manner; and the photodegradation not only destroys PFAS, but also regenerates the material, allowing for multiple

cycles of operations without invoking costly chemical/solvent regeneration or producing any process waste residuals. **Figure A2** illustrates the process schematic of the "Concentrate-&-Destroy" strategy for treating PFAS in IDW water. First, PFAS in water are concentrated on metal-doped TNTs@AC (M/TNTs@AC) via common fixed-bed adsorption; Second, the PFAS-loaded adsorptive photocatalyst is subjected to UV or solar light to destroy the pre-sorbed PFAS, which also regenerates the material; and Third, the photo-regenerated material is reused in another cycle of adsorption/photodegradation. Alternatively, the adsorption step may be conducted using the conventional mixer-settler configuration (for PAC).

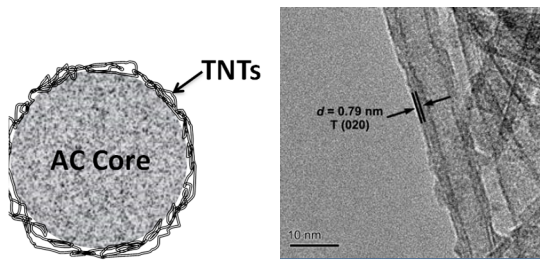

Figure A1. Left: Core-shell structure of activated charcoal supported titanate nanotubes (TNTs@AC); Right: HRTEM images of TNT nanotubes on AC.

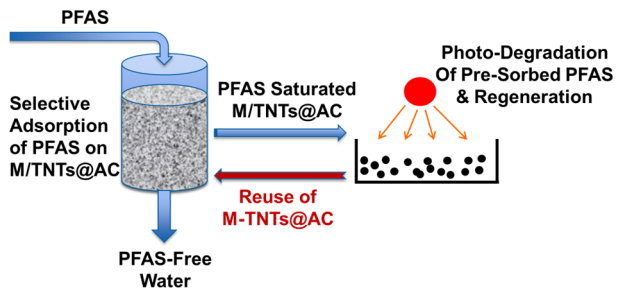

Figure A2. Schematic of the "Concentrate-&-Destroy" concept for removal and destruction of PFAS in water.

To treat PFAS in soil, we tested a novel three-step approach (desorption, concentrate and destroy). As shown in **Figure A3**, soil-sorbed PFAS are first desorbed using a dilute solution of a low-cost and nontoxic oil dispersant, known as Corexit 9500A, and the "Concentrate-&-Destroy" technique is applied to treat the PFAS in the dispersant solution. The treated dispersant solution is then reused in another desorption cycle, and the concentrated PFAS are then destroyed via the photodegradation.

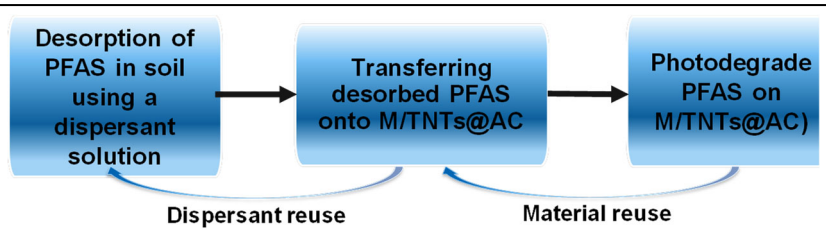

Figure A3. Schematic for treating PFAS in IDW soil.

Objectives

The overall goal of this project was to develop an innovative, cost-effective and 'green' technology for destruction of PFAS from DoD's IDWs including both PFAS-contaminated water and soil. The specific objectives were to:

1) Develop a new class of novel composite materials based on commercially available, low-cost AC, TiO_2, and CS-modified iron oxide (FeO/CS), which can offer both rapid and high-capacity adsorption and high photocatalytic degradation of PFAS;
2) Test the effectiveness of the new materials for adsorption and photocatalytic degradation of PFAS in water under UV or solar light;

3) Examine reusability of the materials for repeated adsorption and photodegradation of PFAS without chemical regeneration;
4) Explore a 'green' and cost-effective approach for eluting PFAS from IDW soil using dilute surfactants or oil dispersants;
5) Test the effectiveness of the new materials for adsorption and photodegradation of PFAS in the spent desorbing solution, and reusability of the treated solution; and
6) Carry out a preliminary cost-benefit analysis.

Technical Approach

The research objectives were accomplished by carrying out five interconnected tasks (**Figure A4**). In the screening experiments, PFOA and PFOS were used as the model PFAS, and deionized water or synthetic water was used in the water treatment tests. In addition, the material performance was preliminarily probed using groundwater from the Willow Grove site. For soil treatment (PFAS desorption), the field soil from Willow Grove was used.

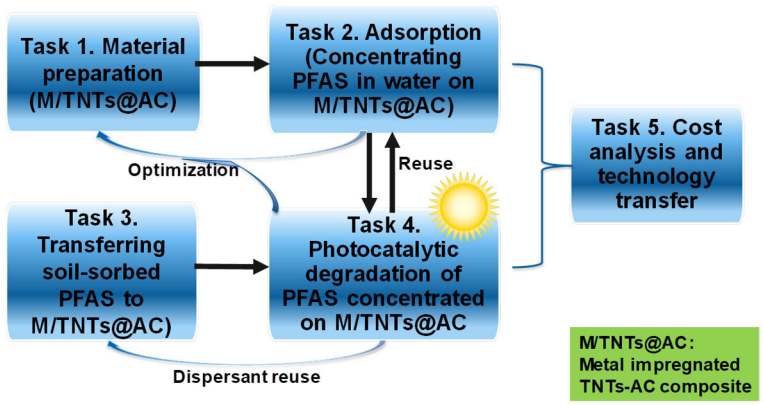

Figure A4. Flow chart of the research approach and tasks.

First, we prepared two metal-doped TNTs@AC composites (Fe/TNTs@AC and Ga/TNTs@AC) through a facile hydrothermal treatment approach by thermal impregnation of iron or gallium onto TNTs@AC. In addition, we prepared a new iron oxide/CS composite, referred to as FeO/CS, through a one-step hydrothermal treatment of Fe(III) and glucose precursors. While Fe/TNTs@AC and Ga/TNTs@AC were photoactive under UV light, FeO/CS was designed to degrade PFAS under solar light. The new adsorptive photocatalysts were then characterized with respects to morphology, particle size, surface area, elemental composition, crystal type and structure, pore size distribution, surface functional groups, element oxidation states, light absorbance, band energy gap, and zeta potential. The characterization information, along with the adsorption and photodegradation data, is then used to polish the material synthesis and elucidate the underlying adsorption and photocatalytic degradation mechanisms.

Second, we tested effectiveness of the new materials for adsorption of PFAS through batch adsorption kinetic and equilibrium experiments.

Third, for treating PFAS in soil, batch desorption tests were carried out to elute soil-sorbed PFAS using various desorbing agents (Corexit 9500A and SPC1000). Based on the screening results, Corexit 9500A was selected as the best dispersant, and PFAS in the dispersant solution was then reloaded onto the photocatalyst (Ga/TNTs@AC) and destroyed subsequently.

Fourth, photodegradation of pre-concentrated PFAS on the photocatalysts was tested in batch

reactors under UV or solar light (with 95% of water removed from the batch adsorption tests), and factors affecting the effectiveness were examined. The photo-regenerated materials were then reused in another cycle of adsorption-photodegradation to gauge reusability of the materials.

Lastly, a preliminary cost-benefit analysis was carried out.

Results and Discussion

Synthesis and characterization of Fe/TNTs@AC. Figure A5a shows the as-prepared iron-doped, AC-supported titanate nanotubes (Fe/TNTs@AC). The physical size and shape mimic those of typical powder AC, though the surface is functionalized with the photoactive Fe-doped TNTs. **Figure A5b** shows that upon the alkaline hydrothermal treatment, some carbon broke into nanoscale carbon particles that are attached on TNTs, and **Figure A5c** presents a close-up of the Fe- and carbon modified TNTs. The iron and carbon modifications are expected to enhance both adsorption and photodegradation of PFAS.

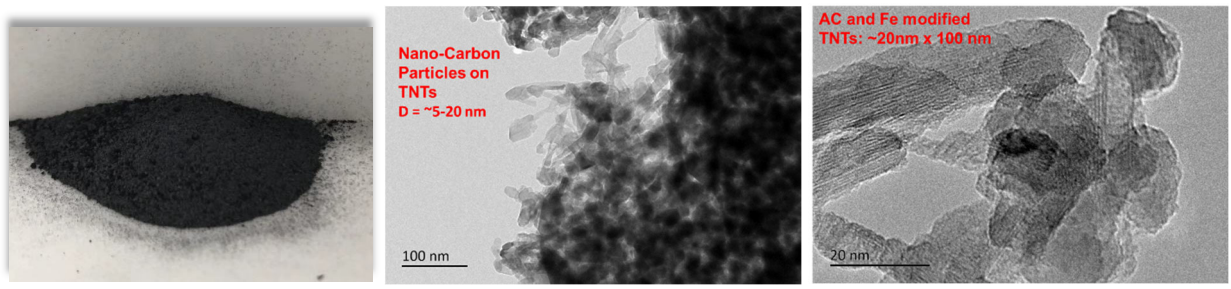

(a) **(b)** **(c)**

Figure A5. (a) A digital image of Fe/TNTs@AC prepared based on commercial activated carbon (AC) and TiO_2 through an alkaline hydrothermal process (AC:TiO_2 mass ratio = 1:1, Fe = 1 wt.% of TNTs@AC); **(b)** TEM images of nanoscale AC particles attached on titanate nanotubes (TNTs); and **(c)** A close-up of iron- and AC-modified TNTs with FeO patched on TNTs.

Adsorption and photodegradation of PFOA and PFOS by Fe/TNTs@AC. Fe/TNTs@AC exhibited excellent adsorption rate and photocatalytic activity for both PFOA and PFOS. **Figure A6a** shows adsorption kinetics of PFOA. More than 99% was adsorbed after 60 min. The rapid adsorption allows for efficient removal of PFOA from bulk water with a small hydraulic residence time (HRT) (i.e., a small reactor). Moreover, the adsorption pre-concentrates PFAS from a large volume of water onto a small volume of Fe/TNTs@AC, enabling the subsequent photocatalytic degradation to be carried out in a much smaller volume of photo-reactor with much less energy consumption compared to directly treating the bulk raw water. **Figure A6b** shows that Fe/TNTs@AC was able to highly efficiently degrade (i.e., break down into other compounds) >90% of pre-concentrated PFOA in 4 h. Moreover, **Figure A6c** shows that 62% of PFOA was completely destroyed or defluorinated (i.e., converted into F^- ions). It should be noted that in this preliminary study, the adsorption was carried out in batch reactors, where the material capacity was not fully utilized. In practice, the treatment can be further optimized. For instance, the adsorption can be performed using fixed-bed columns, which may treat much more volumes of water. Likewise, the photodegradation can be further improved by optimizing factors such as material synthesis, dosage, and reaction chemistry. PFOS has been known to be more persistent and adsorptive than PFOA. **Figure A7a** shows that Fe/TNTs@AC removed >99% of PFOS from water within just 5 min of contact time. When subjected to the UV irradiation, ~88% of preloaded PFOS was degraded within 4 h (**Figure A7b**), of which 46% was defluorinated (**Figure A7c**).

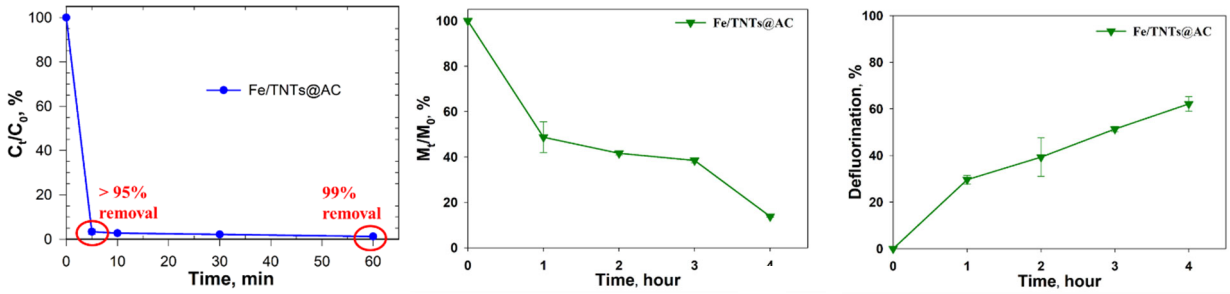

(a) **(b)** **(c)**

Figure A6. (a) Adsorption, **(b)** photodegradation, and **(c)** defluorination kinetics of PFOA by Fe/TNTs@AC. Experimental conditions: initial [PFOA] = 100 μg L^{-1}, material dosage = 1.0 g L^{-1}, solution volume = 40 mL, and pH = 7.0 ± 0.3. Photodegradation conducted under UV (λ=254 nm, 21 mW cm^2). *Degradation*: transformation or breakdown of PFAS into other compounds; *Defluorination*: conversion of fluorine into fluoride ions. M_0: initial mass of PFOA in the material, and M_t: PFOA remaining at time t.

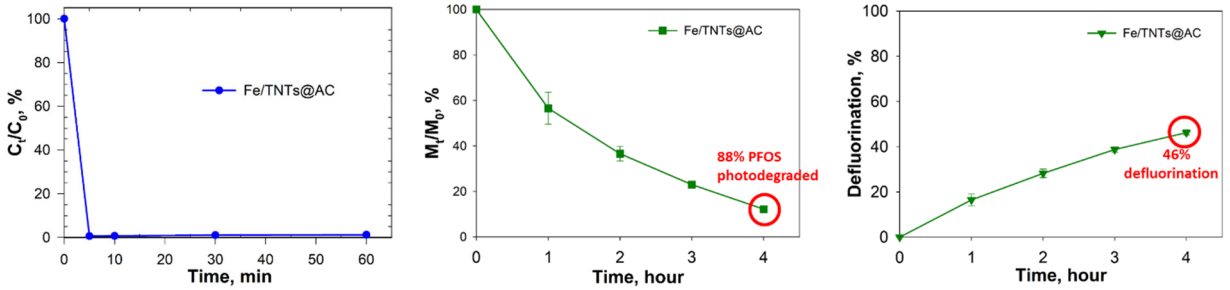

(a) **(b)** **(c)**

Figure A7. (a) Adsorption, **(b)** photodegradation, and **(c)** defluorination kinetics of PFOS by Fe/TNTs@AC. Experimental conditions: initial [PFOS] = 100 μg L^{-1}, material dosage = 2.0 g L^{-1}, solution volume = 40 mL, and pH = 7.0 ± 0.3. Photodegradation conducted under UV (λ=254 nm, 21 mW cm^{-2}).

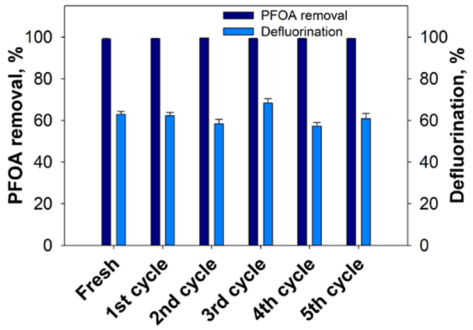

Figure A8. Reusing Fe/TNTs@AC in six consecutive cycles of adsorption-photodegradation of PFOA. Experimental conditions are the same as in Figure A6.

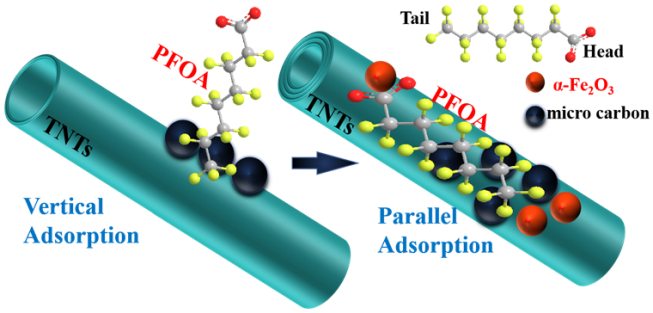

Figure A9. Conceptualized illustration of PFOA adsorption by Fe/TNTs@AC. Carbon nanoparticles interact with the tail, and FeO nanoparticles attract the head groups, setting up for subsequent photodegradation.

Reusability of Fe/TNTs@AC. Figure A8 shows that when Fe/TNTs@AC was repeatedly used in six consecutive cycles of adsorption-photodegradation without chemical regeneration, PFOA adsorption remained high (>99% removal), and defluorination kept at ~60%. Evidently,

Fe/TNTs@AC can be reused in multiple cycles without additional regeneration need. This important feature represents a great advancement of conventional adsorbents (AC or ion exchange resins), which require costly regeneration and subsequent treatment of the spent regenerant wastes. The slight increase in defluorination with the cycle time is attributed to the additional defluorination of intermediate products from the previous cycles. Indeed, short-chain PFAS were detected on Fe/TNTs@AC during the photodegradation process.

Mechanisms of enhanced PFAS adsorption and photodegradation by Fe/TNTs@AC. The adsorption rate, capacity and photocatalytic activity of Fe/TNTs@AC far exceed those of conventional Ti-based photocatalysts such as TiO_2 or TNTs. The PFOA photodegradation starts with decarboxylation of the head (COO^-) group through oxidation by the photo-generated holes (h^+), i.e.,

$$h^+(VB) + C_7F_{15}COO^- \rightarrow C_7F_{15}COO^{\bullet}, \quad C_7F_{15}COO^{\bullet} \rightarrow {}^{\bullet}C_7F_{15} + CO_2$$

The resulting ${}^{\bullet}C_7F_{15}$ radicals are decomposed via reactions with $OH^{\bullet}$ radicals and hydrolysis, resulting in cleavage of the C-F bond and release of fluoride ions. The shorter-chain products undergo the same decarboxylation/defluorination cycle, each of which eliminating one carbon and two fluorine atoms (CF_2). In addition to this standard pathway, Fe/TNTs@AC can also directly induce the decarboxylation reaction, thanks to the iron impregnation which is not only photoactive, but can directly withdraw electrons from the PFOA.

The enhanced adsorption and photodegradation are attributed to: 1) the carbon nanoparticles facilitate hydrophobic interactions with the PFOA tail, 2) the carbon coating also facilitates electron transfer and prevents electron-hole recombination in the photocatalyst, 3) the Fe(III) coating suppresses surface negative potential and enhances the interactions between the holes and the PFOA head groups (carboxylate), 4) the presence of Fe(III) also facilitates production of more ${}^{\bullet}OH$ radicals and prevents e-h recombination.

Lastly, because of the lower band energy gap of iron oxide, the Fe-doping enhances absorption of more visible light. **Figure A9** illustrates the modes of the interactions, where both the head and tail are involved in the adsorption process, resulting in a molecule orientation that is more conducive to the subsequent photocatalytic cleavage of the head groups and the C-F bonds.

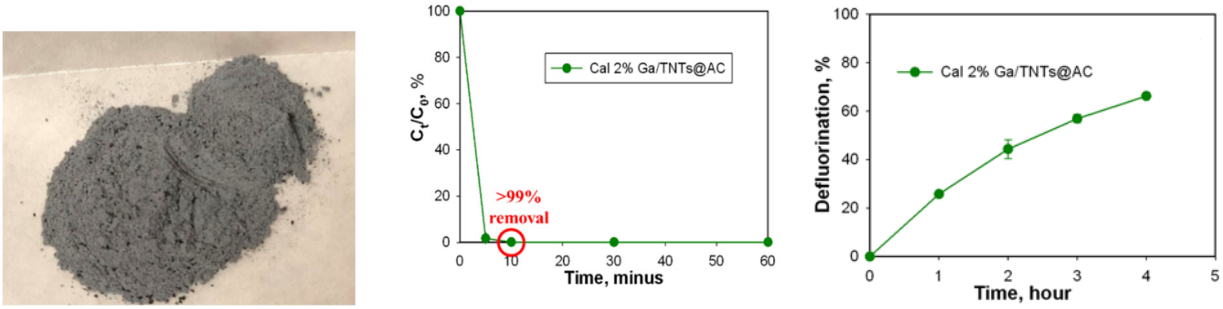

(a) **(b)** **(c)**

Figure A10. (a) Ga/TNTs@AC prepared based on commercial AC and TiO_2 (AC:TiO_2 mass ratio = 1:1, Ga = 2 wt.% of TNTs@AC); **(b)** Adsorption, and **(c)** Defluorination kinetics of PFOS by Ga/TNTs@AC. Experimental conditions: initial [PFOS] = 100 μg L^{-1}, Ga/TNTs@AC = 3.0 g L^{-1}, solution volume = 40 mL, and pH = 7.0 ± 0.3; UV: λ = 254 nm, 21 mW cm^{-2}). C_0 and C_t: PFOS Concentrations at time 0 and t, respectively.

Preparation and testing of Ga/TNTs@AC for adsorption and destruction of PFOS. In search for even more reactive photocatalysts, we prepared the gallium-doped TNTs@AC, i.e.,

Ga/TNTs@AC. **Figure A10a** shows the as-prepared powder Ga/TNTs@AC, whose size, shape and morphology resemble those of Fe/TNTs@AC. **Figure A10b** shows that Ga/TNTs@AC was able to rapidly and nearly completely remove PFOS from water, with >99% of PFOS adsorbed within 10 min. Moreover, **Figure A10c** shows that >66% of defluorination of PFOS was achieved in 4 h under UV irradiation.

Preparation and testing of FeO/CS for destruction of PFOA under solar light. Ferrihydrite (Fh) is a common mineral, which is not only 'green' and low-cost, but also has a narrow band gap energy (2.7 eV), stretching its photoactivity into the red region of the solar spectrum. On the other hand, nanoscale carbon spheres (CS) can facilitate efficient PFAS adsorption and electron transfer. Taking advantage of these properties, we prepared a new Fh-CS composite (FeO/CS), which was able to offer decent photocatalytic activity under solar light, representing significant energy saving.

Figure A11a shows scanning electron microscope (SEM) images of CS prepared without Fe and FeO/CS composite prepared at an Fe:C molar ratio of 1:1, displaying intermingled FeO and CS nanoparticles. **Figure A11b** shows that FeO/CS(1:1) and neat CS or FeO were all able to adsorb >99% of PFOA in 2 h, however, FeO/CS(1:1) showed much greater photodegradation rate than either CS or FeO alone, with 94% of the pre-adsorbed PFOA degraded in 4 h under solar light, unveiling the strong synergistic effect of FeO and CS. **Figure A11c** shows that FeO/CS(1:1) completely mineralized ~60% of PFOA (based on fluoride production) in 4 h of solar light irradiation. Increasing the Fe:C molar ratio from 0:1 to 1:1 increased photocatalytic mineralization of PFOA from almost 0 for neat FeO or CS to ~60%. Moreover, when repeatedly used for three cycles of adsorption-photodegradation, the adsorption rate and photodegradation rates remained high, though defluorination was decreased to ~50% (data not shown).

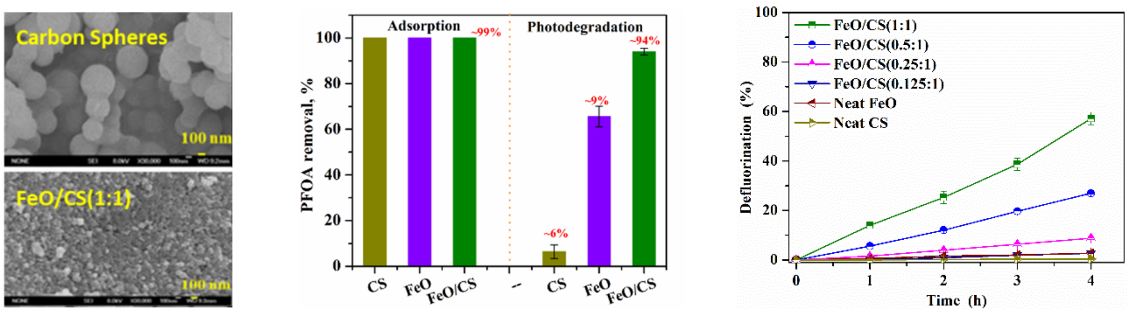

(a) **(b)** **(c)**

Figure A11. (a) SEM images of carbon spheres (CS) prepared without Fe and FeO/CS composite prepared at an Fe:C molar ratio of 1:1 and through a hydrothermal process at 180 ºC; **(b)** Equilibrium adsorption of PFOA by FeO/CS(1:1) at 2 h, and degradation of pre-concentrated PFOA after 4 h of solar light exposure, and **(c)** Defluorination kinetics of PFOA by FeO/CS prepared at various Fe:CS molar ratios (indicated in the brackets). Experimental conditions: initial [PFOA] = 200 μg L^{-1}, FeO/CS = 1.0 g L^{-1}, pH = 7.0 ± 0.3. Photodegradation conducted under simulated solar light (100 mW cm^{-2}).

Desorption of PFOS from Willow Grove Soil using oil dispersants. PFOS was the major contaminant in the Willow Grove field soil (PFOS = 1507.7 ± 37.6 ng g^{-1}; PFOA = 21.4 ± 6.8 ng g^{-1}). In search for a 'green', low-cost and efficient eluent for desorbing PFOS from soil, we tested two common EPA-approved dispersants (Corexit EC9500A and SPC1000), which are composed mainly of surfactants. **Figure A12a** compares the batch equilibrium desorption data using deionized water or the dispersants at various concentrations with or without NaCl for desorption of PFOS from the soil. Evidently, Corexit EC9500A at 50 mg L^{-1} was able to effectively remove

PFOS, while SPC1000 actually retarded the desorption due to the different compositions. It is also noteworthy that the addition of NaCl (1 wt.%) also retarded the desorption process, which is attributed to the suppression of the soil surface negative potential.

The desorption was not exhaustive because desorbed PFOS in solution prevents further desorption. When the tests were carried out in the successive desorption mode (i.e., replacing the solution with fresh dispersant solution after each batch), >90% of PFOS was desorbed at a dispersant concentration of 300 mg L^{-1} (**Figure A12b**). When the PFAS-laden dispersant solution was treated with 5 g L^{-1} of Ga/TNTs@AC, ~98% of PFOS was rapidly re-adsorbed on the photocatalyst (**Figure A12c**), setting up for subsequent photodegradation. Moreover, the treated dispersant solution was then reused for desorption.

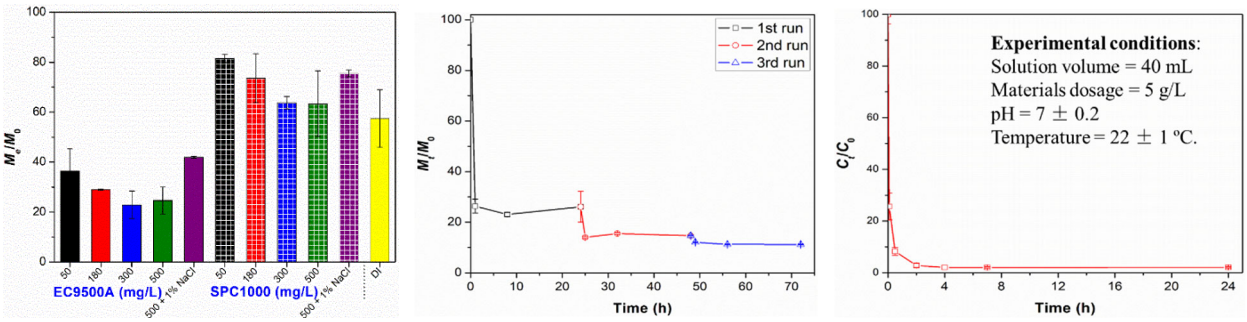

(a) **(b)** **(c)**

Figure A12. (a) Batch equilibrium desorption of PFOS from Willow Grove Soil using two dispersants at various concentrations; **(b)** Successive desorption of PFOS from Willow Grove soil using Corexit 9500A (300 mg L^{-1}); **(c)** Adsorption of PFOS from spent dispersant solution from (b) by Ga/TNTs@AC. M_0: initial PFOS mass in soil, M_t: PFOS mass in soil at time t, M_e: PFOS mass in soil at equilibrium.

Cost analysis. A preliminary cost analysis for a hypothetical 0.1 MGD treatment system indicates that the overall cost for the "Concentrate-&-Destroy" process is $2.23 for complete degradation of PFOA in 1,000 gal of water, which is 9.1 and 6.5 times lower than those by AC adsorption followed by incineration and landfill, respectively.

Implications for Future Research and Benefits

In this SEED project, we proposed and extensively tested a novel innovative "Concentrate-&-Destroy" strategy for cost-effective and complete destruction of PFAS in IDWs. The key findings are summarized as follows:

- Three reusable adsorptive photocatalysts were prepared based on low-cost and well-accepted commercial materials (AC and TiO_2);
- As an adsorbent, the materials can effectively adsorb/concentrate PFAS from water through commonly used reactor configurations (fixed-bed column or batch reactor); as a photocatalyst, the materials can rapidly and completely degrade PFOA and PFOS under UV or solar light;
- The carbon and metal modifications of TNTs or iron oxide not only facilitate selective adsorption of PFAS, but greatly enhance the photocatalytic degradation;
- The *in situ* efficient photodegradation of PFAS also regenerates the materials, allowing for repeated uses of the photocatalysts without incurring costly chemical regeneration and without generation of waste residuals; and

- Dilute Corexit EC9500A can serve as an effective, environmentally safe and low-cost extractant for removing PFOS and PFOA from field soil, and the "Concentrate-&-Destroy" technique can be applied to treat the spent dispersant solution so as to reuse the solution and destroy the PFAS.

The "Concentrate-&-Destroy" strategy offers some unprecedented advantages over conventional approaches, such as adsorption, landfill and incineration, to treat persistent organic pollutants, including:

- It treats low concentrations of PFAS in large volumes of water using low-cost and easy-to-operate adsorption process, and then completely destroys the concentrated PFAS *in situ* through highly efficient photocatalytic approach, representing significant cost savings;
- It eliminates the need for costly and toxic chemical/solvents for regeneration, and generates little or no process waste residual;
- The system can be easily applied on site and is easier to operate, and can be made mobile and "deployed easily, minimizing the spatial footprint and mobilization time and effort";
- It holds the potential to achieve "unrestricted disposal, discharge, and/or reuse of IDW on-site" upon some follow-on studies, and will greatly aid DoD Remedial Project Managers in more effective management of the PFAS-contaminated sites.

This intensive SEED effort directly addressed the SERDP's critical need to develop "more cost-effective and efficient technologies for treatment of IDW from PFAS investigations". The findings provide compelling evidence for a brand new strategy for "green", cost-effective and efficient destruction of PFAS. The "Concentrate-&-Destroy" strategy meets the DoD's preference "for destructive technologies" "so as to avoid potential future environmental liability" associated with PFAS.

Based on the findings, we anticipate that the new technology will potentially equip the DoD Remedial Project Managers with a powerful on-site treatment approach in treating PFAS at hundreds of the DoD sites. To this end, the following follow-on research activities are warranted:

- ✓ The adsorptive photocatalysts can be further optimized in terms of selectivity for PFAS and photoactivity by tuning the parent materials, the dopants, and synthesis conditions towards more efficient mineralization of PFAS, especially for PFAS in soil extracts;
- ✓ Composite materials that are more reactive under solar light should be further explored;
- ✓ Further investigations are needed to test the effectiveness under DoD field water/soil conditions to identify potential inhibitions of the water matrix and find out ways to overcome these inhibitive effects and to optimize the water chemistry conditions;
- ✓ Pilot-scale experiments should be carried out to facilitate more realistic assessment of the technical and economic effectiveness and to guide field application design;
- ✓ Desorption of PFAS from soil can be further optimized by adjusting the solution recipe and chemistry to facilitate more efficient desorption of PFAS and to promote subsequent photodegradation;
- ✓ Water chemistry conditions can be optimized to promote photocatalytic degradation of more persistent PFAS or PFAS from the dispersant solutions, including addition of proper photosensitizers and elevation of reaction temperature; and
- ✓ To promote earliest possible field adoption, various technology transition/transfer measures should be taken immediately following the pilot-testing, first towards the DoD end users, and then the market at large (e.g., landfill leachate and groundwater sites).

1. Objectives

The overall goal of this SEED project was to develop an innovative, cost-effective and 'green' technology, referred to as "Concentrate-&-Destroy" for destruction of PFAS from DoD's IDWs including both PFAS-contaminated water and soil. The specific objectives were to:

1) Develop a new class of novel composite materials based on commercially available, low-cost AC, TiO_2, and CS-modified iron oxide (FeO/CS), which can offer both rapid and high-capacity adsorption and high photocatalytic degradation of PFAS;
2) Test the effectiveness of the new materials for adsorption and photocatalytic degradation of PFAS (PFOA and PFOS) in water under UV or solar light;
3) Examine reusability of the materials for repeated adsorption and photodegradation of PFAS without chemical regeneration;
4) Explore a 'green' and cost-effective approach for eluting PFAS from IDW soil using dilute surfactants or oil dispersants;
5) Test the effectiveness of the new materials for adsorption and photodegradation of PFAS in the spent desorbing solution, and reusability of the treated solution; and
6) Carry out a preliminary cost-benefit analysis.

This SEED project directly addresses SERDP's Statement of Need (SON) "to develop innovative approaches for treatment of investigation-derived waste (IDW) from investigations of per- and polyfluoroalkyl substance (PFAS) contamination in the subsurface." The technology builds upon a new class of cutting edge adsorptive photocatalysts that can offer both high adsorption capacity for PFAS and photocatalytic activity to efficiently degrade and mineralize/defluorinate PFAS under UV or solar light. (Herein: *degrade* refers to breakdown or conversion of PFAS into other compounds, whereas *mineralize/ defluorinate* indicates conversion of fluorine in PFAS into fluoride ions).

This innovative technology emphasizes the SERDP's critical need "for destructive technologies that treat the IDW rather than rely on landfilling so as to avoid potential future environmental liability", and was aimed to reduce or eliminate the environmental risk associated with PFAS in IDW water and soil in a "green" and cost-effective manner. Ultimately, this new technology shoots for the following requirements:

- It will "permit unrestricted disposal, discharge, and/or reuse of IDW on-site";
- It can be made "mobile" "that can be deployed easily, minimizing the spatial footprint and mobilization time and effort"; and
- It is "cost effective" "compared to current disposal methods" such as adsorption, ion exchange, landfill and incineration.

This study also attempted to acquire compelling experimental data "to develop a complete proposal for a more extensive follow-on project".

2. Background

2.1. Environmental issues with PFAS

Per- and polyfluoroalkyl substances (PFAS) have become a class of important contaminants in soil and water due to their wide-spread applications, resistance to environmental degradation, and potential health effects [Li et al., 2020]. Perfluorooctanoic acid (PFOA) and perfluorooctane sulfonate (PFOS) are the most detected PFAS [Li et al., 2020]. To mitigate human exposure, EPA established a lifetime health advisory level of 70 ng L^{-1} for combined PFOA and PFOS in drinking water on May 19, 2016. A recent survey reported that drinking water supplies for 6 million U.S. residents exceeded the advisory level [Hu et al., 2016].

Human exposure to PFAS has been linked to cancer, elevated cholesterol, obesity, immune suppression, and endocrine disruption [Hu et al., 2016]. Health concerns in the early 2000s prompted manufacturers in Europe and North America to phase out production of some long-chain PFAS [Land et al., 2018].

The EPA's third Unregulated Contaminant Monitoring Rule (UCMR 3) requires close monitoring of PFAS. In addition to the EPA health advisory, EPA unveiled a PFAS Action Plan that will move forward with the Maximum Contaminant Level (MCL) process for PFOA and PFOS. As part of the Action Plan, U.S. EPA will continue their enforcement actions and clarify clean up strategies, and expand monitoring of PFAS in the environment. Meanwhile, many states have initiated stringent drinking water standards on PFAS.

Aqueous film-forming foams (AFFFs) have been a vital tool to fight large hydrocarbon fires [Place and Field, 2012]. Due to their surface-tension lowering properties, fluorinated surfactants are often added in the formulations to enhance their firefighting capabilities [Schaefer et al., 2008]. Historical reports of uncontrolled spills and repeated uses of AFFFs during fire training and for AFFF performance testing have been correlated with elevated concentrations of PFAS in biota, surface water, or groundwater [Place and Field 2012].

AFFF formulations have been used by DoD since the 1970s, and the military use accounted for 75% of the U.S. market [Moody and Field, 2000]. Consequently, hundreds of the military sites have been contaminated with PFAS [SERDP, 2016]. Groundwater at sites impacted by AFFF uses has the greatest recorded concentrations of PFAS of any aqueous environment [Backe et al., 2013]. The vast majority of the AFFF formulations used by DoD contain PFOS and related perfluoroalkyl sulfonates such as perfluorohexane sulfonate (PFHxS) [SERDP, 2016]. Although the product was phased out in 2002, DoD continued (until only recently) to use PFOS-containing AFFF stocks [SERDP, 2016]. As a result, the use of PFOS-based AFFFs has been a major environmental liability of DoD.

In the last decade or so, DoD has been increasingly investigating the extent of PFAS contamination across its portfolio of sites. Consequently, large quantities of investigation-derived wastes (IDWs) were (and will continue to be) generated [SERDP, 2017]. Yet, cost-effective technologies are lacking to treat the IDWs including both PFAS-laden water and soil [SERDP, 2017]. To a large extent, current practices rely on landfilling and incineration of these wastes, which are both costly and pose additional transportation requirements and secondary contamination issues. As such, SERDP has been looking for "alternative innovative technologies that would permit unrestricted disposal, discharge, and/or reuse of IDW on-site" [SERDP, 2017].

2.2. The state of the technology

Due to the strongly polarized carbon–fluorine bonds and the amphiphilic nature, PFAS are uniquely persistent (biological half-life = ~3 years), mobile, bio-accumulative in the environment [Li et al., 2020]. Conventional treatment technologies are not effective for degrading PFAS, such as standard biological, Fenton and photochemical processes [Li et al., 2020]. Numerous studies have examined remediation methods for treatment of PFAS (mainly PFOA and PFOS) [Espana et al., 2015; Li at al., 2020]. Yet, cost-effective technologies remain lacking. Yet, a cost-effective solution remains lacking. Sorption has been one of the most cited methods to remove PFASs [Du et al., 2014], and various adsorbents have been investigated, including AC [Deng et al., 2015; Yu et al. 2009], carbon nanotubes [Deng et al., 2012], ion exchange resins [Deng et al., 2010; Yu et al. 2009], synthetic magnetite nanoparticles [Gong et al., 2016] and biomaterials [Deng et al., 2013; Zhang et al. 2011]. However, these adsorbents bear with some critical drawbacks, such as low adsorption capacity, high material cost, costly regeneration, and/or generation of large volumes of process waste. For instances, AC has been tested/used at several sites to remove PFOS and PFOA from contaminated water; however, the cost-effectiveness of AC systems remains questionable due to costly regeneration [Du et al., 2014, SERDP 2016]. While ion exchange resins may effectively adsorb PFASs, large volumes of regenerant brines are produced, increasing the operating cost and demanding additional waste treatment and handling. Moreover, while adsorption concentrates PFASs, it does do not degrade them. Consequently, "Solutions are needed which include provisions for regeneration of spent media, and treatment and disposal of ancillary waste streams." [SERDP, 2016].

Past efforts to induce photochemical transformations of PFASs employed persulfate ions ($S_2O_8^{2-}$) or TiO_2 particles as sensitizers, but the reactions are very slow [Dillert et al., 2007; Hori et al. 2005; Panchangam et al., 2009]. For instance, degradation of PFOA using $S_2O_8^{2-}$ as a sensitizer was found slow and costly due to the large amount of $S_2O_8^{2-}$ required and because persulfate activation is energy demanding [Hori et al., 2005]. Sonochemical oxidation was also studied, but it is energy-demanding and its feasibility has not been tested under realistic field conditions [Espana et al., 2015].

Treating PFASs-bearing IDW soil is even more challenging because the soil-sorbed PFAS are not directly accessible. Typically, PFASs are subject to adsorption to soil (mainly soil organic matter or SOM). Based on laboratory experiments, the average log Koc values are 3.0 for PFOS and 2.8 for PFOA. Therefore, the main environmental concern has been the slow leaching of adsorbed PFASs into groundwater [Yao et al., 2015], and chemical or biochemical degradation of soil-sorbed PFASs is subject to desorption or mass transfer limitation. For instance, a field study showed that under natural groundwater extraction, only 0.1% of the soil sorbed PFASs was removed from the soil in two years [Paterson et al., 2008]. For typical IDW soil, the conventional disposal methods have been landfill (upon proper treatment and permission), containment, or incineration [Yao et al., 2015]. With the mounting environmental regulations, however, landfill/containment of IDW is facing growing challenges, whereas incineration is cost-inhibitive. In fact, many common soil remediation techniques have been proven ineffective for treating PFAS contaminated soil, including air sparging, soil-vapor extraction, bioremediation, and hydrolysis [Pancras et al., 2013].

To speed up the soil remediation process, in situ soil flushing or soil washing using a flushing agent has been often practiced. For instance, Mulligan et al. [2001] reported that the use of flushing

solution containing 1% of an anionic surfactant (SDBS) shortened the remediation time for a trichloroethylene (TCE) contaminated site by 100 times compared to the conventional pump-and-treat. However, because desorption of PFAS is often more difficult, more aggressive solvents (e.g., methanol) were used to elute PFAS from soil or other adsorbents, which is not only costly, but environmentally prohibitive. In a prior work, the PI [Pan et al., 2009] observed that the addition of 43.4 mg L^{-1} of SDBS increased the water solubility of PFOS by >2 times and lowered the soil adsorption by 31%. Based on another prior work by the PI's group [Duan et al., 2018], dilute oil dispersants (18 mg L^{-1}), known as Corexit 9500A and SPC1000, were able to effectively desorb sediment-sorbed oil alkanes and polycyclic aromatic hydrocarbons (PAHs). These findings suggest that low-cost and nontoxic surfactants or oil dispersants may effectively desorb PFAS from soil in a more cost-effective and environmentally benign manner.

2.3. The proposed technology

This project aimed to develop an innovative "Concentrate-&-Destroy" technique that can highly effectively adsorb/concentrate and degrade PFAS in water. The key to this technology is to develop a new class of carbon-modified photocatalysts (Fe/TNTs@AC, Ga/TNTs@AC, and FeO/CS) that can serve as both an adsorbent and a photocatalyst. As an adsorbent, the composite materials offer not only rapid adsorption rate, but also high adsorption selectivity towards PFAS, thanks to the concurrent hydrophobic interactions (between the carbons and PFAS tails) and Lewis acid-base interactions (between metals and PFAS head groups) as well as the unique structures of the composite materials. As a photocatalyst, the materials provide superior photocatalytic activity over conventional photocatalysts (e.g., TiO_2) owing to the carbon-mediated electron transfer and enhanced generation of reactive species. **Figure 1** illustrates the core-shell structure of activated carbon (AC) supported/modified titanate nanotubes (TNTs@AC) and shows a high resolution transmission electron microscopy (TEM) image of the tubular structure of TNTs on AC [Liu et al., 2016].

The effective adsorption concentrates trace levels of PFAS from large volumes of contaminated water onto a small amount of the photocatalyst, facilitating subsequent photochemical destruction of PFAS in a more efficient and cost-effective manner; and the photodegradation not only destroys PFAS, but also regenerates the material, allowing for multiple cycles of operations without invoking costly chemical/solvent regeneration or producing any process waste residuals. **Figure 2** illustrates the process schematic of the "Concentrate-&-Destroy" strategy for treating PFAS in IDW water. First, PFAS in water are concentrated on metal-doped TNTs@AC (M/TNTs@AC) via common fixed-bed adsorption; Second, the PFAS-loaded adsorptive photocatalyst is subjected to UV or solar light to destroy the pre-sorbed PFAS, which also regenerates the material; and Third, the photo-regenerated material is reused in another cycle of adsorption/photodegradation. Alternatively, the adsorption step may be conducted using the conventional mixer-settler configuration (for PAC).

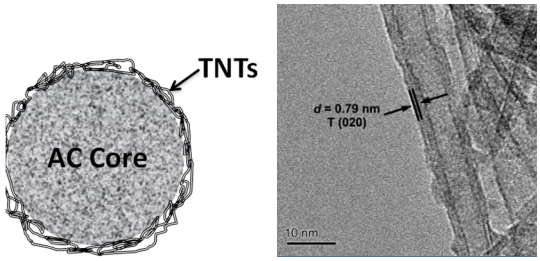

Figure 1. Left: Core-shell structure of activated charcoal supported titanate nanotubes (TNTs@AC); Right: HRTEM images of TNT nanotubes on AC.

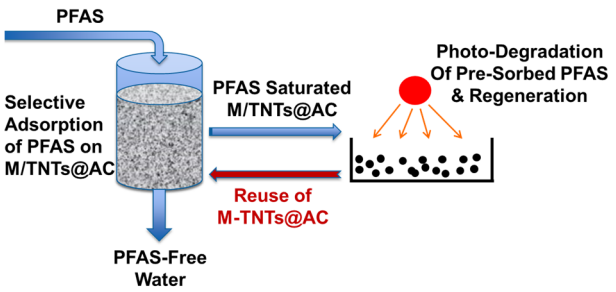

Figure 2. Schematic of the "Concentrate-&-Destroy" concept for removal and destruction of PFAS in water.

To treat PFAS in soil, we proposed and tested a novel three-step approach (desorption, concentrate and destroy). As shown in **Figure 3**, soil-sorbed PFAS are first desorbed using a dilute solution of a low-cost and nontoxic oil dispersant, known as Corexit 9500A, and the "Concentrate-&-Destroy" technique is applied to treat the PFAS in the dispersant solution. The treated dispersant solution is then reused in another desorption cycle, and the concentrated PFAS are then destroyed via the photodegradation.

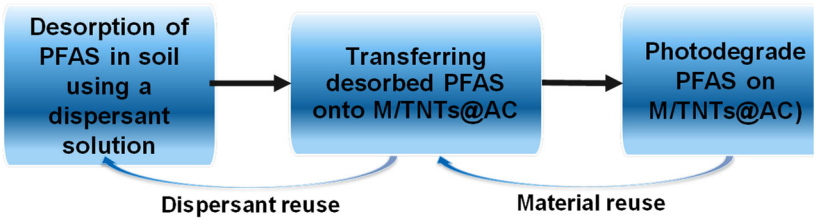

Figure 3. Schematic for treating PFAS in IDW soil.

3. Materials and Methods

3.1. General Technical Approach

The research objectives were accomplished by carrying out five interconnected tasks as shown in **Figure 4**. In the screening experiments, PFOA and PFOS were used as the model target PFAS, and deionized water or synthetic water was used in the water treatment tests. In addition, the material performance was preliminarily probed using groundwater from the DoD's Willow Grove site. For soil treatment (PFAS desorption), the field soil from Willow Grove was used.

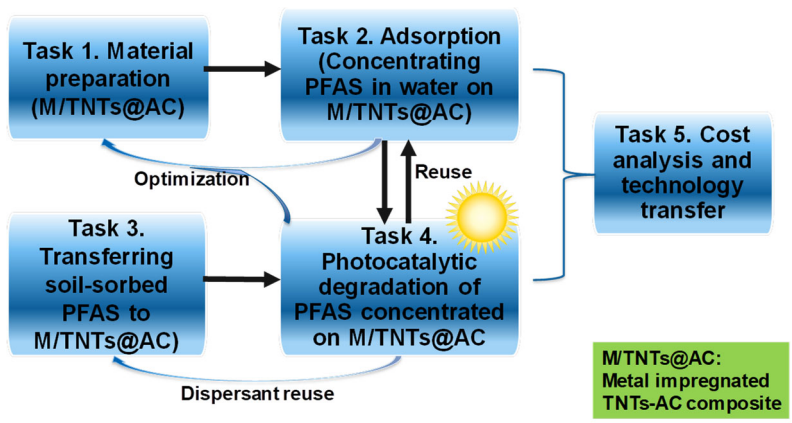

Figure 4. Flow chart of the research approach and tasks.

First, we prepared two metal-doped TNTs@AC composites (Fe/TNTs@AC and Ga/TNTs@AC) through a facile hydrothermal treatment approach based on our prior work (Liu et al., 2016; Zhao and Liu, 2018) and by thermal impregnation of iron or gallium onto TNTs@AC. In addition, we prepared a new iron-oxide/CS composite, referred to as FeO/CS, through a one-step hydrothermal treatment of Fe(III) and glucose precursors. While Fe/TNTs@AC and Ga/TNTs@AC were photoactive under UV light, FeO/CS was able to degrade PFAS under solar light. The new adsorptive photocatalysts were then characterized with respects to their morphology, particle size, surface area, elemental composition, crystal type and structure, pore size distribution, surface functional groups, element oxidation states, light absorbance, band energy gap, and zeta potential. The characterization information, along with the subsequent adsorption and photodegradation data, is then used to polish the material synthesis and understand how material characteristics relate to the adsorption capacity and photocatalytic activity for PFAS.

Second, we tested effectiveness of the new materials for adsorption of characterization of the new AC/CS-supported/modified photocatalysts through batch adsorption kinetic and equilibrium experiments.

Third, for treating PFAS in soil, batch desorption tests were carried out to elute soil-sorbed PFAS using various desorbing agents (we focused on two commonly used oil dispersants Corexit 9500A and SPC1000). Based on the screening results, Corexit 9500A was selected as the best dispersant, and PFAS in the dispersant solution was then reloaded onto the photocatalyst (Ga/TNTs@AC) and destroyed subsequently.

Forth, Photodegradation of PFAS pre-concentrated on the photocatalysts was tested in batch reactors under UV or solar light (with 95% of water removed from the batch adsorption tests), and

factors affecting the effectiveness was examined. The photo-regenerated materials were then reused in another cycle of adsorption-photodegradation to gauge the reusability of the materials.

Lastly, a preliminary cost-benefit analysis was carried out based on the batch experimental data.

3.2. Materials and Methods: Fe/TNTs@AC

3.2.1. Chemicals and materials

All chemicals were of analytical or higher grade. Nano-TiO_2 (P25, 80% anatase and 20% rutile) was purchased from Evonik (Worms, Germany). PFOA and PFOS were obtained from Sigma-Aldrich (St. Louis, MO, USA). Sodium hydroxide (pellets) and absolute ethanol were obtained from Acros Organics (Fair Lawn, NJ, USA). Filtrosorb-400® granular activated carbon (F-400 GAC) was obtained through the courtesy of Calgon Carbon Corporation (Pittsburgh, PA, USA) and was used as received. F-400 GAC was made of bituminous coal to achieve high density and high surface area for organic pollutant removal. Perfluoro-n-[1,2,3,4,5,6,7,8-$^{13}C_8$]octanoic acid (^{13}C-PFOA or M8PFOA) and sodium perfluoro-1-[1,2,3,4,5,6,7,8-$^{13}C_8$]octanesulfonate (^{13}C-PFOS or M8PFOS) were purchased from Wellington Laboratories Inc. (Guelph, Ontario, Canada Perfluoro) and were used as isotopically labeled internal standards.

3.2.2. Synthesis of Fe/TNTs@AC

Fe/TNTs@AC composite was initially synthesized through an alkaline hydrothermal treatment method modified based on our previous work (U.S. Patent 62/452,648).

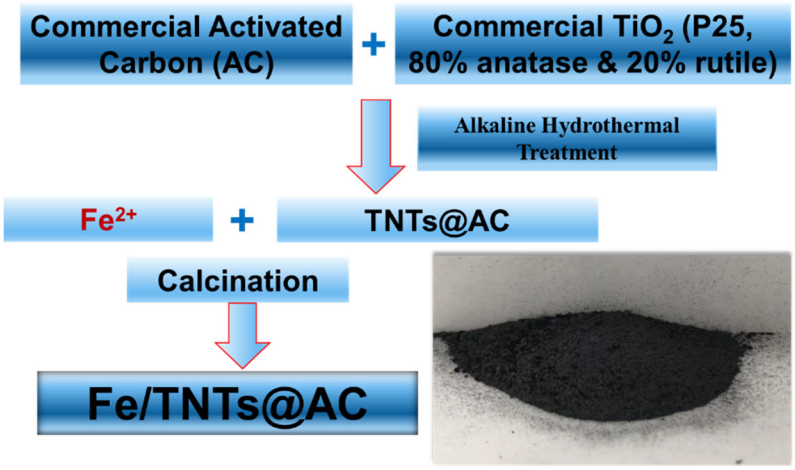

Figure 5. Synthesis of a novel adsorptive photocatalysts, Fe/TNTs@AC based on commercial activated carbon and TiO_2 with Fe impregnation.

Typically, 1.2 g of TiO_2 was mixed with 1.2 g of F-400 GAC and then dispersed into 67 mL of a 10 M NaOH solution. After stirring for 12 h, the mixture was transferred into a Teflon reactor and heated at 130 °C for 72 h. Then, the gray precipitates, *i.e.*, TNTs@AC, were washed with deionized (DI) water until neutral pH, and then oven-dried at 105 °C for 4 h. Then, 1 g of dried TNTs@AC was dispersed in 100 mL of DI water, and then 10 mL of an $FeCl_2$ solution (1 g L^{-1} as Fe, pH = 3.0) was drop-wise added into the TNTs@AC suspension (Fe:TNTs@AC = 1 wt.%).

Upon equilibrium, nearly all (>99.7%) Fe(II) ions were adsorbed by TNTs@AC, the solid particles were separated via centrifugation, and then oven-dried at 105 °C for 24 h, which also oxidized Fe(II) to Fe(III). The supernatant was analyzed for residual dissolved iron. Then, the dried particles were calcined at 550 °C and under a nitrogen flow at 100 mL min^{-1} for 3 h. No detectable Ti or Fe leaching was observed when 0.2 g of Fe/TNTs@AC was mixed with 200 mL DI water.

Additionally, the calcination temperature and Fe content were varied to obtain best photoactive Fe/TNTs@AC (good adsorption rate and capacity and high photoactivity). The calcination temperatures were 300 °C, 550 °C, 650 °C, and 850 °C, and the Fe contents included 0.5 wt.%, 1 wt.%, 3 wt.%, and 5 wt.%. Based on the subsequent adsorption and photodegradation tests, Fe/TNTs@AC prepared at 550 °C calcination temperature and 1 wt.% of Fe was chosen as the best composite for further studies. For comparison, TNTs@AC without Fe was also prepared following the same procedure.

3.2.3. Characterization of Fe/TNTs@AC

Fe/TNTs@AC was characterized with respects to various physicochemical and photochemical properties. The surface morphology was imaged using a scanning electron microscope (SEM) (20 kV; FEI XL30F, Philips, USA), equipped with an energy-dispersive X-ray spectroscopy (EDS). Additionally, transmission electron microscopy (TEM) analysis was conducted on a Tecnai30 FEG microscopy (FEI, USA) operated at 300 kV. The zeta potential (ζ) was measured using a Malvern Zetasizer Nano-ZS90 (Malvern Instrument, Worcestershire, UK). The crystalline structures were analyzed on a Bruker D2 PHASER X-ray diffractometer (XRD, Bruker AXS, Germany) using Cu Kα radiation (λ = 1.5418 Å) and at a scanning rate (2θ) of 2° min^{-1}. The surface chemical compositions and oxidation states were analyzed using an AXIS-Ultra X-ray photoelectron spectroscopy (XPS) (Kratos, England), which was operated at 15 kV and 15 mA (Al *K*α X-ray). The standard C 1s peak (Binding energy, E_b = 284.80 eV) was used to calibrate all the peaks and eliminate the static charge effects. The Brunauer–Emmett–Teller (BET) surface area was obtained using an ASAP 2010 BET surface area analyzer (Micromeritics, USA) in the relative pressure (P/P0) range of 0.06–0.20. The pore size distribution was determined following the Barret-Joyner-Halender (BJH) method. The nitrogen adsorption at the relative pressure of 0.99 was used to determine the pore volumes and the average pore diameters.

3.2.4. Adsorption kinetic and isotherm tests

Adsorption kinetic tests were performed in batch reactors using 40 mL high-density polypropylene (HDPE) vials under the following experimental conditions: initial PFOA or PFOS = 100 μg L^{-1}, material dosage = 1 g L^{-1} for PFOA and 2 g L^{-1} for PFOS, pH = 7.0, and temperature = 22 ± 1 ºC. The adsorption was initiated by mixing a specific material with a PFOA or PFOS solution. The vials were kept in the dark and under shaking at 100 rpm. At predetermined time intervals, the vials were sampled in duplicate and centrifuged for 2 min at 4000 rpm, and the supernatants were analyzed for remaining PFOA/PFOS. Each kinetic test lasted for 1 h, which was sufficient to reach equilibrium.

Adsorption isotherms for PFOA were conducted following the same procedure under the following conditions: initial PFOA = 0 μg L^{-1} to 100 mg L^{-1}, material dosage = 1 g L^{-1}, pH = 7.0, solution volume = 40 mL, and equilibrium time = 24 h.

3.2.5. Photodegradation kinetic tests

Following the adsorption equilibrium, the mixtures were left still for 1 h to allow the composite materials to settle by gravity (>99% of the materials settled). Then, ~95% of the supernatant was pipetted out, and the residual solid-liquid mixture was transferred into a quartz photo-reactor with a quartz cover. Then, 8 mL of DI water was added to the mixture so that the solution volume in the photo-reactor reached 10 mL (i.e., soli:solution = 1:10), and the solution pH was adjusted to 7.0. The reactor was then placed in a Rayonet chamber UV-reactor (Southern New England Ultraviolet CO., Branford, CT, USA), and subjected to UV light at a wavelength of 254 nm and an intensity of 21 mW cm^{-2} at a 15 in distance. After predetermined times (*i.e.*, 1, 2, 3 and 4 h), the liquid was collected for fluoride analysis while the solid was extracted for remaining PFOA using 40 mL of methanol at 80 °C for 4 h. M8PFOA/M8PFOS was used as internal standards (IS) to correct the mass recovery. Without the IS, the average method recovery was >90% for both PFOA and PFOS. All tests were carried out at least in duplicate.

In this report, degradation of PFAS refers to decomposition or breakdown of PFAS into other compounds, e.g., shorter-chain perfluorinated carboxylic acids (PFCAs) or perfluorosulfonic acids (PFSAs), CO_2, and F^-; whereas defluorination or mineralization indicates conversion of fluorine in PFAS into fluoride ions. The degradation was quantified by comparing the initial PFAS loaded on a photocatalyst and PFAS remaining upon light irradiation, whereas defluorination was determined by measuring the fluoride produced upon the photocatalytic reactions.

3.2.6. Effect of environmental factors on photodegradation of PFOA by Fe/TNTs@AC and preliminary test of removal PFOS from field groundwater by Fe/TNTs@AC

Batch kinetic and/or equilibrium tests were carried out to examine effects of NaCl, $CaCl_2$, and dissolved organic matter (DOM) on adsorption and photodegradation of the PFAS by Fe/TNTs@AC.

The adsorption tests were initiated by adding 0.08 g of Fe/TNTs@AC into 40 mL of a 100 µg L^{-1} PFOA solution (material dosage = 2 g L^{-1}) and in the presence of additional NaCl (≤1 mM), $CaCl_2$ (≤1 mM) or DOM (≤5 mg L^{-1} as TOC), a commercial standard Leonardite humic acid was used as a surrogate DOM.

Following the adsorption equilibrium, photodegradation of the pre-loaded PFOA was carried out following the similar approach as in **Section 3.2.5**, but in the presence of additional NaCl (≤1 mM), $CaCl_2$ (≤1 mM) or DOM (≤5 mg L^{-1} as TOC). Prior to the UV irradiation, 8 mL of a NaCl, $CaCl_2$, or humic acid solution was added to the photo-reactor so that the solution volume in the photo-reactor reached 10 mL (solid:solution ratio = 2 g), with the solution pH adjusted to 7.0. After 2 h of UV irradiation, aqueous samples were taken and analyzed for fluoride concentration.

To preliminarily test effect of temperature, the cooling fan of the photo-reactor was turned off, and the photodegradation tests were then carried out at a chamber temperature of 62-65 °C.

To preliminarily gauge the effectiveness of the as-prepared Fe/TNTs@AC for treating DoD field groundwater, the adsorption and photodegradation tests were performed using the groundwater taken from the Willow Grove site. Based on our analysis, the basic groundwater quality parameters were: PFOS = 96.1 µg L^{-1} (linear PFOS = 57.3 µg L^{-1} and branched PFOS = 38.8 µg L^{-1}), pH = 6.1, PFOA = 1.9 µg L^{-1}, F^- = 218 µg L^{-1}, Cl^- = 16.3 mg L^{-1}, SO_4^{2-} = 8.6 mg L^{-1},

NO_3^- = 27.6 mg L^{-1}, and $H_2PO_4^-$ = 6.2 mg L^{-1}. Note: PFOA and PFOS were analyzed using LC-MS/MS by UMBC.

In brief, 2 g L^{-1} of Fe/TNTs@AC was spiked in 40 mL of the field groundwater. After 24 h of adsorption, aqueous samples were collected and analyzed for PFOA/PFOS remaining, and the PFAS-laden Fe/TNTs@AC was then transferred to the photo-reactor for photodegradation following the same method as described in **Section 3.2.5**.

3.2.7. Density functional theory calculations

To acquire more theoretical insight into the surface complexation of PFOA anions with Fe/TNTs@AC, density functional theory (DFT) calculations were performed using Gaussian 09. According to Wei et al. [2017], the B3LYP functional, 6−311+G(d,p) basis set, and Integral Equation Formalism Polarized Continuum Model (IEFPCM) were employed in the hybrid DFT calculations. To determine the orientation of PFOA binding on the Fe/TNTs@AC surface (e.g., parallel or perpendicular), formic acid and an edge-sharing two-Fe(III) octahedral dimer were used to mimic the surface reactions. This simplified configuration saved a massive amount of computing time and, at the same time, adequately predicted the possible orientation of PFOA anions on the surface [Wei et al., 2017].

3.3. Materials and Methods: Ga/TNTs@AC

3.3.1. Chemicals and materials

PFOS was purchased from Matrix Scientific (Columbia, SC, USA). A 10 mg L^{-1} of PFOS stock solution of was prepared and stored at 4 ºC. Gallium (III) chloride anhydrous ($GaCl_3$) was purchased from VWR International (Radnor, PA, USA). Other chemicals and materials were the same as in **Section 3.2.1.**

3.3.2. Synthesis of Ga/TNTs@AC

Ga/TNTs@AC was prepared following similar procedure as for Fe/TNTs@AC. **Figure 6** depicts the synthesis of TNTs@AC and the subsequent Ga impregnation and calcination.

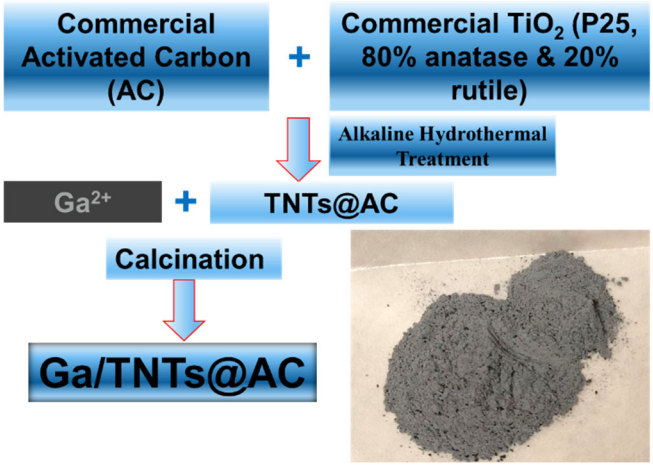

Figure 6. Synthesis of Ga/TNTs@AC via an alkaline hydrothermal approach.

In brief, 1g of the dried TNTs@AC was dispersed in 100 mL of DI water, and then 4 mL of a $GaCl_3$ solution (5 g L^{-1} as Ga, pH = 3.5) was dropwise added into TNTs@AC suspension. Adjust the pH to 7.0 and allow for 3 h adsorption, which was enough to reach equilibrium. The solid particles were separated via centrifugation, and then dried in an oven at 105 °C for 24 h. The resulting particulates were further calcined at 550 °C for 3 h under a nitrogen flow of 100 mL min^{-1}. The resulting Ga/TNTs@AC contained 2 wt.% of Ga. For comparison, Ga/TNTs@AC was prepared at different Ga contents (1, 2, 3, and 5 wt.%). Based on the subsequent adsorption/photodegradation results, Ga/TNTs@AC with 2 wt.% of Ga showed best adsorption rate and photodegradation activity for PFOS, and thus, was further studied.

3.3.3. Adsorption and subsequent photodegradation of PFOS by Ga/TNTs@AC

Adsorption and photodegradation of PFOS by Ga/TNTs@AC were tested following the same procedure as for Fe/TNTs@AC described in **Sections 3.2.4** and **3.2.5**. Detailed experimental conditions are provided in the respective figure captions.

3.4. Materials and Methods: FeO@CS

3.4.1. Chemicals and materials

Iron (III) sulfate hydrate ($Fe_2(SO_4)_3 \cdot xH_2O$), sodium hydroxide (NaOH), nitric acid (HNO_3), D-glucose ($C_6H_{12}O_6$), isopropyl alcohol ($(CH_3)_2CHOH$, ISA), potassium dihydrogen phosphate (KH_2PO_4), PFOA ($C_8HF_{15}O_2$), and 5,5-Dimethyl-1-Pyrroline N-oxide (DMPO) were purchased from Alfa Aesar, Ward Hill, MA, USA. All the chemicals were of analytical grade or higher, and were used without further purification.

3.4.2. Synthesis and characterization of FeO/CS

The iron oxide/carbon sphere (FeO/CS) composite was synthesized via a modified one-step hydrothermal method [Jia et al., 2011; Wang et al., 2014]. **Figure 7** illustrates the preparation procedure with D-glucose and iron sulfate as the precursors for CS and Fe, respectively.

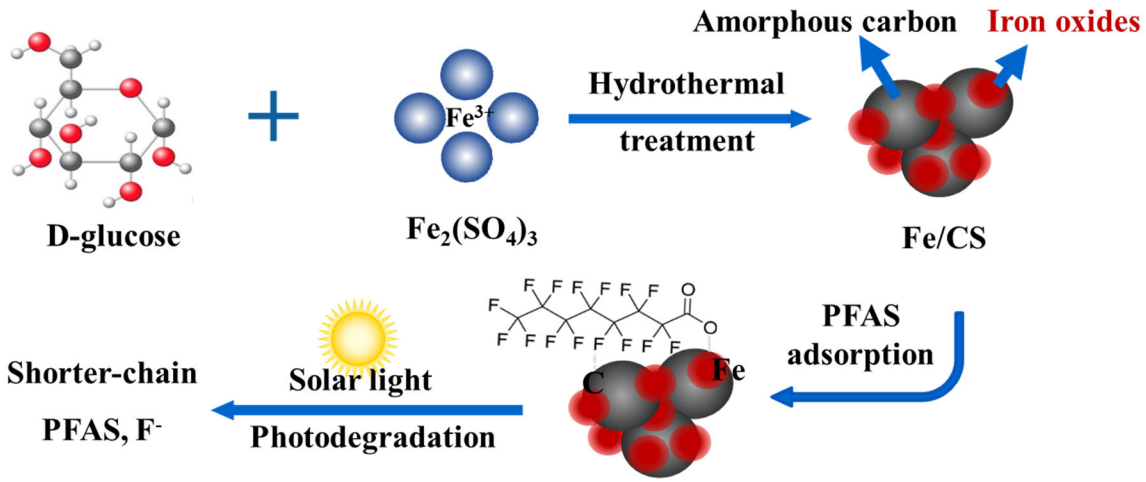

Figure 7. Synthesis of FeO/CS via a modified one-step hydrothermal method and illustration of the potential use for adsorption and photocatalytic degradation of PFAS under solar light.

Typically, 0.04 mol D-glucose was dissolved in 50 mL of ultrapure water. Then a given amount of $Fe_2(SO_4)_3 \cdot xH_2O$ (0.0025, 0.005, 0.01, 0.02 mol) was dissolved in the D-glucose solution, followed by 1 h stirring. Under vigorous stirring, a 28% ammonia solution was added dropwise to raise the solution pH to 7.5 ± 0.1. The mixed solution was then transferred into a Teflon-lined autoclave (100 mL) and treated at 180°C for 18 h. After cooling to room temperature, the resulting black suspension was filtered through a 0.2 μm membrane filter, and the particles washed by DI water 5 times to remove any soluble residuals. Upon gravity settling, the solid material was oven-dried at 80°C. According to the molar ratio of Fe:C of the precursors, the resulting materials are denoted as FeO/CS(m:n), with m:n denoting the Fe:C molar ratio. For comparison, neat CS and iron oxide were also prepared through the same procedure but with only one of the precursors, namely $Fe_2(SO_4)_3 \cdot xH_2O$ or D-glucose.

As illustrated in **Figure 7**, FeO/CS was designed to concentrate and degrade PFAS under solar light, which represents significant energy savings compare to UV irradiation.

3.4.3. Characterization of FeO/CS

FeO/CS was characterized with respects of relevant physical, chemical and photochemical properties. Morphological observations were performed by a scanning electron microscope (SEM, 6700−F, JEOL) and high-resolution transmission electron microscopy (HRTEM, JSM−2010, JEOL) linked with an Oxford Inca250 energy dispersive X-ray spectroscopy (EDS). The surface chemical compositions of the samples were semi-quantitatively evaluated through the EDS scanning. XRD analyses were performed on an X-ray diffractometer (Bruker D8 ADVANCE) with Cu Kα irradiation (40 kV, 40 mA) to characterize the crystalline structures. XRD patterns were obtained from 2θ values of 10° through 80° and at a scan speed of 2° min^{-1}. UV-vis diffuse reflectance spectra (DRS) were acquired using a Shimadzu UV-2550 double-beam digital spectrophotometer equipped with the standard components of a reflectance spectrometer and with $BaSO_4$ as the reference. X-ray photoelectron spectroscopy (XPS) data were obtained by a Thermo Fisher Scientific K-Alpha spectrometer. The C1s peak from the adventitious carbon-based contaminant with a binding energy of 284.8 eV was used as the reference for calibration. Fourier transform infrared spectra (FTIR) were obtained from a Bruker Vertex-70 FTIR spectrophotometer with a resolution of 4 cm^{-1} in transmission mode at room temperature.

3.4.4. Adsorption and photodegradation of PFOA by FeO/CS

Batch adsorption tests of PFOA by FeO/CS were carried out in a 45 mL high-density polyethylene vials by adding 1 g L^{-1} of FeO/CS to 40 mL of a PFOA solution (200 μg L^{-1}, pH 7.0). The vials were mounted on a tumbler operated at 50 rpm. At predetermined times, 1 mL of aliquots per vial were sampled and filtered through a 0.22 μm poly (ether sulfones) (PES) membrane filter, and the filtrates were analyzed for PFOA remaining in the solution.

To facilitate photodegradation experiments, additional PFOA adsorption tests were performed under the following experimental conditions: solution volume = 160 mL, initial PFOA = 200 μg L^{-1}, pH = 7.0, FeO/CS dosage = 1 g L^{-1}. Upon adsorption equilibrium, FeO/CS was separated by gravity, and then, 135 mL of the supernatant solution was removed by pipetting. The remaining 25 mL solid-liquid mixture was transferred to a 250 mL cylindrical quartz tank reactor with a Pyrex pillar (80 × 75 mm). Then, the photodegradation was conducted under simulated solar light using a 94041A solar simulator (Newport Corporation, Irvine, CA). The light intensity reaching

the reactor was 100 mW cm^{-2}. The solid-liquid was mixed with magnetic stirring at 200 rpm during the course of the photodegradation tests. At predetermined times (1, 2, 3, and 4 h), each 5 mL of liquid samples were taken, upon gravity settling, 2 mL of the supernatant was filtered with a 0.22 μm PES membrane filters, and filtrate was analyzed for F^- generated during the photodegradation. The residual solid-liquid mixture was extracted using 20 mL of methanol at 80°C for 8 h and analyzed for PFOA remaining in the solid phase.

3.4.5. DFT calculations

DFT-based calculations were performed to gain further insight into the underlying mechanisms for the adsorption and photocatalytic degradation of PFOA by FeO/CS. The first-principles computations were performed based on the density functional theory (DFT), and were implemented with the Vienna ab initio simulation package (VASP). The projector augmented wave (PAW) based potentials were used to describe nuclei-electron interactions. The generalized gradient approximation (GGA) within the Perdew-Burke-Ernzerh (PBE) of exchange-correlation function was employed. The wave functions at each k-point were expanded with a plane wave basis set, and the kinetic cutoff energy was set to 450 eV. The K-point sets of 7×7×3, 11×3×9 and 1×1×1 were used for Fe_2O_3 (hematite, Ht), FeOOH (ferrihydrite, Ft), and PFOA, respectively. The Ht (001) surface was modeled using a (2 × 2) supercell with a thickness of 9 atomic layers, and Fh (001) surface was modeled using a (3 × 1) supercell with a thickness of 5 atomic layers, and the vacuum thickness being larger than 20 Å in the (001) direction. During optimization, the energy and force converged to 10^{-5} eV per atom and 0.02 eV $Å^{-1}$, respectively. All geometry optimization was performed until all components of residual force were less than 0.02 eV/Å and the iterative energy difference was less than 10^{-5} eV. The energy and force converged to 10^{-5} eV/atom and 0.02 eV/Å during the geometrical optimization, respectively.

A grid of 3 × 3 × 1 Monkhorst–Pack mesh k-points was used to perform the integration in the Brillouin zone. In the Bader, charge density difference and DOS calculation parts, the k points were increased to 5 × 5 × 1 for the (001) surfaces. The interaction energy of the adsorbed PFOA on the iron oxide surface was calculated via:

$$\Delta E = E(\text{PFOA/iron oxide}) - E(\text{iron oxide}) - E(\text{PFOA}) \quad (1)$$

where E refers the respective electronic energy; and the charge density difference was calculated by:

$$\Delta\rho = \rho(\text{PFOA/iron oxide}) - \rho(\text{PFOA}) - \rho(\text{iron oxide}) \quad (2)$$

where ρ(PFOA/iron oxide) is the density of the interacting PFOA−surface system, whereas ρ(PFOA) and ρ(iron oxide) are the densities of the two isolated (non-interacting) subsystems, taken in the same geometry of the interacting system.

3.5. Materials and Methods: Soil Treatment

3.5.1. Chemicals and materials

The Willow Grove field soil samples were air-dried and sieved through the standard sieve of 2 mm openings, and then homogenized through thorough mixing. For each analysis or

experimental uses, at least three subsamples will be taken from different parts of the primary samples. Dispersants Corexit EC9500A was acquired per the courtesy of Nalco Company (Naperville, IL, USA) and SPC1000 was purchased from Polychemical Corporation (Chestnut Ridge, NY, USA). Both dispersants were used as received upon proper dilution. A 500-mg Superclean Envi-18 SPE cartridge was purchased from Sigma-Aldrich (St. Louis, MO, USA) to extract PFAS from various eluents.

3.5.2. Extraction PFAS in the field soil

The soil sample was extracted following the sequential extraction of acidified sediment/soil using methanol at 60 °C and under sonication Higgins et al. [2005]. Briefly, a 500 µL aliquot of the 200 ng mL^{-1} isotopically labeled surrogate (i.e., M8PFOA or M8PFOS) for the target analytes was spiked in 1 g of the homogenized soil sample (surrogate concentration = 100 ng g^{-1}) and vigorously mixed on a horizontal shaker for 4 h before the extraction. Then, the sample was extracted first by adding 10 mL of a 1% acetic acid solution into a 50-mL HDPE vial, which was then treated under sonication at 60 °C in a water batch for 15 min, and then the supernatant was separated per centrifugation at 5000 rpm for 15 min. Upon decanting the supernatant into a second 50-mL HDPE vial, the sample was extracted again using 2.5 mL of a mixture containing 9:1 (v/v) methanol and 1% acetic acid in the original vial under sonication for 15 min at 60 °C. This process of acetic acid washing followed by methanol/acetic acid extraction was repeated one more time. Finally, a 10-mL of 1% acetic acid washing was performed in the same manner. For each sample, all washes and extracts are combined, resulting in a total volume of ~35 mL.

To concentrate the extracts and avoid potential matrix interferences, a solid phase extraction [Higgins et al., 2005] was performed to treat the extract. Briefly, a 500-mg Superclean Envi-18 SPE cartridge was preconditioned with 10 mL of methanol followed by 10 mL of 1% acetic acid at a rate of 1 drop/sec under vacuum. After loading the extract, two 7.5 mL aliquots of DI water were used to rinse the sample vials and drawn through cartridge, and the target analytes (PFOS and PFOA) were eluted with 4 mL methanol at a rate of 1 drop/sec and collected in 1:1 (v/v) methanol/acetone-washed polypropylene vial. The procedure was repeated with a second 4 mL aliquot of methanol. The eluent was then concentrated under a flow of high purity nitrogen to remove all the solvents (water/methanol). Then, appropriate amounts of the 96:4% (vol/vol) methanol:water solution and the internal standards (M4PFOA/PFOS) were added to the collection vial to bring the volume to 2 mL. Upon mixing and full dissolution of PFOS in the solvent, the samples were stored at 4 °C and analyzed for PFAS.

Based the soil analysis, PFOS was the major PFAS for the soil, and hence was followed in the subsequent desorption and photodegradation experiments.

3.5.3. Desorption and successive desorption of PFOS by oil dispersants

Batch desorption experiments were conducted in 43 mL amber glass vials with polypropylene caps. Briefly, 2 g of the homogenized soil were mixed with 40 mL of a desorbing solution containing dispersants Corexit EC9500 or SPC1000 from 50 to 500 mg L^{-1} with or without NaCl. The mixtures were then sealed and rotated on an end-to-end tumbler at 50 rpm. At predetermined times, duplicate vials are centrifuged at 5000 rpm for 15 minutes to separate the soil from the aqueous phase. The supernatant was then spiked with a stock solution of M8PFOA/PFOS to give

a surrogate concentration of 20 μg L^{-1}. Finally, the supernatant was subjected to the SPE cleanup process to minimize the matrix effects on the subsequent analysis.

It is noted that the desorption from the batch experiments was not exhaustive, i.e., it does not presents the maximum amounts of PFAS that can be eluted by a certain desorbing agent. Rather, the method was merely use to screen the most effective desorbing agent based on the equilibrium distribution of PFAS between soil and the liquid phases.

Successive desorption tests were further conducted to determine the maximum desorbable PFOS in the field soil using Corexit EC9500A, which outperformed SPC1000. Following each apparent desorption equilibrium, the vials were centrifuged and supernatants pipetted out, and replaced with 300 mg L^{-1} of fresh Corexit EC9500A. At predetermined times (0, 1, 8, and 24 h), the vials were sacrificially sampled, and the supernatants were analyzed for the PFAS concentration in the aqueous phase following the same procedures as described above. The successive desorption tests were carried out in triplicate to assure data quality.

3.5.4. Re-adsorption kinetics of desorbed PFOS by Ga/TNTs@AC

To reuse the spent dispersant solution, PFOS in the spent solution was removed by adsorption using Ga/TNTs@AC (Ga = 2 wt.%). First, 2 g of PFOS-loaded soil was mixed with 40 mL of solution containing 300 mg L^{-1} of Corexit EC9500A. The mixture was then sealed and rotated on an end-to-end tumbler at 50 rpm. At equilibrium, duplicate vials were sampled and centrifuged at 4000 rpm for 10 minutes to separate the soil from the aqueous phase. Then, the supernatant was transferred into clean vials containing 0.2 or 0.4 g of Ga/TNTs@AC (material dosage = 5 or 10 g L^{-1}) to initiate the re-adsorption. At predetermined times, 1 mL of each supernatant was taken and analyzed for PFOS concentration upon proper QA/AC procedures (see SOP).

3.5.5. Photodegradation of re-adsorbed PFOS by Ga/TNTs@AC and re-use of treated dispersant solution

Following the adsorption equilibrium, PFOS desorbed from the field soil was reloaded on Ga/TNTs@AC. Upon gravity settling, 36 mL of the solution was pipetted out. Then, the remaining mixture of Ga/TNTs@AC + 4 mL dispersant solution was transferred to the quartz UV reactor through 6 mL DI water rinsing, making the total solution volume to 10 mL. The reactor was then placed into the Rayonet chamber photo-reactor (Southern New England Ultraviolet CO., Branford, CT, USA), and the photodegradation was conducted under UV at a wavelength of 254 nm and a light intensity of 21 mW cm^{-2}. After 4 h UV irradiation, the sample vials were taken out and analyzed for the F^- in the aqueous phase and PFOS remaining in the solid phase. The tests were carried out at both material dosages, 5 and 10 g L^{-1} to compare the PFOS degradation and defluorination rates.

The treated dispersant solution was re-used in another cycle of desorption test with the field soil. Briefly, 2 g of the field soil was mixed with the treated dispersant solution, which was replenished with 10% of the fresh dispersant solution (total dispersant solution volume = 40 mL). The PFOS concentration in the aqueous phase was then followed as described above.

3.6. Analytical Methods

In the material screening stage, the aqueous PFAS samples with known high concentrations (part per billion levels) and with insignificant matrix interference were analyzed using an ultra-performance liquid chromatography system coupled with a quadrupole time-of-flight mass spectrometer (UPLC-QTOF/MS) or QTOF and with electrospray ionization (ESI) operated in the negative mode and with Masslynx software (V4.1) (ACQUITY, Waters Corp., USA). The following method was followed. First, 10 µL of a standard or sample is injected in the C18 column (Luna C18(2), particle size = 3 µm, pore size = 100 Å, ID x L = 2 × 50 mm, with a 2 x 4 mm guard cartridge, Phenomenex) with a 200 µL min^{-1} flow rate of mobile phase, which consists of solution A (2 mM ammonium acetate in water pH 4.7) and solution B (100% acetonitrile) beginning at 30% B for the first 0.3 minute then increasing to 95% B at 3.4 min, held at 95% B for 0.7 min, back to 30% B in 1.2 min, and re-equilibration, resulting in a total run time of 7 min. The capillary voltage is set at 2.0 kV, the sample cone voltage is 20 V, and the extraction cone is 4.5 V. The source and desolvation temperatures are maintained at 120 and 400 °C, respectively, with the desolvation gas flow at 800 L h^{-1}. The Time of Flight Mass Spectrometry scan is 1 s from 50 to 600 m/z with a 0.1 s inter-scan delay using the centroid data format. The lock mass is used to correct instrument accuracy with a 0.2 ppm solution of Leucine enkephalin. Ion source parameters such as the source temperature (gas and sample cone), mobile phase flow rate, and cone voltage are fixed throughout the study. Based on our calibration analysis, the detection limits of the QTOF system can reach the sub-ppb levels for PFOA and PFOS, which are acceptable for the screening purpose, where we intended to test the removal of the PFAS from >100 ppb to low ppb levels using various photocatalysts.

PFAS samples with unknown low concentrations (part per trillion levels) and with or without significant matrix interference (including groundwater sample and soil sample) were analyzed using liquid chromatograph with triple quadrupole tandem mass spectrometry (LC-MS/MS) at University of Maryland, Baltimore County (UMBC). The analytical procedure followed the requirements specified in Table B-15 of the latest DoD QSM 5.3 manual. Briefly, PFOA, PFOS, and their mass labelled IS are measured with an UltiMate 3000 LC connected to a Thermo TSQ Quantum Access Max triple quadrupole MS/MS (Thermo; Waltham, MA). Samples (50 µL) are injected into a Waters XBridge BEH C18 column (2.1×150 mm, 2.5 µm) with a guard column (2.1×5 mm, 2.5 µm) containing the same material. The analytes are separated using a 6-minute isocratic elution scheme employing 65% methanol with 0.1% ammonium hydroxide and 35% water with 0.1% ammonium hydroxide (pH 10.5). The column temperature is set at 40 °C, and the eluent flow rate is 200 µL min^{-1}. The negative electrospray ionization mode is employed for all compounds and at least one product ion is selected for quantitation. A DI water sample and another sample with known PFAS concentrations (both spiked with isotopes IS) are analyzed along with other samples for each batch as QC check and to correct bias caused by shipment. After samples are delivered, the PFAS concentration in DI water sample must be lower than 1/2 LOQ and concentration of the sample with known PFAS concentration must be within ± 10% of its true value. Failure in these criteria will lead to sample re-preparation.

The concentrations of F^- was determined using a Dionex ion chromatograph (IC) (DX-120) equipped with anion exchange column (Dionex Ionpac AS22, including analytical column and guard column) and an anion dynamically regenerated suppressor (ADRS 600, 4mm). The anions were eluted isocratically at a flow rate of 1.0 mL min^{-1} using a carbonate/bicarbonate eluent. The eluent was prepared according to the manufacturer's recommendation (4.5 mM Na_2CO_3, 1.4 mM $NaHCO_3$). The injection volume is 50 µL and three replicate injections were used for each sample.

The same IC method was employed to analyze chloride, sulfate, nitrate and phosphate ions. In addition, a fluoride selective electrode (VWR® fluoride ISE Electrodes, VWR International, Radnor, PA, USA) were used to rapidly measure the F^- production during photodegradation. The results were confirmed by comparing with those obtained using the IC method.

The standard operating procedure (SOP) provides more details about the analytical methods and the associated QA/QC procedures. The SOP has been submitted as a separate document.

Because of complex nature of the degradation products, it was not our intention to quantify all the intermediate products in this limited scope project. Rather, fluorine in the intermediates was derived based on the difference between the initial fluorine mass and fluorine remaining and fluoride generated after the photocatalytic degradation, namely,

Fluorine in intermediates = Initial Fluorine in PFOA/PFOS – Fluorine in residual PFOA/PFOS – Fluoride

where Fluorine in PFOA/PFOS and Fluoride were analyzed as described in the standard operating procedure (SOP).

Tables A1-A3 in **Appendix 7.2** present the QA/QC supporting data relevant to the PFOA and PFOS analyses, which were carried out at UMBS using LC-MS/MS. Details on the limits of detection (LODs) and limits of quantitation (LOQs) for target PFAS are provided in Table III-2, Part III in the SOP (Pages 39-40). For aqueous samples, the LOD and LOQ of PFOA after isotope dilution (*e.g.*, 10× dilution) were 0.06 μg/L and 0.20 μg/L, respectively; furthermore, the LOD and LOQ of PFOS were 0.03 μg/L and 0.10 μg/L, respectively. For aqueous samples with a 10-mL loading volume (processed by solid-phase extraction (SPE)), the LOD and LOQ of PFOA were 0.006 μg/L and 0.020 μg/L, respectively; furthermore, the LOD and LOQ of PFOS were 0.003 μg/L and 0.010 μg/L, respectively. For the solid samples, the LOD and LOQ of PFOA were 0.6 ng/g and 2.0 ng/g, respectively; and the LOD and LOQ of PFOS were 0.3 ng/g and 1.0 ng/g, respectively. Note that all solid-phase PFAS concentrations are reported on a dry-weight mass basis.

The QA/QC checks for spikes, method blanks, matrix spikes, and matrix spike duplicates were discussed in Section 5.1.1 for isotope dilution analyses and Section 5.1.2 for SPE-based analyses of the SOP. The actual spiked recoveries for the aqueous samples were presented in Figure III-1 in the SOP.

For the QTOF analysis conducted at Auburn University, the LODs and LOQs for PFOA and PFOS are provided in Part II in the Section 3.4. (Page 19) and Section of 5.4 (Page 24). The LOD and LOQ for PFOA and PFOS are 1 and 5 μg/L respectively. The QA/QC checks for the QTOF analysis are discussed in Section 7.2 (Pages 29-31) and Section 8.1 (Pages 31-32) of the SOP. The correlation between peak area and concentration of PFOA and PFOS with a 20 μg/L internal standard (^{13}C8 PFOA, ^{13}C8 PFOS) are presented in Figures II-1 and II-2, respectively, on page 32 of the SOP, which also give the actual spiked recoveries for the aqueous PFOA and PFOS in DI water (**Table A3**). Both PFOA and PFOS showed high R^2 values (>0.99), indicating high spiked recoveries. **Tables A3-A4** in **Appendix 7.2** provide the detailed QA/QC data related to the QTOF analyses.

4. Results and Discussion

In accord with the Material and Methods, the Results and Discussion are organized based on the photocatalysts used and the media treated, namely, in the order of Fe/TNTs@AC, Ga/TNTs@AC, FeO/CS, and soil treatment.

To assure data quality, all experiments and analyses were carried out at least in duplicate. In this report, all data are presented as mean of replicates with errors/error bars indicating standard deviations or relative deviation to the mean.

4.1. Results and Discussion: Fe/TNTs@AC

4.1.1. Synthesis and characterization of Fe/TNTs@AC.

Figure 8a shows a digital picture of the as-prepared iron-doped, AC-supported titanate nanotubes (Fe/TNTs@AC). The physical size and shape mimic those of typical powder activated carbon (PAC), though the surface is functionalized with the photoactive Fe-doped TNTs. Figure 8b shows carbon nanoparticles (the dark dots) were attached on the TNTs, with a particle size in the range of 5 to 20 nm, indicating that upon the alkaline hydrothermal treatment, some carbon broke into nanoscale carbon particles. The carbon nanoparticles not only facilitate adsorption of PFAS through enhanced hydrophobic interactions, but facilitate electron transfer to result in enhanced photoactivity. Figures 8c and 8d present close-up TEM images of the Fe- and carbon modified TNTs. The iron and carbon modifications are expected to enhance both adsorption and photodegradation of PFAS. Figures 8b and 8d also reveal that the TNTs have an outer diameter of ~20 nm and a length of ~100 nm.

Figure 9a presents an SEM image of Fe/TNTs@AC, displaying a cotton-like surface structure consisting of interwoven carbon- and Fe-modified TNTs. This structure is expected to be conducive to concentrating PFAS on the outer-shell surface and thereby facilitate the subsequent photocatalytic destruction of PFAS *in situ*. For comparison, the parent F-400 GAC (not shown) shows a flat, smooth, and layered-structure, where adsorption is expected to penetrate deep into the internal pores. **Figure 9b** shows the EDS spectra of Fe/TNTs@AC, confirming the presence of the five major elements (C, O, Na, Fe, and Ti) on the surface of Fe/TNTs@AC. **Figure 10** presents EDS mappings of the elements, indicating that a small amount of Fe is well distributed on the surface of Fe/TNTs@AC, while Ti and C are the predominant elements. **Table 1** gives the relative percentiles of the elements.

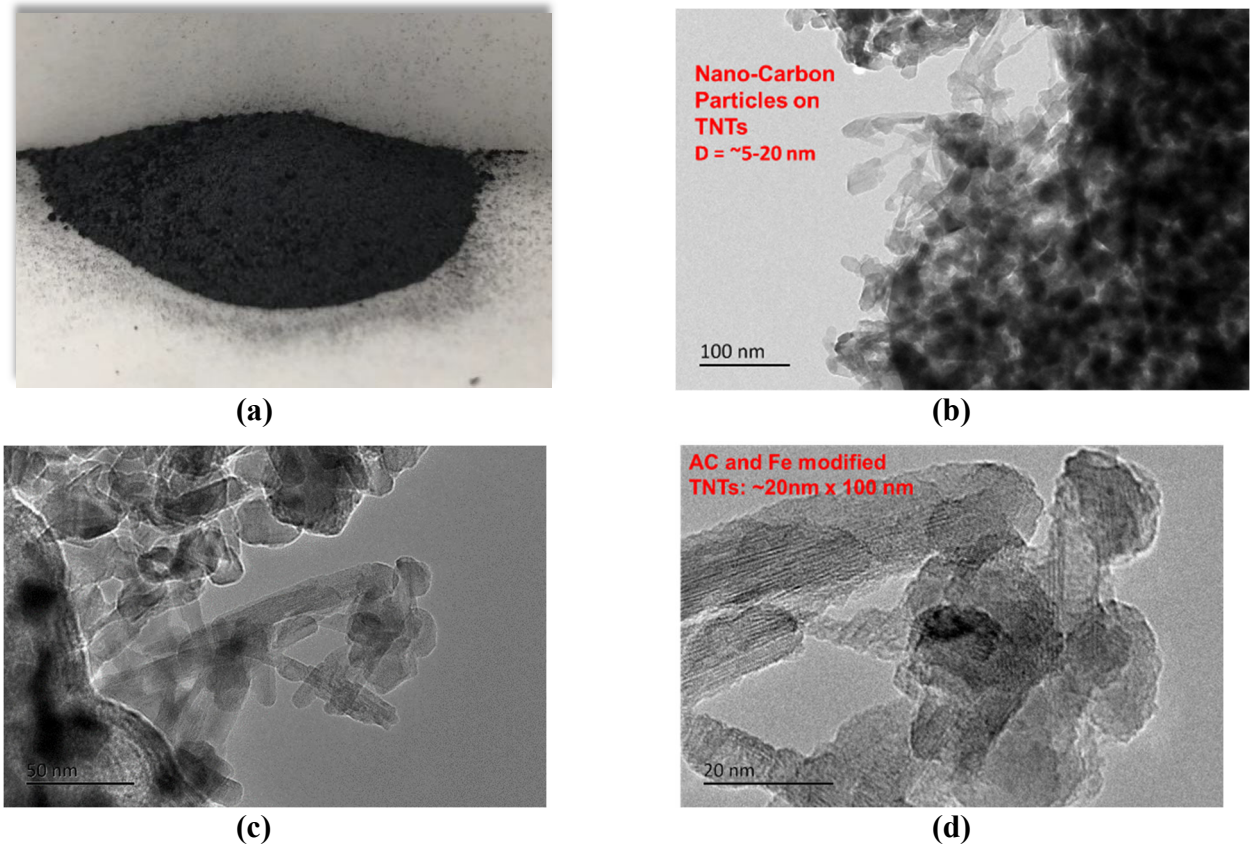

(a) **(b)** **(c)** **(d)**

Figure 8. **(a)** A digital image of Fe/TNTs@AC prepared based on commercial activated carbon (AC) and TiO_2 through an alkaline hydrothermal process (AC:TiO_2 mass ratio = 1:1, Fe = 1 wt.% of TNTs@AC); **(b)** TEM images of nanoscale AC particles attached on titanate nanotubes (TNTs); and **(c)** and **(d)** Close-up TEM images of iron- and AC-modified TNTs with FeO patched on TNTs.

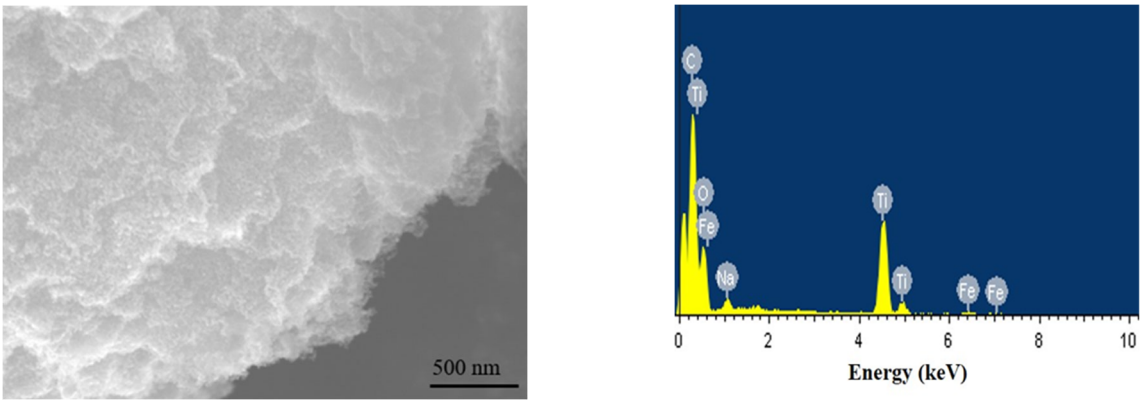

(a) **(b)**

Figure 9. SEM image of **(a)** TNTs@AC and **(b)** EDS spectra of Fe/TNTs@AC.

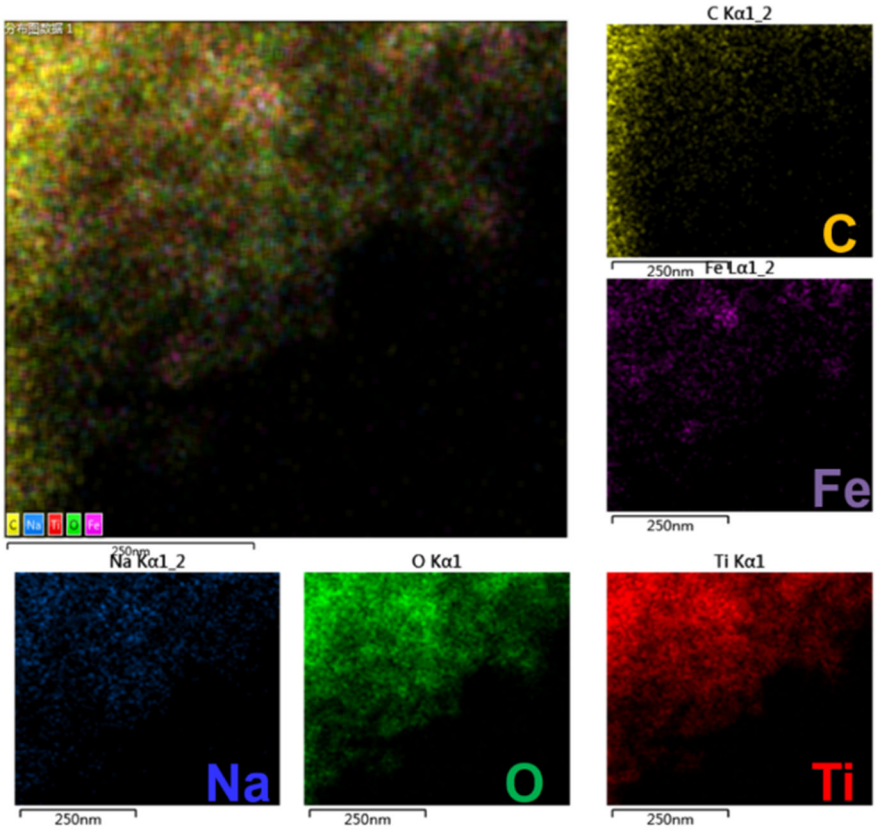

Figure 10. SEM-EDS mapping of the elements of Fe/TNTs@AC.

Table 1. Atomic compositions of Fe/TNTs@AC.

Element	Weight, %	Atomic, %
C	53.02	65.75
O	30.89	28.76
Na	1.51	0.98
Ti	13.99	4.35
Fe	0.59	0.16
Totals	100.00	100.00

Figure 11a shows the XRD patterns of F-400 GAC, TNTs@AC, and calcined Fe/TNTs@AC. Table 2 summarizes the six crystalline phases identified by the XRD analysis, where quartz-SiO_2 and moissanite (SiC) are likely due to the impurities from the parent AC. For F-400 AC, the two major peaks at 26° and 43° are assigned to the diffractions of crystal planes of graphite (002) and (100), respectively [Quiñones et al., 2014, Rey et al., 2012]. For TNTs@AC, the peaks at 9.2°, 24.1°, 28.1°, 48.4°, and 61.4° are attributed to sodium tri-titanate (expressed as $Na_xH_{2-x}Ti_3O_7$), which is composed of corrugated ribbons of triple edge-sharing [TiO_6] as skeletal structure with

cation (*e.g.*, Na^+, H^+, Fe^{3+}) located at interlayer [Chen et al., 2002; Liu et al., 2016; Ma et al. 2017]. In particular, the peak at 9.2° signifies the interlayer distance (crystal plane (020)) of sodium tri-titanate [Sun and Li 2003]. Furthermore, the peak at 26° represents crystal planes of graphite (002) suggesting that AC is intermingled with TNTs [Liu et al. 2016]. For Fe/TNTs@AC, the peaks at 24.1°, 36.6°, 46.2°, 52.4°, 60.2°, and 73° are ascribed to anatase [Li et al., 2018]; and the peaks at 26.1° and 31.4° belong to graphite (crystal planes (002)) and hematite (α-Fe_2O_3, crystal plane (104)) [Sivula et al., 2011], respectively. Evidently, upon calcination and Fe-doping, the sodium tri-titanate of TNTs@AC was transformed to anatase. This observation agrees with the EDS mapping data.

The HR-TEM images in **Figure 11b** display the layered crystalline structures of TNTs and Fe_2O_3 on the calcined Fe/TNTs@AC, revealing an interlayer distance of 0.35 nm for anatase and 0.27 nm for Fe_2O_3. The interlayer distance for anatase is much smaller than that for neat TNTs (0.75 nm for the crystal plane (020) of titanate), and 0.79 nm for unmodified TNTs@AC [Liu et al., 2016], indicating the iron modification and calcination greatly altered the crystalline structure of TNTs@AC.

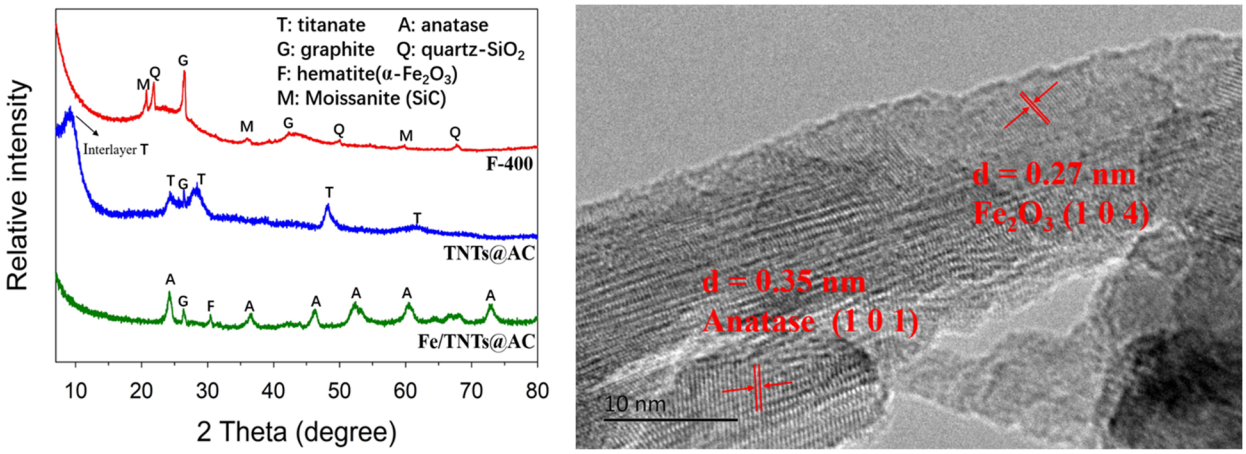

(a) **(b)**

Figure 11. **(a)** XRD patterns of F-400 GAC, TNTs@AC, and Fe/TNTs@AC calcined at 550 ºC; and **(b)** High resolution TEM images of TNTs and iron oxide crystals of Fe/TNTs@AC calcined at 550 ºC

Table 2. XRD pattern powder diffraction file (PDF) number.

Crystal Phase	**PDF #**
Graphite	41-1487
Titanate	48-0693
Anatase	21-1272
Quartz-SiO_2	46-1045
Moissanite (SiC)	42-1360
Hematite (α-Fe_2O_3)	33-0664

Figure 12 displays X-ray photoelectron spectroscopy (XPS) spectra of Fe/TNTs@AC, and **Table 3** lists the corresponding atomic compositions of Fe/TNTs@AC and TNTs@AC. In a previous work [Liu et al., 2016], we identified that the formula of TNTs can be expressed as $Na_{0.7}H_{1.3}Ti_3O_7$. On the basis of carbon content in AC (60.11%) and Ti mass added, the overall mass ratio of AC to TNTs in the TNTs@AC is ~1.2:1. After Fe doping and calcination, the C content decreased from 60.11% to 51.08%, while the contents of Ti and O increased from 8.35% to 11.34% and from 24.40% to 30.52%, respectively. Meanwhile, the XPS data also indicated an Fe content of 0.68%, which was close to the EDS-based value (0.59%).

Figure 12b shows the high resolution XPS spectra of Fe 2p, where the two main peaks, located at ~710 and ~723 eV, correspond to Fe $2p_{3/2}$ and Fe $2p_{1/2}$, respectively [Wu et al. 2015]. This observation confirmed that Fe(II) was converted to Fe(III) resulting in the α-Fe_2O_3 phase, which is consistent with the TEM and XRD observations.

Table 3. Surface atomic percentage of AC and TNTs@AC obtained by XPS.

Materials	**Element atomic percentage (%)**					
	C	**O**	**Na**	**Ti**	**Fe**	**Cl**
TNTs@AC	60.11	24.40	5.14	8.35	0	2.01
Fe/TNTs@AC	51.08	30.52	5.42	11.34	0.68	0.95

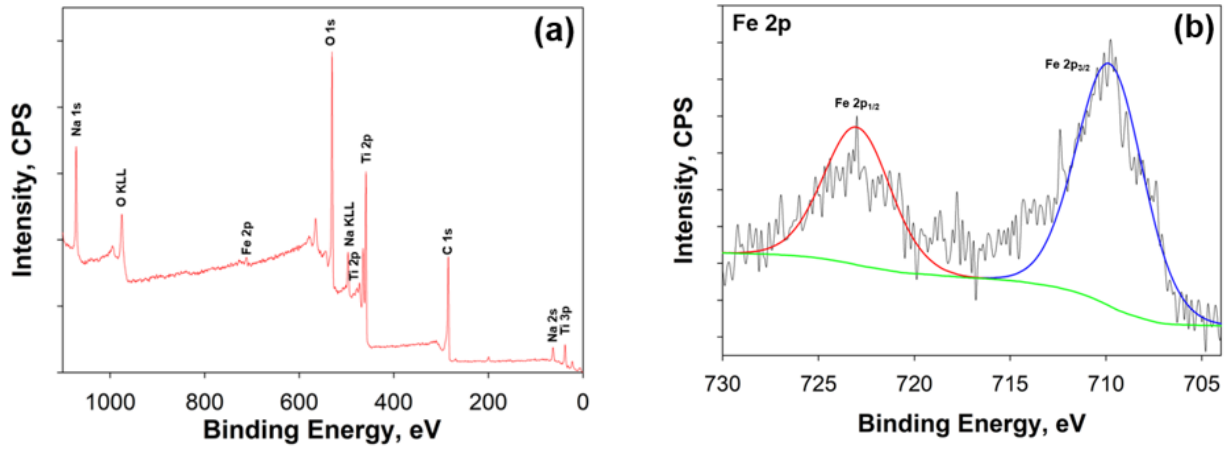

Figure 12. XPS spectra of Fe/TNTs@AC: **(a)** Survey XPS, and **(b)** high resolution of Fe 2p.

Figure 13a shows the N_2 adsorption-desorption isotherms for unmodified TNTs@AC and Fe/TNTs@AC, which revealed that the Fe loading and the calcination treatment of TNTs@AC lowered the BET surface area from 348.5 m^2 g^{-1} for unmodified TNTs@AC to 292.1 m^2 g^{-1} for Fe/TNTs@AC. This meets our initial design to shut off the adsorption sites in the deep pores so that PFAS can be accumulated/concentrated on the exterior sites that are more accessible by light or photo-generated reactive species.

Figure 13b shows pore size distribution of TNTs@AC and Fe/TNTs@AC. TNTs@AC displayed a bimodal pore size distribution profile with a primary peaking at ~4 nm and a secondary peaking at 2−2.5 nm. The pore size distribution from 4 to 10 nm mimics that of the parent AC, whereas the pore size distribution for <4 nm pores can be attributed to conversion of larger pores (>10 nm) of TNTs into more micropores in TNTs@AC. The similar distribution profile was observed for Fe/TNTs@AC. However, Fe/TNTs@AC showed a much higher change in dV/dD from ~4 nm to ~10 nm than TNTs@AC, suggesting that loading of Fe and calcination blocked some large and deep pores. Contrary to the BET surface area, the Fe loading and the calcination treatment of TNTs@AC increased the pore volume from 0.55 cm^3 g^{-1} for TNTs@AC to 0.61 cm^3 g^{-1} for Fe/TNTs@AC, which is in favor of rapid adsorption rate for PFAS.

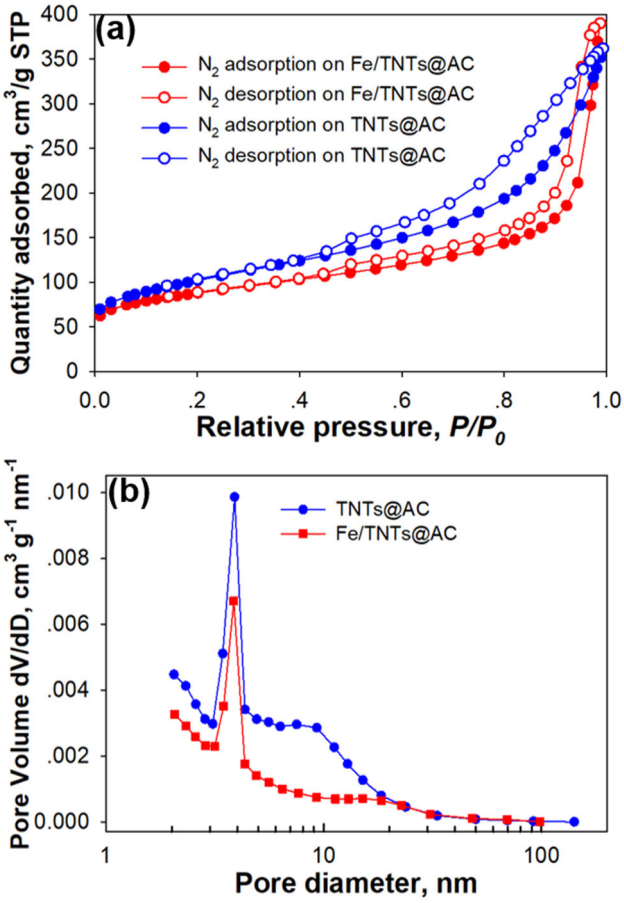

Figure 13. (a) N_2 adsorption-desorption isotherms, and **(b)** pore size distributions of unmodified TNTs@AC and Fe/TNTs@AC. V: Pore volume, and D: pore diameter.

4.1.2. Effects of calcination temperature and Fe content on photoactivity of Fe/TNTs@AC

Material calcination has been often practiced to enhance the activity of photocatalysts. In search for a proper calcination temperature for Fe/TNTs@AC, the material was calcined at 300, 550, 650, and 850 ºC, and tested for defluorination of PFOA under UV irradiation. **Figure 14a** shows that Fe/TNTs@AC calcined at 550 °C displayed the highest defluorination rate, with ~62% fluorine in PFOA converted to F^- ions in 4 h of UV irradiation. Increasing the temperature to 650 °C and 850 °C decreased the defluorinate to 57% and 16%, respectively. Conversely, lowering the

calcination temperature to 300 °C resulted in only 37% defluorination. Thus, 550 °C was considered the optimal calcination temperature for Fe/TNTs@AC prepared under the given recipe.

It has been reported that titanate begins to be transferred into the anatase phase at 190 °C [Mao and Wong, 2006]. As the calcination temperature increases, the formed anatase phase would have larger crystallites with the ability to absorb a broader range of light [Yang et al., 2008]. However, when calcination temperature further increases to 600 °C, anatase starts to transform to the rutile phase, which has lower photocatalytic activity than the anatase phase [Yang et al., 2008]. Thus, the best calcination temperature range falls between 500 to 600 °C. However, the effect of the calcination temperature on the carbon coatings was not explored in this limited-scope study.

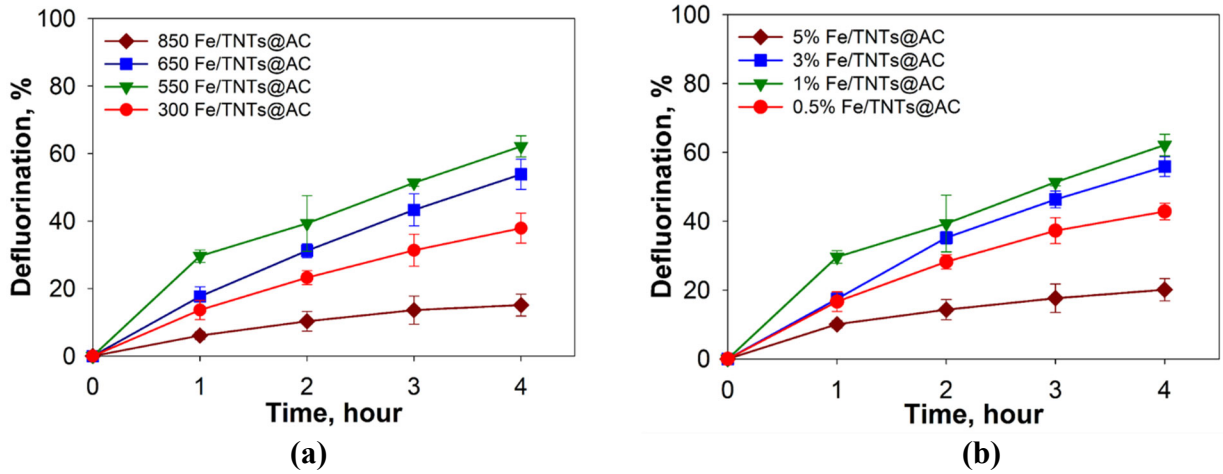

Figure 14. Defluorination of PFOA by Fe/TNTs@AC with **(a)** different calcination temperatures, and **(b)** various Fe contents. Experimental conditions: initial [PFOA] = 100 μg L^{-1}, material dosage = 1.0 g L^{-1}, solution volume = 40 mL, pH = 7.0 ± 0.3; photocatalytic defluorination was conducted under UV light (λ=254 nm, intensity = 21 mW cm^{-2}).

Iron oxide is one of the most desired adsorbents and photocatalysts for wide availability, low cost and environmental friendliness. Yet, iron oxide alone cannot degrade PFAS. The Fe impregnation was expected to facilitate interactions with the anionic head groups of PFOA and PFOS, and to enhance photocatalytic activity of Fe/TNTs@AC by improving the light absorption, electron transfer and generation of radicals. As the photo-activation occurs at the material surface, only a small fraction of Fe is needed. In order to preliminarily optimize the Fe content, photocatalytic defluorination of PFOA was tested using Fe/TNTs@AC prepared with 0.5%-5% of Fe. **Figure 14b** shows that Fe/TNTs@AC with 1% of Fe offered the highest defluorination rate, with a 4 h defluorination of ~62%. However, further increasing the Fe content to 3%–5% decreased the defluorination extent to 57% and 20%, respectively. Conversely, lowering the Fe content to 0.5% resulted in only 43% of PFOA defluorinated. Although increasing Fe doping could neutralize the negatively charged surface of TNTs@AC and facilitate PFOA adsorption, an excess of Fe would act as recombination centers for the photo-generated electrons and holes due to quantum tunneling effects [Zhang and Lei, 2008; Zhou et al., 2006], resulting in reduced photodegradation rates. Moreover, excessive loading of Fe_2O_3 on the TNTs surface may hamper the photocatalytic activity of anatase.

It is noted that multiple factors can affect the material performance, including the TNTs:AC:Fe ratio, calcination temperature, hydrothermal treatment temperature, properties of AC, Fe type and content, and synthesis procedure. As such, further more sophisticated material optimization can be carried out through proper experimental design (e.g., the full factorial experiment method). IN other words, there is still plenty of room to further improve the adsorption and photocatalytic properties of Fe/TNTs@AC.

4.1.3. Adsorption and photodegradation of PFOA and PFOS by Fe/TNTs@AC

Fe/TNTs@AC exhibited excellent adsorption rate and photocatalytic activity for both PFOA and PFOS. **Figure 15a** shows adsorption kinetics of PFOA by neat AC, treated AC and Fe/TNTs@AC. While Fe/TNTs@AC removed >95% of PFOA (100 μg L^{-1}) in just 5 min, and >99% after 60 min, AC and treated AC removed only ~73% and ~85% of PFOA after 120 min, respectively, indicating a much faster adsorption rate of Fe/TNTs@AC over the parent AC. The rapid adsorption allows for efficient removal of PFOA from bulk water with a small hydraulic residence time (HRT) (i.e., a small reactor). Moreover, the adsorption pre-concentrates PFAS from a large volume of water onto a small volume of Fe/TNTs@AC, enabling the subsequent photocatalytic degradation to be carried out in a much smaller volume of photo-reactor with much less energy consumption compared to directly treating the bulk raw water.

Figure 15b shows that Fe/TNTs@AC was able to highly efficiently degrade PFOA (i.e., breakdown into other compounds), and >90% of pre-concentrated PFOA was photodegraded in 4 h. Moreover, **Figure 15c** shows that Fe/TNTs@AC was able to completely destroy or defluorinate (i.e., converted into F^- ions) >62% of PFOA upon 4 h of the UV irradiation, while neat AC and treated AC defluorinated only ~4% and ~3% after 4 hours of the same UV irradiation, respectively. It should be noted that in this preliminary study, the adsorption was carried out in batch reactors, where the material capacity was not fully utilized. In practice, the treatment can be further optimized. For instance, the adsorption can be performed using fixed-bed columns, which may treat much more volumes of water. A great concentrating factor represents more budget savings. Likewise, the photodegradation reactor can be further optimized. Likewise, the photodegradation can be further improved by optimizing factors such as material synthesis, dosage, and reaction chemistry.

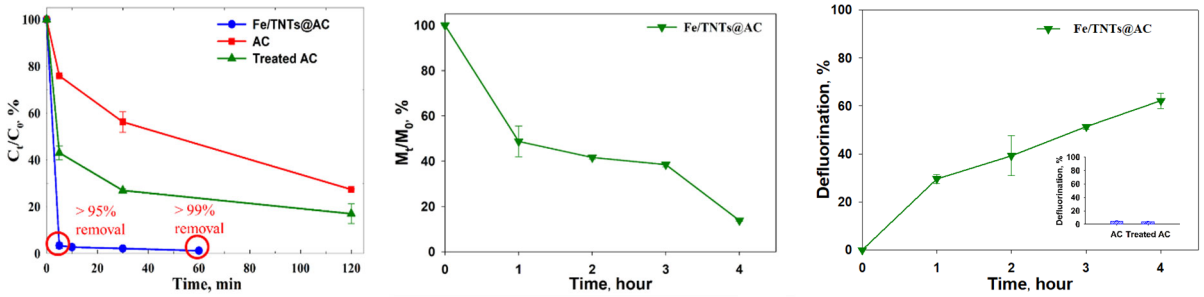

(a) (b) (c)

Figure 15. **(a)** Adsorption, **(b)** photodegradation, and **(c)** defluorination kinetics of PFOA by Fe/TNTs@AC. Experimental conditions: initial [PFOA] = 100 μg L^{-1}, material dosage = 1.0 g L^{-1}, solution volume = 40 mL, and pH = 7.0 ± 0.3. Photodegradation conducted under UV (λ=254 nm, 21 mW cm^{-2}). *Degradation*: transformation or breakdown of PFAS into other compounds; *Defluorination*: conversion of fluorine into fluoride ions. M_0: initial mass of PFOA in the

material, and M_t: PFOA remaining at time t.

PFOS has been known to be more persistent and more adsorptive than PFOA. **Figure 16a** shows that Fe/TNTs@AC removed >99% of PFOS from water within just 5 min of contact time. When subjected to the mild UV irradiation (λ=254 nm, intensity = 21 mW cm^{-2}), ~88% of the preloaded PFOS was degraded within 4 h, of which 46% was defluorinated. Although not fully optimized, the results clearly unveil the potential of the proposed "Concentrate-&-Destroy" strategy using the dual-mode composite material.

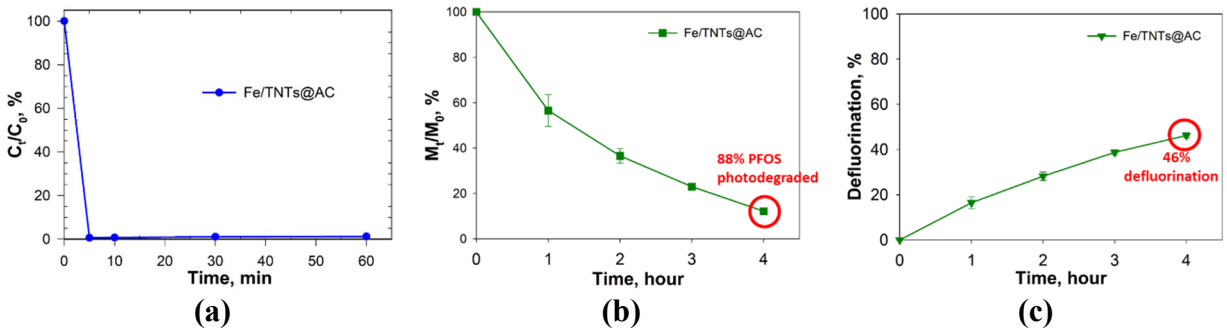

Figure 16. **(a)** Adsorption, **(b)** photodegradation, and **(c)** defluorination kinetics of PFOS by Fe/TNTs@AC. Experimental conditions: initial [PFOS] = 100 μg L^{-1}, material dosage = 2.0 g L^{-1}, solution volume = 40 mL, and pH = 7.0 ± 0.3. Photodegradation conducted under UV (λ=254 nm, intensity = 21 mW cm^{-2}).

Figure 17 shows the PFOA adsorption isotherm for Fe/TNTs@AC. The classical Langmuir model and Freundlich model were applied to interpret the experimental data. While both models can adequately fit the data, the Freundlich model (R^2 = 0.991) offered slightly better goodness of fit based on the coefficient of determination (R^2) than the Langmuir model (R^2 = 0.972), which can be attributed to its better catching of the data at higher concentrations. Mechanistically, PFOA as a surfactant may be adsorbed in monolayer (at low concentration) or multiple layers (at elevated concentration or upon formation of hemi-micelles). The maximum Langmuir adsorption capacity of PFOA by Fe/TNTs@AC was derived to be 88.9 mg g^{-1} from the model fitting. While neat TNTs offered no adsorption for PFOA, the maximum capacity for Fe/TNTs@AC was slightly lower than that for the parent AC (F-400), which was reported to be 112.1 mg g^{-1} [Ochoa-Herrera and Sierra-Alvarez, 2008]. It is noteworthy that the equilibrium uptake of PFOA by Fe/TNTs@AC in the low concentration range (< 5 mg L^{-1}) was comparable or even better than that for the parent AC (not shown). Given that some of the deep adsorption sites for Fe/TNTs@AC were lost due to reduced BET surface area, the isotherm data indicate a higher selectivity for PFOA by Fe/TNTs@AC especially in the low PFOA concentration range, which is typical in real world applications.

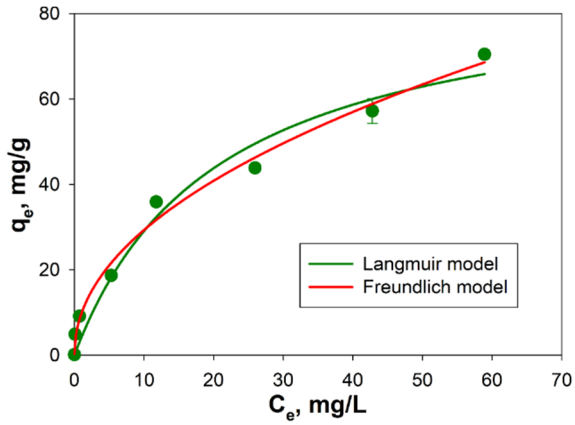

Figure 17. Adsorption isotherm of PFOA by Fe/TNTs@AC. Experimental conditions: initial [PFOA] = 100 μg L^{-1} – 150 mg L^{-1}, material dosage = 1.0 g L^{-1}, solution volume = 40 mL, and pH = 7.0 ± 0.3, temperature = 22 ± 1 °C, and reaction time = 24 h.

4.1.4. Reusability of Fe/TNTs@AC

Figure 18 shows that when Fe/TNTs@AC was repeatedly used in six consecutive cycles of adsorption-photodegradation without chemical regeneration, namely, the efficient photodegradation of pre-concentrated PFOA also regenerates the material. PFOA adsorption remained high (>99% removal), and the defluorination rate kept at ~60%. Evidently, Fe/TNTs@AC can be reused in multiple cycles without additional regeneration need. This important feature represents a great advancement of conventional adsorbents (AC or ion exchange resins), which require costly regeneration and subsequent treatment of the spent regenerant wastes. The slight increase in defluorination with the cycle time is attributed to the additional defluorination of intermediate products from the previous cycles. Indeed, short-chain PFAS were detected on Fe/TNTs@AC during the photodegradation process (see **Section 4.1.5**).

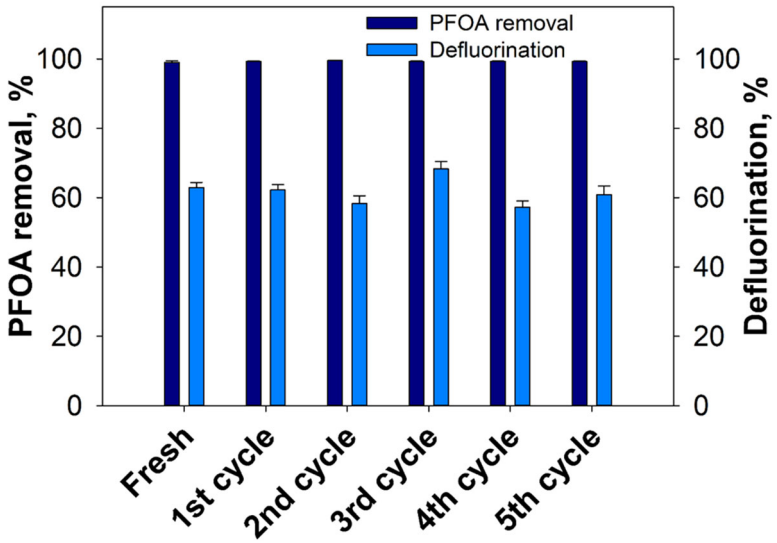

Figure 18. Reusing Fe/TNTs@AC in six consecutive cycles of adsorption-photodegradation of PFOA. Experimental conditions are the same as in Figure 15.

4.1.5. Mechanisms for enhanced adsorption and photodegradation of PFAS by Fe/TNTs@AC

The experimental data indicate that the adsorption rate, capacity and photocatalytic activity of Fe/TNTs@AC far exceed those of conventional Ti-based photocatalysts such as TiO_2 or TNTs. The "Concentrate-&-Destroy" process using Fe/TNTs@AC proceeds in the following key steps: 1) Adsorption of PFAS on the photoactive sites of the material, 2) Activation of the photocatalysts under UV or solar light, and 3) Decarboxylation and/or defluorination of PFAS by photo-activated holes and/or electrons as well as photo-generated reactive species. As such, both adsorption (rate, capacity and molecular orientation of adsorbed PFAS) and photocatalytic (redox potential, band energy gap, e-h recombination, and generation of radicals) properties can affect the degradation effectiveness.

Figure 19 shows a LC-QTOF-MS chromatogram displaying the intermediate products during the photodegradation of PFOA Fe/TNTs@AC. The peaks at the m/z values of 413, 363, 313, 263, 213, 163, and 113 were assigned to various PFOA and shorter chain PFCAs, including PFHpA, PFHxA, PFPeA, PFBA, PFPA, and TFA anions, respectively. In addition, the degradation products of PFOA, namely PFHpA, PFHxA, PFPeA, PFBA, and PFPA were also identified at 369, 319, 269, 219, 169, and 119, respectively. This observation suggests that the PFOA degradation proceeds in the stepwise chain-shortening manner, which has been reported for conventional Ti- or anatase-based photocatalysts, and is consistent with observations by Tang et al. [2012] and Chen et al. [2007].

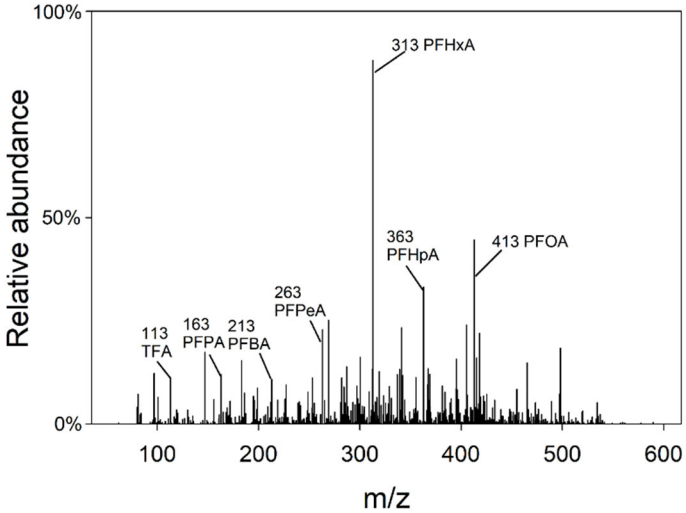

Figure 19. A LC-QTOF-MS chromatogram showing intermediate products during photodegradation of PFOA by Fe/TNTs@AC. Experimental conditions: initial [PFOA] for adsorption = 1 mg L^{-1} (>95% PFOA was adsorbed), material dosage = 2.0 g L^{-1}, solution volume = 40 mL, pH = 7.0 ± 0.3, temperature = 23 ± 1 °C, and UV (λ=254 nm, intensity = 21 mW cm^{-2}) irradiation time = 2 h.

Based on the latest theory for standard Ti-based materials [Panchangam et al., 2018; Peng et al., 2017] and the observed intermediates, the PFOA photodegradation by Fe/TNTs@AC proceeds through the following stepwise defluorination process:

$$CF_3(CF_2)_6COO^- + \equiv FeOH_2^+ \rightarrow CF_3(CF_2)_6COO^- \equiv FeOH_2^+ \quad (3)$$

$$TNTs + h\nu \rightarrow h^+ (VB) + e^- (CB) \quad (4)$$

$$CF_3(CF_2)_6COO^- + h^+ (VB) \rightarrow C_7F_{15}COO^\bullet \quad (5)$$

$$C_7F_{15}COO^\bullet \rightarrow {}^\bullet C_7F_{15} + CO_2 \quad (6)$$

$${}^\bullet C_7F_{15} + {}^\bullet OH \rightarrow C_7F_{15}OH \text{ or } {}^\bullet C_7F_{15} + H_2O \rightarrow C_7F_{15}OH + H^+ \quad (7)$$

$$C_7F_{15}OH \rightarrow C_6F_{13}COF + H^+ + F^- \quad (8)$$

$$C_6F_{13}COF + {}^\bullet OH \rightarrow C_6F_{13}COO^- + H^+ + F^- \quad (9)$$

First, PFOA anions are adsorbed the impregnated iron (hydr)oxide nanoparticles through concurrent electrostatic and Lewis avid-base interactions (Eq. 3). Second, the adsorbed PFOA is oxidized by the photo-generated holes (h^+) (Eqs. 4-5) to form the unstable perfluoroalkyl radical ($C_7F_{15}COO^\bullet$), which decomposes into ${}^\bullet C_7F_{15}$ through a photo-Kolbe-like decarboxylation reaction with the head (COO^-) group cleaved (Eq. 6). The resulting ${}^\bullet C_7F_{15}$ radicals are further decomposed via reactions with $OH^\bullet$ radicals and hydrolysis reaction (Eq. 7). The resulting $C_7F_{15}OH$ is highly unstable, leading to the cleavage of a C-F bond and release of one fluoride ion (Eq. 8). The intermediate product $C_6F_{13}COF$ is easily attacked by ${}^\bullet OH$ radicals, which are produced abundantly by Fe/TNTs@AC, resulting in the shorter-chain PFCA (Eq. 9). The shorter-chain product $C_6F_{13}COO^-$ undergoes the same decarboxylation/defluorination cycle, each of which eliminating one carbon and two fluorine atoms (CF_2).

It should be noted that because the reaction starts with the head group decarboxylation, the introduction of iron plays a critical role as it can attract the head groups of PFOA to the vicinity of the photoactive sites, rendering the subsequent photodegradation much more favorable.

In addition to the anatase-facilitated photodegradation mechanism, Fe/TNTs@AC offers an additional degradation pathway thanks to the impregnation of iron (hydr)oxide as depicted by Eqs. (10)-(16). The holes generated from photo-activation of iron oxide can directly oxidize PFOA, resulting in the $CF_3(CF_2)_5CF_2^\bullet$ radical upon decarboxylation. In addition, the redox reactions between Fe(III) and photo-generated holes/electrons also facilitate production of ${}^\bullet OH$ radicals and prevent electron-hole recombination, leading to much enhanced photodegradation effectiveness.

$$CF_3(CF_2)_6COO^- \equiv Fe(OH)_2^+ + h\nu \rightarrow CF_3(CF_2)_5CF_2^\bullet + CO_2 + \equiv FeOH_2 \quad (10)$$

$$\equiv Fe(OH)_2 + h^+ \rightarrow \equiv Fe(OH)_2^+ \quad (11)$$

$$\equiv Fe(OH)_2 + O_2 \rightarrow \equiv Fe(OH)_2^+ + O_2^{\bullet -} \quad (12)$$

$$Fe^{3+} + h^+ \rightarrow Fe^{4+} \quad (13)$$

$$Fe^{4+} + OH^- \rightarrow Fe^{3+} + {}^\bullet OH \quad (14)$$

$$Fe^{3+} + e^- \rightarrow Fe^{2+} \quad (15)$$

$$Fe^{2+} + O_2 \rightarrow Fe^{3+} \quad (16)$$

Earlier, Birben et al. [2017] reporeted that Fe(III) can react with photo-generated holes (h^+) to form Fe(IV), which can further react with hydroxide under alkaline condition, producing Fe(III) and hydroxyl radicals (Eqs. 13-14). Meanwhile, Fe(III) can react with photo-generated electrons

to form Fe(II) (Eq. 15), which can be further regenerated to Fe(III) (Eq. 16). This Fe cycle plays an important role in facilitating the PFOA photodegradation. Yet, the Fe concentration needs to be well controlled. If the concentration of Fe is too high, Fe(III) may act as recombination centers through quantum tunneling [Zhang et al., 1998; Zhou et al., 2005], resulting in reduced photo-activity; if the concentration is too low, the role of Fe may not be fully utilized. Since the photodegradation of PFOA took place at neutral pH, dissolved O_2, rather than the hydroxyl radicals (which requires alkaline condition) should be the major oxidizing agent facilitating the Fe(III)-Fe(II) cycle.

Overall, the enhanced adsorption and photodegradation are attributed to: 1) the carbon nanoparticles facilitate hydrophobic interactions with the PFOA tail, 2) the carbon coating also facilitates electron transfer and prevents electron-hole recombination in the photocatalyst, 3) the Fe(III) coating suppresses surface negative potential and enhances the interactions between the holes and the PFOA head groups (carboxylate), 4) the presence of Fe(III) also facilitates a series of redox reactions that facilitate production of $^{\bullet}OH$ radicals and prevent e-h recombination, and 5) because of the lower band energy gap of iron oxide, the Fe-doping enhances absorption of more visible light.

Figure 20 presents a conceptualized illustration of the modes of PFOA binding to Fe/TNTs@AC. Without the iron impregnation, the adsorption of PFOA is mainly facilitated by hydrophobic interactions between the tail of PFOA and the carbon particles. As a result, the PFOA molecules are taken up with an orientation perpendicular to the surface in the head-out mode. In contrast, in the presence of the impregnated iron oxide nanoparticles, the head group is strongly adsorbed to the photoactive sites, resulting in a molecule orientation that is more conducive to the subsequent photocatalytic cleavage of the head groups and the C-F bonds.

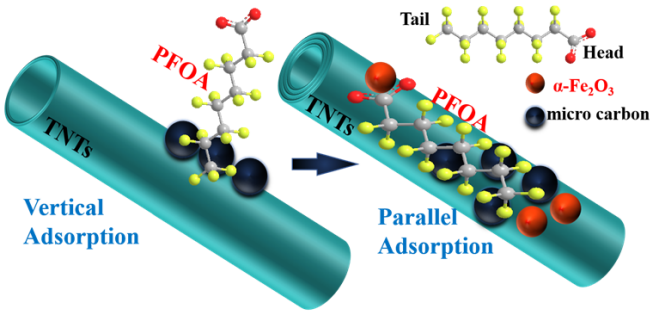

Figure 20. Conceptualized illustration of PFOA adsorption by TNTs@AC and Fe/TNTs@AC: vertical versus parallel adsorption of PFOA. Carbon nanoparticles interact with the tail, and iron oxide nanoparticles attract the head groups, setting up for subsequent photodegradation.

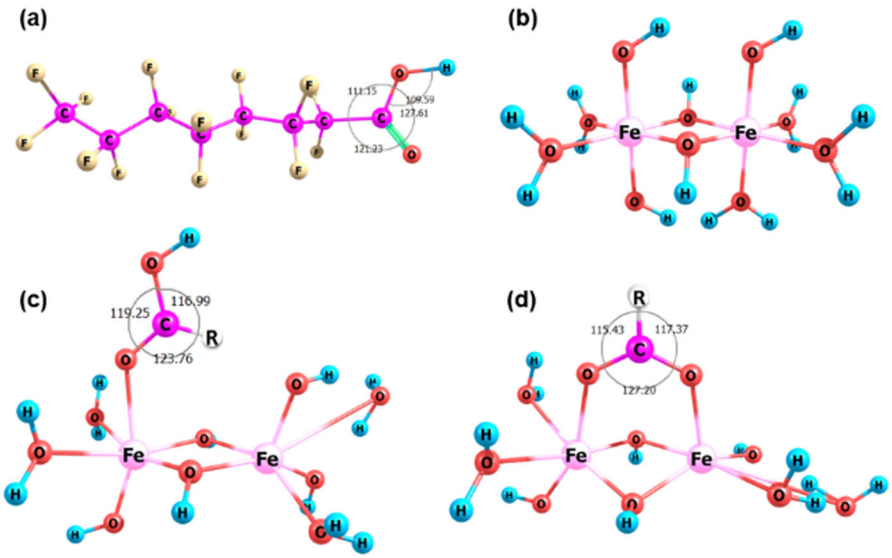

Figure 21. **(a)** PFOA, **(b)** Fe(III) dimer, **(c)** mono-dentate complexation, and **(d)** bi-dentate complexation with optimized geometries calculated at B3LYP/6−311+G(d,p) level of theory. The numbers indicate angular values between bonds.

DFT calculations were employed to analyze the orientations of adsorbed PFOA anions on Fe/TNTs@AC surface. **Figure 21** shows the resulting optimized molecular orientations with minimum energy from the frequency and optimization calculations. The angle between the hydroxyl group and carbon chain of PFOA is between 110º and 120º (**Figure 21a**). The angles remain in the same range for mono- and bi-dentate complexed PFOA (**Figures 21b** and **21c**). Based on the structural properties, PFOA adsorbed through mono-dentate complexation is likely oriented "parallel" to the Fe(III) dimer, *i.e.*, the iron oxide surface; whilst PFOA via bi-dentate complexation is "perpendicular" to the iron oxide surface in the head-in mode. However, it should be noted that the "parallel" or "perpendicular" is not mathematically strict-defined orientation, but with allowable range up to ~10º in difference. In both cases, the head-in adsorption is expected to facilitate head-first decarboxylation reactions.

4.1.6. Effects of DOM and ionic strength on PFOA photodegradation

Figure 22a shows the 2 h defluorination efficiency of PFOA by Fe/TNTs@AC in the presence or absence of humic acid (0.5 or 1 mg L^{-1} as TOC). In the absence of the HA, 2 g L^{-1} of Fe/TNTs@AC achieved 49% defluorination after 2 h of the UV irradiation. With the addition of 0.5 or 1 mg L^{-1} as TOC of humic acid, the defluorination extent was reduced to 38% or 27%, respectively. DOM may compete for adsorption sites and consume the reactive oxygen species (ROS) [Zhao et al., 2018b]. However, more detailed study is needed to identify the inhibiting species and mechanisms, and then find ways to cope with the inhibitive effect. For DoD field groundwater, such as the Willow Grove groundwater, DOM is typically less than 0.5 mg L^{-1} as TOC, and thus, which may not pose prohibitive inhibition.

While the DOM was found to inhibit the photo-defluorination/mineralization of PFOA, it is supposed to show less effect on the photodegradation of PFOA because of the lower energy demand. Yet, detailed experimental data are yet need to be acquired through follow-on studies.

Figure 22b shows effects of NaCl and $CaCl_2$ on photocatalytic defluorination of PFOA by Fe/TNTs@AC. In the absence of NaCl or $CaCl_2$, 2 g L^{-1} of Fe/TNTs@AC achieved 49% of defluorination after 2 hours of the UV irradiation. In the presence of 1 mM or 10 mM of NaCl, defluorination was reduced to 46% or 43%, respectively. The t-test results suggested that the difference in the defluorination extent at 0 or 1 mM of NaCl was insignificant (at the 0.05 level), while that at 10 mM of NaCl was significant. In the presence of 1 mM or 10 mM of $CaCl_2$, the defluorination rate was significantly decreased to 42% or 33% (at the 0.05 level), respectively. Therefore, the ionic strength effect is only significant when extremely high concentrations of salts are present.

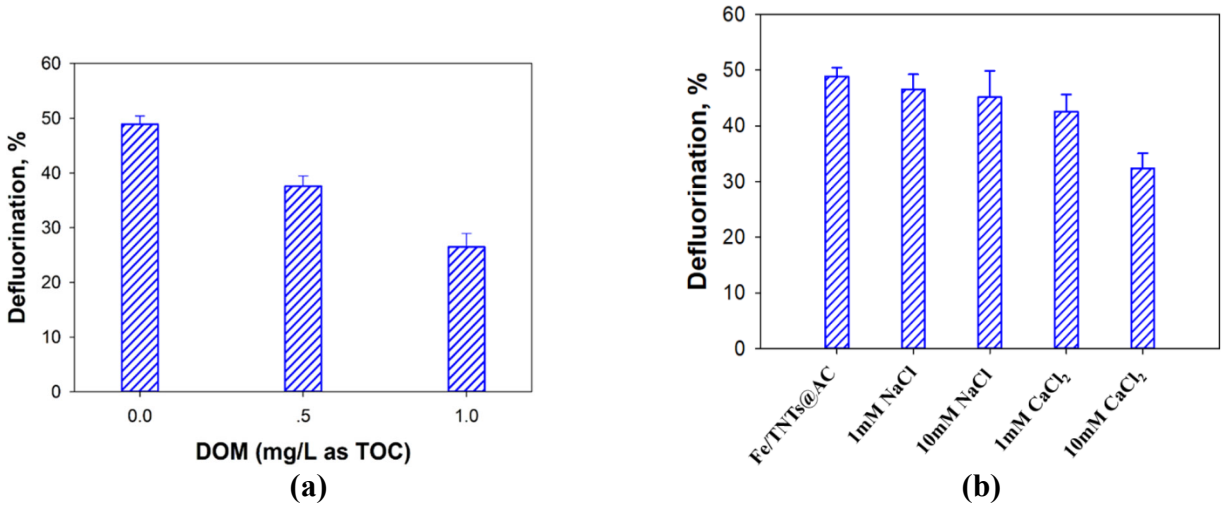

Figure 22. Effects of **(a)** dissolved organic matters (DOM) and **(b)** ionic strength (NaCl or $CaCl_2$) on PFOA photodegradation using Fe/TNTs@AC. Experimental conditions: initial [PFOA] = 100 μg L^{-1}, material dosage = 2.0 g L^{-1}, solution volume = 40 mL, pH = 7.0 ± 0.3. Leonardite humic acid = 0.5 or 1 mg L^{-1} as TOC in (a), [NaCl] = 1 or 10 mM in (b), and [$CaCl_2$] = 1 or 10 mM (c). UV (λ=254 nm, intensity = 21 mW cm^{-2}) irradiation time = 2 h.

However, more detailed experimental evidences are needed to identify the inhibiting mechanisms, especially considering that cations may enhance adsorption of PFAS, while anions tend to compete for the adsorption sites with PFAS. Moreover, while the inhibitive effect was observed for the photocatalytic mineralization of PFAS, less effect is expected for photodegradation of PFOA because of the lower energy demand, which needs to be further investigated.

Our preliminary tests also indicated that the presence of DOM (1 mg L^{-1}), NaCl (1 mM), or $CaCl_2$ (1 mM) had insignificant effect on the adsorption of PFOA by Fe/TNTs@AC, which confirms the fine selectivity of Fe/TNTs@AC towards the PFAS.

4.1.7. Effect of temperature on PFOA photodegradation by Fe/TNTs@AC

Figure 23 presents preliminary data comparing the defluorination efficiencies of PFOA after 2-h UV irradiation using Fe/TNTs@AC at room temperature (23 ± 1 ºC) and at 65 °C. At the room temperature, 2 g L^{-1} of Fe/TNTs@AC achieved 49% defluorination efficiency; at 65 ºC, the mineralization efficacy was increased to 67%, indicating mild increase in the photodegradation

temperature may remarkably increase the mineralization rate. Raising treatment temperature could be quite costly when treating large volumes of raw water. However, taking advantage of the "Concentrate-&-Destroy" strategy, this can be quite cost-effective because: 1) the photodegradation is targeting a small volume of the material, and 2) the modest temperature increase may be achieved by the light energy without significant additional energy input.

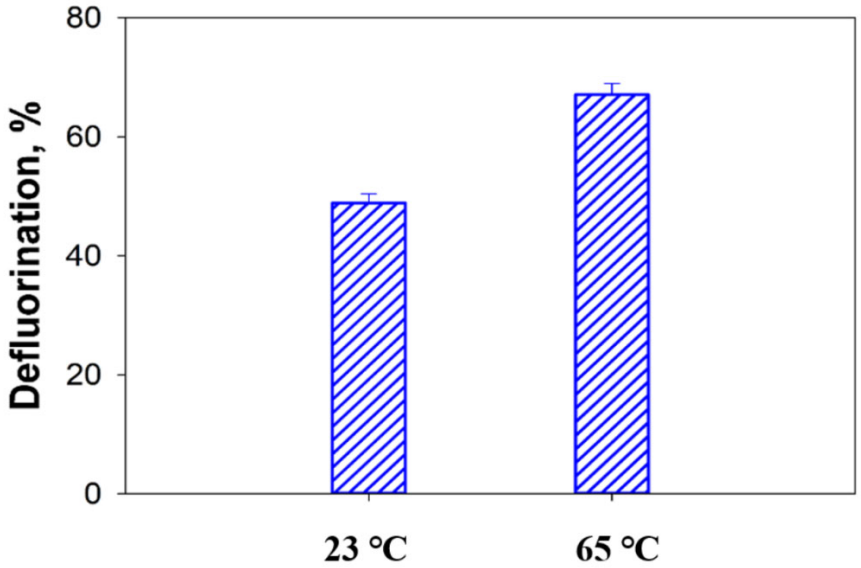

Figure 23. Effects of temperature on PFOA photodegradation using Fe/TNTs@AC. Experimental conditions: initial [PFOA] = 100 μg L^{-1}, material dosage = 2.0 g L^{-1}, solution volume = 40 mL, pH = 7.0 ± 0.3, Fan On: temperature = 22-24°C, and Fan Off: temperature = 62-65°C. UV (λ = 254 nm, intensity = mW cm^{-2}) irradiation time = 2 h.

4.1.8. Effect of material dosage on PFOA photodegradation by Fe/TNTs@AC

It is postulated that adsorption of PFAS at different material dosages will result in loading the PFAS onto different adsorption/photodegradation sites on Fe/TNTs@AC. For instance, at a lower material dosage, i.e., lower PFAS:material, PFAS are more likely to be adsorbed on the shallow or exterior sites, which are more accessible by light, and thus more photodegradable. This can be quite useful for degradation of more persistent PFAS. Although the adsorption capacity may not be fully utilized, the capital cost may not be compromised significantly due to the excellent reusability of the material, and it can be well rewarded by the gain in the additional photodegradation efficiency.

Figure 24 shows the mineralization of PFOA using Fe/TNTs@AC at various material dosages (1 – 10 μg L^{-1}). When 40, 80, 200, or 400 mg of Fe/TNTs@AC was spiked into 40 mL of 100 μg L^{-1} PFOA solution, nearly all (>99%) of PFOA was concentrated on Fe/TNTs@AC for all cases. Afterwards, the solid materials were transferred to the photo-reactor with the solution pipetted out and replaced with 10, 20, 50, and 100 mL of DI water to give an identical solid:solution ratio of 4:1 in all cases. After 2 hours of UV irradiation, Fe/TNTs@AC at the dosages of 1, 2, 5, and 10 g L^{-1} defluorinated 39%, 49%, 69%, and 48% of the PFOA, respectively. Increasing the dosage from 1 to 5 g L^{-1}, the defluorination efficiency increased with the material dosage, which can be attributed to: 1) the higher material dosage facilitated adsorption of PFOA on the easily-accessible sites, and 2) the higher photocatalyst dosage resulted in more ROS during photocatalytic process.

However, further increasing the dosage from 5 to 10 g L^{-1}, light scattering became significant because of the much large solution volume, resulting in decreased photodegradation efficiency.

Therefore, further studies are needed to optimize the dosage during the adsorption phase and the solid:liquid ratio during the photodegradation phase.

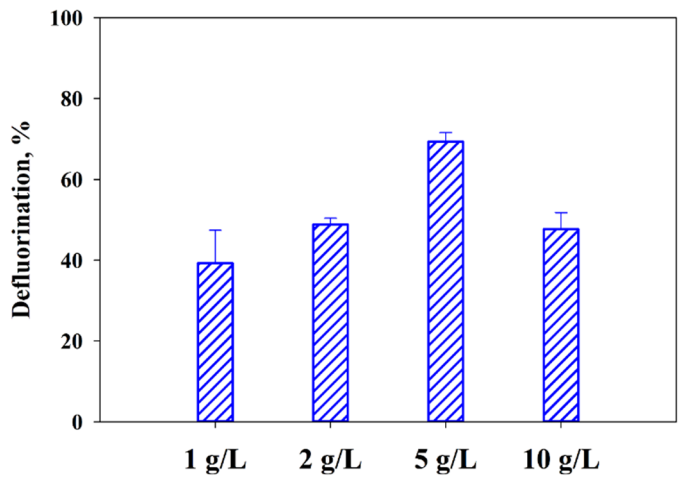

Figure 24. Effect of material dosage on the mineralization of PFOA using Fe/TNTs@AC. Experiment conditions: Material dosage = 1, 2, 5 and 10 g L^{-1}, solution volume = 40 mL, initial [PFOA] = 100 μg L^{-1}, and pH = 7.0 ± 0.3; UV (λ = 254 nm, intensity = 21 mW cm^{-2}) irradiation time = 4 h.

4.1.9. Preliminary test of PFOS removal from field groundwater using Fe/TNTs@AC

The groundwater from the Willow Grove was used to preliminarily test the photodegradation effectiveness of Fe/TNTs@AC. The total PFOS concentration in the groundwater was measured at 96.1 μg L^{-1} (linear PFOS = 57.3 μg L^{-1} and branched PFOS = 38.8 μg L^{-1}), and the PFOA concentration was measured at 1.9 μg L^{-1}. Therefore, PFOS was targeted in the adsorption and subsequent photodegradation experiments.

After 24 h of adsorption, >99% of PFOS was adsorbed on Fe/TNTs@AC, again confirming the high adsorption selectivity of the material towards the PFAS (**Figure 25**). When the spent material was subjected to the UV irradiation for 4 h, about 55% of PFOS was photodegraded (**Figure 25**). This rate is about 30% lower than that using DI water, indicating some significant matrix effect from the field water, which contained various competing ions and DOM (see **Section 3.2.6**).

Follow-on investigations are needed to identify the key inhibiting species and find ways to overcome the inhibitive effect. For instance, simple rising may desorb some adsorbed inhibitive species, some pre-treatment of the spent photocatalyst can be performed to remove the inhibiting species from the solid phase, and/or some photosensitizers may be added to enhance the photocatalytic reactions.

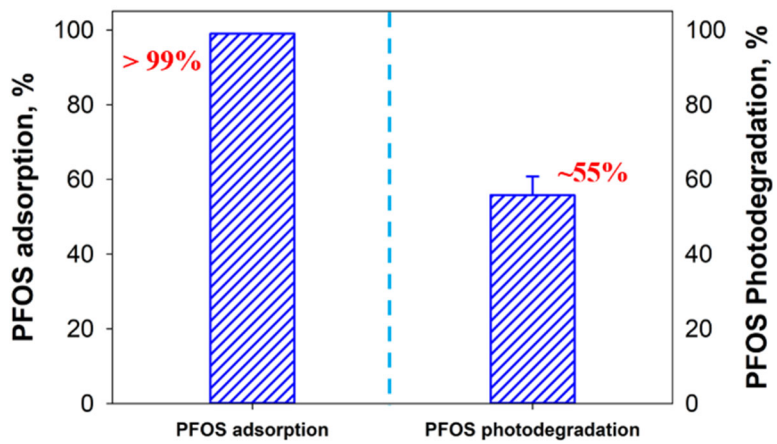

Figure 25. Adsorption and photodegradation of PFOS from the Willow Grove groundwater using Fe/TNTs@AC. Experimental conditions: initial [PFOS] = 96.1 μg L^{-1}, initial [PFOA] = 1.9 μg L^{-1}, material dosage = 2.0 g L^{-1}, groundwater volume = 40 mL, and pH = 6.3; UV (λ = 254 nm, intensity = 21 mW cm^{-2}) irradiation time = 4 h.

4.2. Results and Discussion: Ga/TNTs@AC

4.2.1. Introduction

While iron-based minerals are most desirable materials in environmental applications. The photocatalytic activity is often limited. In search for a more efficient dopant for degradation of PFAS, especially for PFOS, which is more recalcitrant, we prepared another composite adsorptive photocatalyst, Ga/TNTs@AC by impreganting gallium oxide (Ga_2O_3) on TNTs@AC. Ga_2O_3 is known to be an excellent photocatalyst with a wide band gap (~4.8 eV), and it can adsorb UV light efficiently to generate hole-electron pairs [Shao et al., 2013]. Researchers have shown that the addition of Ga could enhance the photocatalytic activity of TiO_2 towards water cleavage and organic pollution degradation [Chandiran et al., 2011; Deshpande et al., 2005]. Here, we hypothesized that Ga doping can act as an excellent electron conductor to prevent the electron-hole recombination TNTs@AC, thus facilitating the direct photocatalytic reactions between electrons/holes and PFOS molecules to achieve higher photodegradation efficiency. In this part of work, PFOS was used as the target PFAS, and preliminary batch adsorption and photodegradation of PFOS were carried out to gauge the material performances.

4.2.2. Adsorption of PFOS by Ga/TNTs@AC

Figure 26a shows the as-prepared powder Ga/TNTs@AC, whose size, shape and morphology resemble those of Fe/TNTs@AC. **Figure 26b** shows that Ga/TNTs@AC was able to rapidly and nearly completely (>99%) remove PFOS from water within 10 min. In comparison, neat AC adsorbed only 95% of PFOS after 4 h, indicating much improved adsorption performance of Ga/TNTs@AC over the parent AC. Like Fe/TNTs@AC, the fast adsorption kinetics by Ga/TNTs@AC can be attributed to: 1) the concurrent hydrophobic interactions between AC surface and PFOS tail, and 2) the concurrent electrostatic and Lewis acid-base interactions between the Ga_2O_3 nanoparticles and PFOS's head group (pH of pH_{PZC} of Ga_2O_3 = 9.0) [Wang et al., 2017].

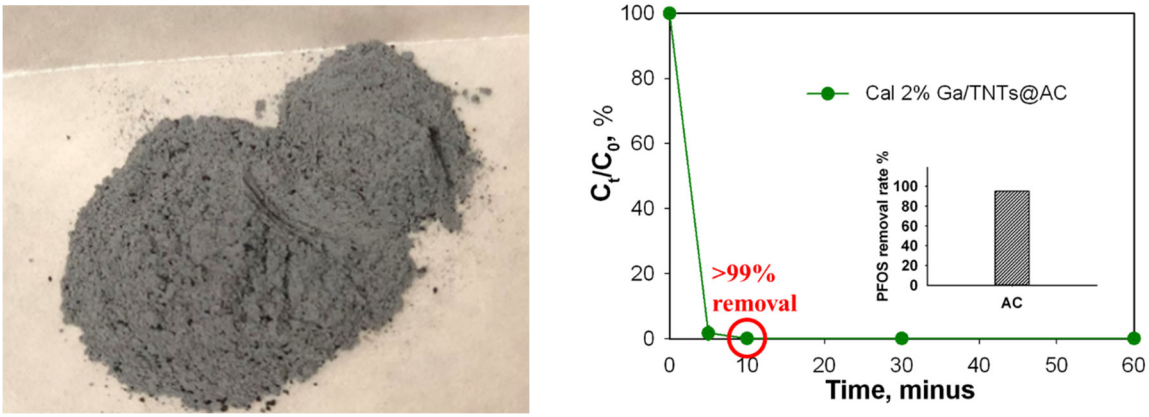

(a) **(b)**

Figure 26. **(a)** Ga/TNTs@AC prepared based on commercial AC and TiO_2 (AC:TiO_2 mass ratio = 1:1, Ga = 2 wt.% of TNTs@AC); **(b)** Adsorption kinetics of PFOS by Ga/TNTs@AC and neat AC. Experimental conditions: initial [PFOS] = 100 μg L^{-1}, Ga/TNTs@AC = 3.0 g L^{-1}, solution volume = 40 mL, and pH = 7.0 ± 0.3. C_0 and C_t: Concentration of PFOS at time 0 and t, respectively.

4.2.3. Photodegradation and defluorination kinetics of PFOS by Ga/TNTs@AC

Figure 27a shows that ~75% of PFOS was photodegraded by Ga/TNTs@AC in 4 h under the UV irradiation. Moreover, Ga/TNTs@AC was able to achieve >66% of defluorination (**Figure 27b**). In contrast, negligible PFOS (<3%) was defluoriated by neat AC after 4 h under the identical UV irradiation conditions, indicating the much enhanced photocatalytic activity of Ga/TNTs@AC. While the mechanisms for the enhanced adsorption and photocatalytic degradation of PFOS are expected to resemble those for Fe/TNTs@AC, the stronger redox potential generated by Ga_2O_3 is likely to enhance the direct hole-facilitated oxidation pathway.

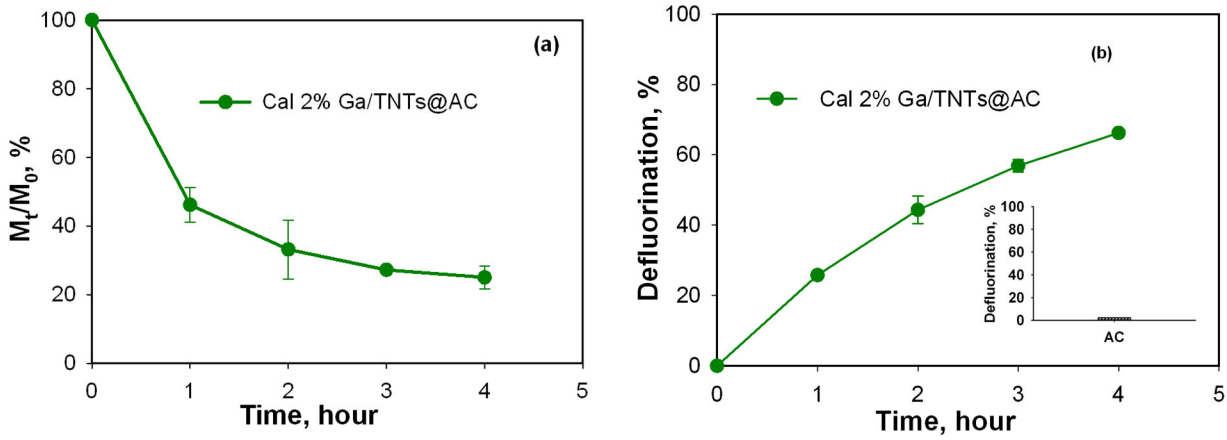

(a) **(b)**

Figure 27. Photodegradation **(a)** and defluorination **(b)** of PFOS by Ga/TNTs@AC and neat AC. Experimental conditions: initial [PFOS] = 100 μg L^{-1}, material dosage = 3 g L^{-1}, solution volume

= 40 mL, UV irradiation = 4 h, and pH = 7.0 ± 0.3; UV: λ = 254 nm, intensity = 21 mW cm^{-2}.

4.2.4. Comparison of PFOS defluorination by Fe/TNTs@AC and Ga/TNTs@AC

Figure 28 compares the defluorination effectiveness of PFOS by Fe/TNTs@AC and Ga/TNTs@AC at the same dosage of 2 g L^{-1}. After 4 h UV irradiation, Ga/TNTs@AC defluorinated 56% of the PFOS, while Fe/TNTs@AC mineralized 46%.

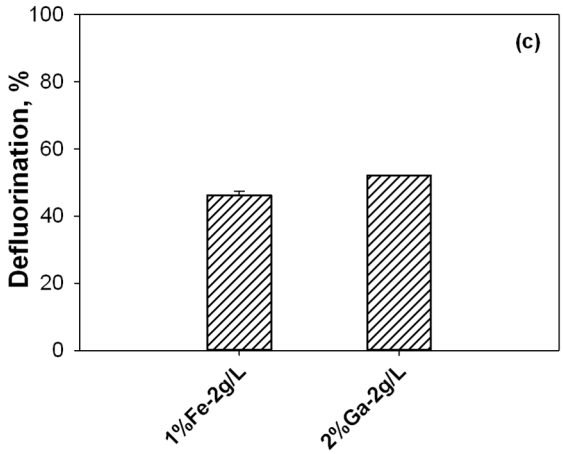

Figure 28. Defluorination of PFOS by Fe/TNTs@AC and Ga/TNTs@AC. Experimental conditions: initial [PFOS] = 100 μg L^{-1}, material dosage = 2 g L^{-1}, solution volume = 40 mL, UV irradiation and pH = 7.0 ± 0.3; UV: λ = 254 nm, intensity = 21 mW cm^{-2}. The Fe or Ga content represents the best case for the respective photocatalyst.

In addition to the greater redox potential induced by the gallium oxide, the smaller ionic radius of Ga^{3+} (0.62 Å) than that of Fe^{3+} (0.79 Å) may also play a role in the more effective photodegradation of PFOS by Ga/TNTs@AC. The difference in ionic radius between Ga^{3+} and Ti^{4+} (0.645 Å) is less than that between Fe^{3+} and Ti^{4+}. As a result, Ga^{3+} is much easier to replace Ti^{4+} ions due to their similarities in ionic radii [Ismail et al., 2018; Wojcieszak et al., 2017], resulting in more oxygen vacancies. In addition, the calcination of Ga/TNTs@AC in nitrogen atmosphere may result in increased oxygen vacancies and oxygen ionic conductivity. Therefore, Ga_2O_3 is able to absorb UV light more efficiently, generating more hole-electron pairs. Moreover, Ga_2O_3 can strongly coordinate with PFOS in the bidentate or bridging mode, which is beneficial for the photocatalytic decomposition under UV irradiation [Shao et al., 2013]. In addition, the Ga-doping eliminates the deep trap states that act as recombination centers. Further studies are needed to understand the detailed mechanisms to guide further material optimization.

4.3. Results and Discussion: FeO/CS

4.3.1. Introduction

While Fe/TNTs@AC and Ga/TNTs@AC were designed to work under UV, FeO/CS was supposed to be photoactive in the visible light region. The introduction of ferric ions in a UV (254

nm) system was found to improve the utilization of light intensity by complexing with PFOA (absorption peak around 280 nm), and consequently enhanced defluorination of PFOA [Cheng et al., 2014; Liang et al., 2016; Ohno et al., 2014]. For instance, Wang et al. [2008] found that 47.3% of initial PFOA (48 μM) was decomposed and 15.4% defluorinated within 4 h reaction time in the presence of 10 μM Fe(III) under 254 nm UV light, where the PFOA decomposition is likely initiated by electron-transfer from PFOA to Fe(III) ions, forming Fe(II) ions and an unstable organic carboxyl radical. Compared with dissolved Fe(III) ions, iron oxides show a wider light absorption, including the visible light (up to 600 nm) [Liu et al., 2019; Xu et al., 2019]. Moreover, iron oxides are able to effectively adsorb PFOA by forming inner-sphere Fe–carboxylate complexes by ligand exchange as well as electrostatic interactions [Gao and Chorover, 2012].

Ferrihydrite (Fh) is a common form of iron hydroxide minerals, which is not only 'green' and low-cost, but also has a narrow band gap energy (2.7 eV, compared to 3.2 eV for TiO_2), stretching its photoactivity into the red region of the solar spectrum. On the other hand, nanoscale carbon spheres (CS) can facilitate efficient PFAS adsorption and electron transfer as described earlier. Taking advantage of these novel properties, we prepared a new iron hydroxide-CS composite (FeO/CS), which was expected to offer decent photocatalytic activity under solar light, representing significant energy saving.

4.3.2. Characterization of FeO/CS

Figure 29 shows the material morphologies for neat CS, FeO and the FeO/CS composite prepared at an Fe:C molar ratio of 1:1, investigated by SEM and TEM/HRTEM. Neat CS appeared as nearly perfect spheres, with particle size in the range of 300-700 nm. In contrast, neat FeO displayed as clustered cubic crystals of 30-40 nm, whereas, FeO/CS(1:1) appeared as much finer and irregular agglomerated nanoparticles. The observation indicates that CS and FeO may mutually affect the final composite structure and constrain the particle growth. Besides, while the HRTEM image and fast Fourier transform (FFT) pattern of neat FeO (**Figures 29c** and **d**) show clear lattice fringes and reflections, those for FeO/CS(1:1) (**Figures 29g** and **h**) indicate poor crystallinity of the composite. Moreover, the EDS elemental mapping of FeO/CS(1:1) (**Figure 29g**) suggests that O, C, Fe are well distributed in the composite.

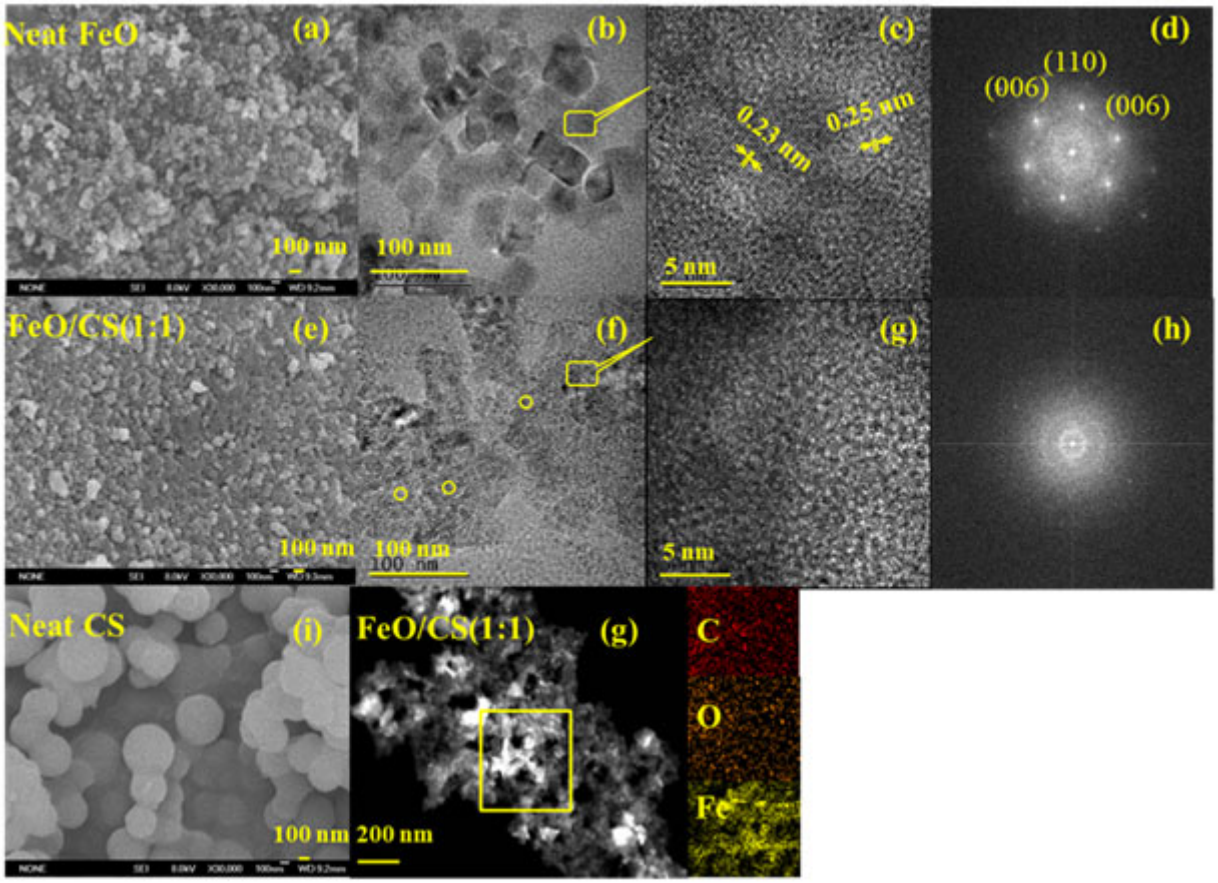

Figure 29. SEM **(a, e, i)**, TEM **(b, f)**, HRTEM **(c, g)**, FFT **(d, h)** patterns of neat FeO, FeO/CS(1:1) and neat CS; and EDS elemental mapping **(g)** of FeO/CS(1:1).

Figure 30 shows the XRD patterns of neat FeO, CS and FeO/CS prepared at various Fe/C molar ratios. No peak was evident for neat CS and FeO/CS(0.125:1), indicating that CS and FeO/CS of low Fe content are amorphous. However, at Fe/C molar ratios higher than 0.125:1, FeO/CS showed two strong peaks at 35° and 63°, and four weak peaks at 41°, 46°, 53°, and 61°, which are characteristic of ferrihydrite (Fh, JCPDS No. 29-0712), a weakly crystalline iron hydroxide. It is also noteworthy that in the absence of CS, the neat FeO conforms to the crystalline structure of hematite (Ht, JCPDS No. 33-0664), a form of well crystalline iron oxide. The XRD results indicate that the presence of CS hindered the crystallization of amorphous iron hydroxide (Fh).

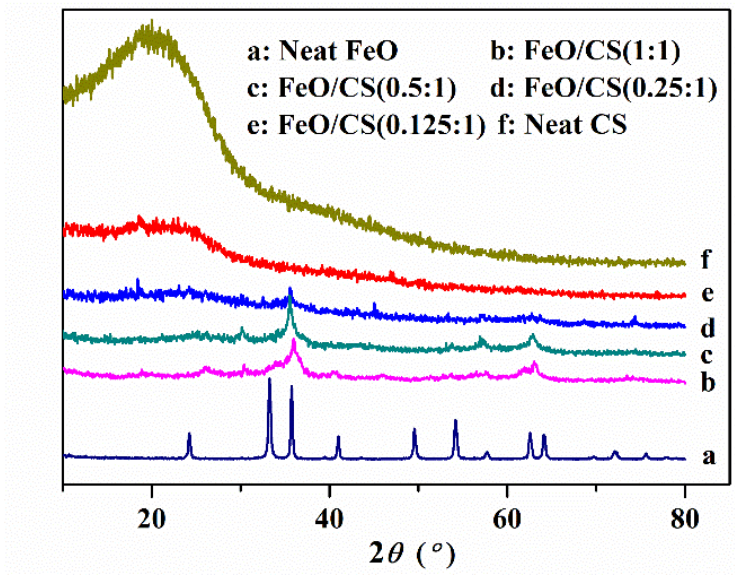

Figure 30. XRD patterns of neat CS, FeO, and FeO/CS prepared at various Fe/C molar ratios.

Figure 31 shows the FTIR spectra of the material. The strong IR bands at 564 and 472 cm^{-1} in neat FeO are characteristic signals of the Fe-O bond vibrations of α–Fe_2O_3 [Pradhan and Parida, 2011]. The peak at 1703 cm^{-1} in neat CS represents the C=O vibrations in carboxylic groups [Seredych and Bandosz, 2011]. For the FeO/CS composite, the Fe-O vibration was observed but located at 578 cm^{-1}, which is typical for the low crystalline Fh [Schwertmann et al., 1999]. The band at 1570 cm^{-1} in FeO/CS pattern represents the aromatic ring stretching mode vibrations of C=C bonds or conjugated carbonyl and carboxylate groups, and that at 1389 cm^{-1} is the symmetrical bending vibration of C-H [Thrower, 1996]. In addition, the peaks at 3443 and 3330 cm^{-1} are assigned to the O-H band, suggesting the existence of hydroxyl groups on the surface of neat FeO and FeO/CS [Thrower, 1996; Xie et al., 2011].

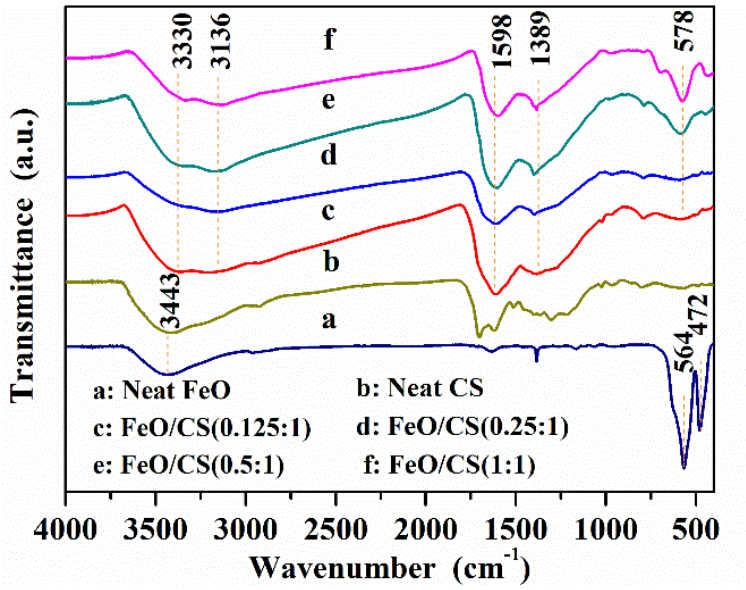

Figure 31. FTIR patterns of synthetic neat FeO, CS and FeO/CS at various Fe/C molar ratios.

Figure 32 shows the UV-vis DRS results, indicating the neat FeO shows very good absorption from UV to visible light region, while neat CS shows weakest light absorption in the region of <600 nm. In contrast, the FeO/CS composite shows not only higher absorption intensity than that of neat CS in the UV-vis light region, but also better light absorbance at >600 nm than the neat FeO. The results suggest that FeO/CS may work well as a photocatalyst throughout the UV-Vis spectra, whereas neat FeO has the potential to serve as a photocatalyst in the wavelength range of <600 nm.

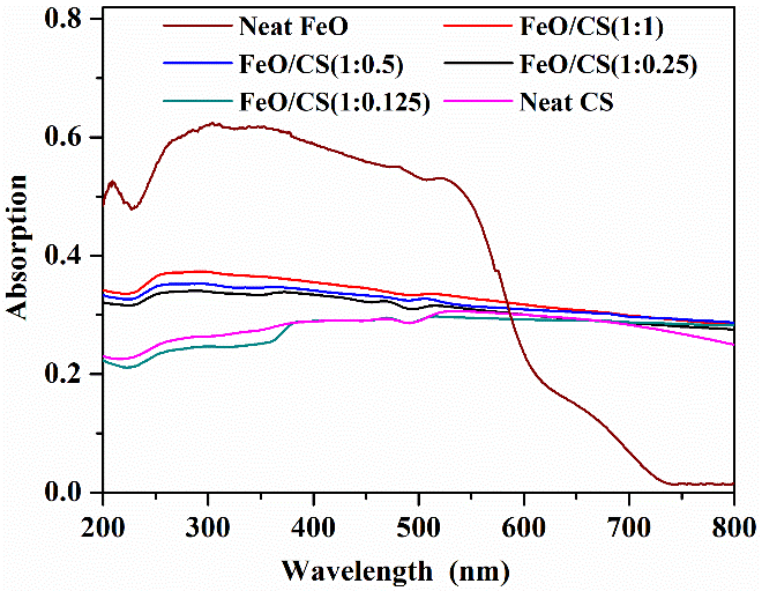

Figure 32. UV-vis DRS patterns of prepared neat FeO, CS and FeO/CS at various Fe/C molar ratios.

4.3.3. Adsorption and photodegradation of PFOA by FeO/CS

All the materials, including neat FeO, CS and FeO/CS prepared at different Fe/C molar ratios, showed high adsorption capacities towards PFOA (**Figure 33a**), and more than 99% of PFOA were adsorbed within 4 h, indicating that almost all PFOA transferred from solution to the surface of materials.

However, under solar light irradiation, the materials showed dramatically different photocatalytic activity for degradation or defluorination of the pre-adsorbed PFOA. **Figure 33a** shows that neat CS degraded only 9.4% of the PFOA, FeO degraded 61.1%, while FeO/CS(1:1) degraded >94% of PFOA. Moreover, **Figure 33b** shows that while neat CS or FeO displayed little or no F^- production after 4 h of solar light irradiation, FeO/CS(1:1) defluorinated 60% of PFOA, indicating substantial synergistic effect of the composite material.

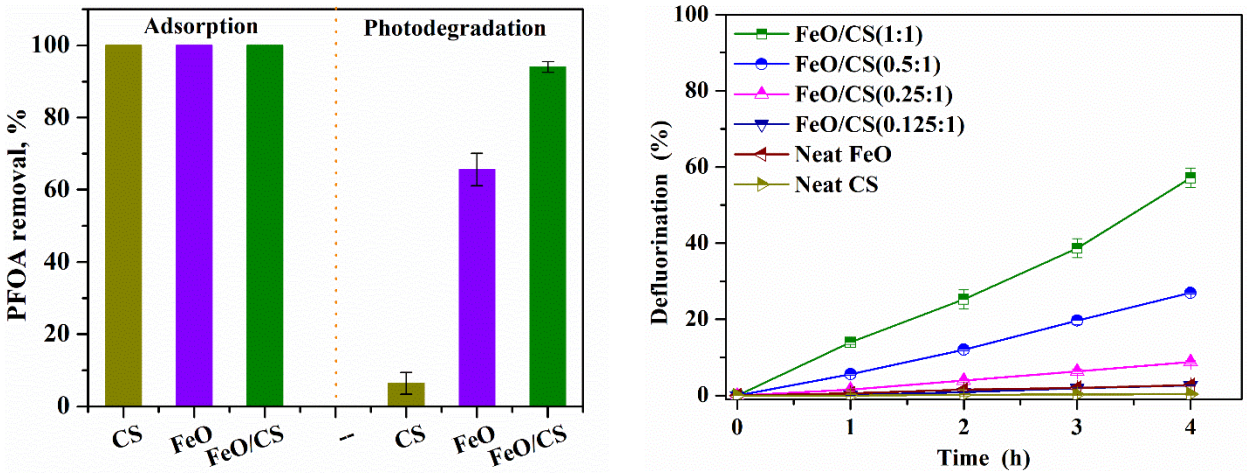

(a) **(b)**

Figure 33. Equilibrium adsorption of PFOA and subsequent photodegradation after 4 h of solar light exposure **(a)**, and defluorination kinetics **(b)** of PFOA by neat CS, FeO and FeO/CS at various Fe/C molar ratios (indicated in the brackets). Experimental conditions: initial [PFOA] = 200 μg L^{-1}, FeO/CS = 1.0 g L^{-1}, pH = 7.0 ± 0.3. Photodegradation conducted under simulated solar light (100 mW cm^{-2}).

4.3.4. Mechanisms for enhanced adsorption and photodegradation by FeO/CS

Adsorption of PFOA by FeO/CS may proceed through four mechanisms, including electrostatic attraction, hydrophobic interactions between CS and PFOA tail, π-anion interaction between the phenyl rings of the CS and PFOA, and direct coordination through ligand exchange between PFOA and iron oxide to form a Fe-PFOA complex.

The pH at the point of zero charge (PZC) values of FeO/CS, neat CS and FeO were determined to be 6.08, 1.56, and 7.90, respectively, which means both FeO/CS and neat CS are negatively charged at the experimental pH 7.0, while neat FeO is positively charged. Since PFOA is present as fully dissociated anions [Wang and Zhang, 2011], adsorption of PFOA by FeO/CS is unfavorable due to electrostatic repulsion. In addition, the water-contact angle of neat CS and FeO/CS was measured to be 25.4° and 10.0°, respectively, suggesting that both materials are rather hydrophilic due to the existence of hydrophilic groups. Hence, the hydrophobic binding between CS and PFOA is also not favored. Consequently, the π-anion interaction between CS and the CF chain of PFOA plays an important role in the adsorption of PFOS. The FTIR patterns of the reacted materials showed strong C-F vibrations in the range from 1162 to 1304 cm^{-1} [Zhang et al., 2013] for FeO/CS(1:1) and neat FeO, indicating adsorption of PFOA. However, the peaks of hydroxyl groups disappeared, implying that the PFOA was adsorbed by exchanging with the surface hydroxyl groups (**Figure 34**).

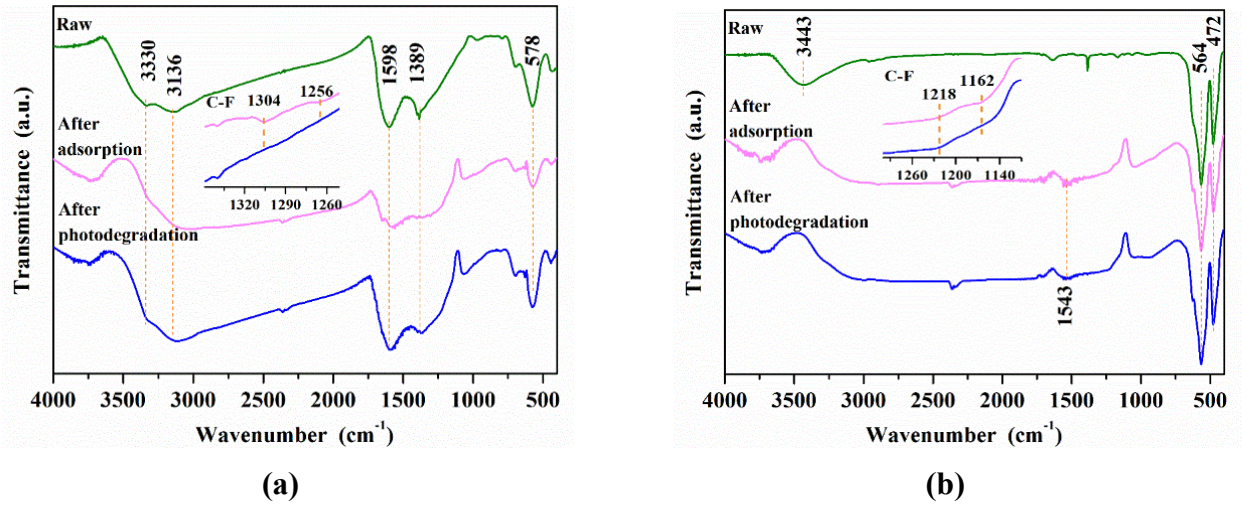

Figure 34. FTIR patterns of FeO/CS **(a)** and neat FeO **(b)** after adsorption of PFOA.

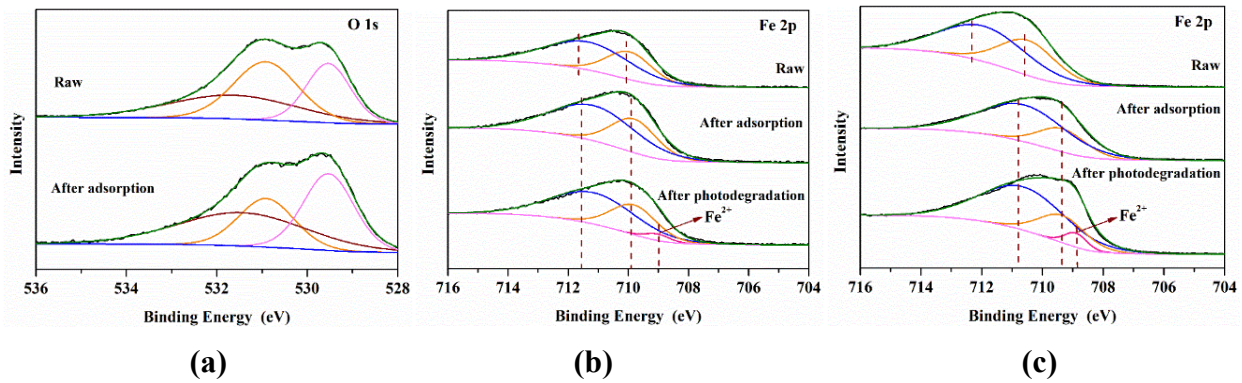

Figure 35. The O1s XPS patterns of FeO/CS **(a)**, and Fe 2p XPS patterns of FeO/CS **(b)** and neat FeO **(c)** before and after adsorption and photodegradation of PFOA.

To gain further insight into the adsorption mechanisms, the O, Fe and F elements on fresh and spent FeO/CS samples were further characterized by XPS. Referring to the O1s XPS spectra (**Figure 35a**), the three peaks with binding energies of 531.6, 530.9, and 529.5 eV are assigned to the adsorbed O (H_2O), OH groups, and structural O of FeO/CS, respectively [Casalongue et al., 2013; Sleiman et al., 2017; Xiao et al., 2016]. After adsorption of PFOA, the intensity of the OH group was decreased notably, suggesting that PFOA was adsorbed on the surface of FeO/CS by ion exchange with the OH group. The Fe 2p3/2 XPS spectra of fresh FeO/CS (**Figure 35b**) show two peaks with binding energies of 710.0 and 711.3 eV, both of which can be assigned to Fe(III) [Xu et al., 2017]. However, after adsorption of PFOA, the binding energies of Fe 2p3/2 were slightly decreased to 709.8 and 711.2 eV, respectively, suggesting formation of Fe-PFOA complexes. In contrast, for neat FeO (**Figure 35c**), the binding energies of Fe 2p3/2 decreased more than FeO/CS, from 710.5 and 711.9 eV for fresh FeO to 709.4 and 710.6 eV after PFOA adsorption. Meanwhile, the binding energies of F 1s also differed between FeO/CS and neat FeO, amounting to 689.8 and 688.3 eV, respectively [Chen et al., 2011; Gatto et al., 2015]. This phenomenon could be attributed to the different PFOA adsorption modes for FeO/CS and neat FeO. For neat CS, a weak F signal on the XPS spectra was observed at 689.2 eV after PFOA

adsorption, which is close to the position of the F signal for PFOA-laden FeO/CS, implying that CS in FeO/CS could also be a site for PFOA adsorption.

Based on the foregoing analysis, the excellent PFOA adsorption by FeO/CS is mainly attributed to the ligand exchange process between PFOA and the abundant hydroxyl groups on the material surface. In addition, the presence of CS in FeO/CS also contributes to the PFOA adsorption by interacting with the PFOA tail. Furthermore, the presence of CS weakens the C-F bond of PFOA, and lowers the energy demand for cleavage of the C-F bond [Liu et al., 2015].

After the 4 h solar irradiation, Fe(II) peaks (709.8 eV) occurred in the XPS patterns for both FeO/CS and neat FeO (**Figures 35b** and **35c**) [Xu et al., 2017]. In the photochemical system of iron oxide and PFOA, Fe(II) can be generated through solar light induced reduction of Fe(III) and electron transferring from PFOA to Fe(III) [Voelker et al., 1997; Wang et al., 2008]. However, for FeO/CS without PFOA, no Fe(II) signal was observed (**Figure 36**), confirming that Fe(III) was reduced into Fe(II) mainly by electrons from PFOA.

In addition, no obvious F signal in the XPS pattern of FeO/CS after the solar light irradiation **(Figure 37).** However, a strong F peak remained in the XPS pattern of neat FeO, indicating the much greater photoactivity of FeO/CS over neat FeO. This observation is backed by the FTIR patterns in **Figure 34**, which shows that the peaks of C-F vibrations of FeO/CS(1:1) disappeared after 4 h solar light irradiation, those for the neat FeO remained.

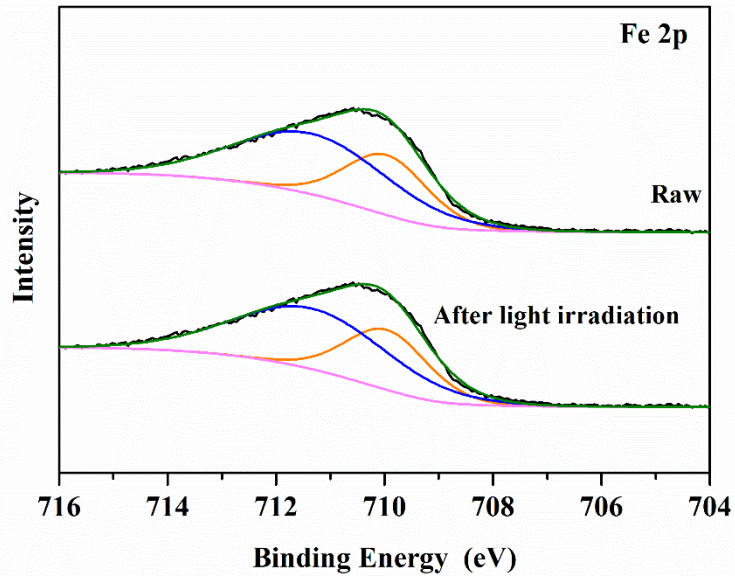

Figure 36. The Fe 2p XPS spectra of fresh and solar light irradiated FeO/CS(1:1) in the absence of PFOA.

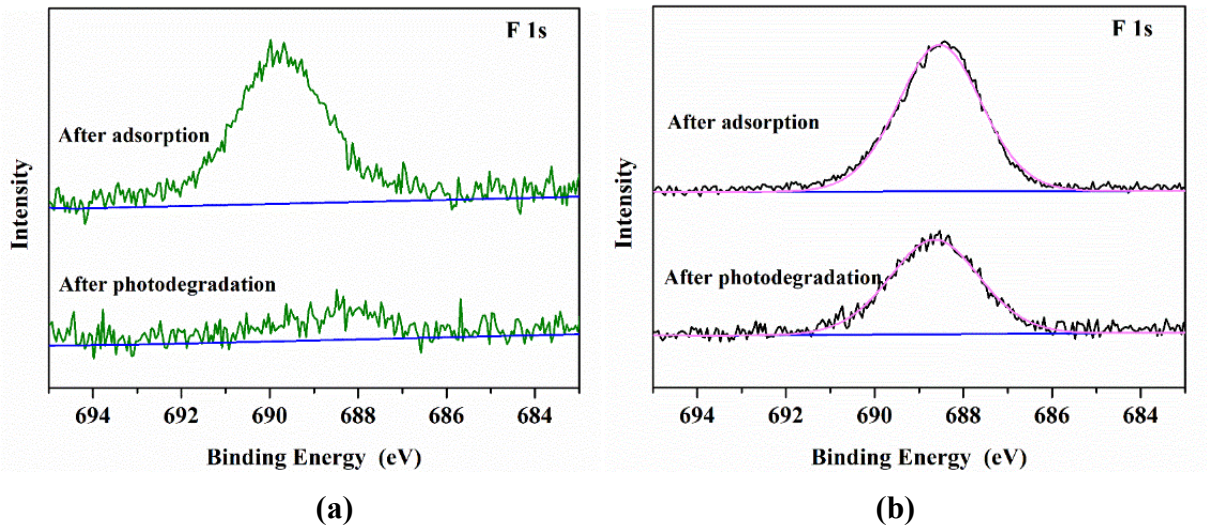

Figure 37. F1 s XPS patterns of FeO/CS **(a)** and Fe_2O_3 **(b)** before and after adsorption or photodegradation of PFOA.

The XPS results in **Figure 37** also indicates Fe(II) was formed on the surface of both FeO/CS(1:1) and neat FeO after photodegradation. However, PFOA degradation and defluorination showed a huge difference in two systems. To acquire deeper insight into the reaction mechanisms, DFT calculations were performed to analyze the electron transfer process involved in PFOA degradation by FeO/CS and neat FeO. According to XRD results, the iron oxide in FeO/CS and neat FeO was in the form of Fh and Ht, respectively. Hence, Fh and Ht were used as the model iron oxides for Fh/CS(1:1) and neat FeO, respectively. The DFT calculations of PFOA adsorption on Fh and Ht used in this study were focused primarily on the (001) surface, which is the common exposed face for iron (hydro)oxides [Kerisit et al., 2015; Noerpel et al., 2016].

Figure 38 shows the optimized PFOA-Ht (001) and PFOA-Fh (001) results based on the DFT calculations. As expected, Fh shows more suitable Fe-O bond lengths for PFOA adsorption, and the distance of adjacent Fe atom in Fh is 2.936 Å, which is shorter than that in Ht (4.758 Å). The interatomic distance measurements suggested that two oxygen atoms from –COOH of PFOA chelate to the Fe of Fh ($d_{O–Fe}$ = 1.955 and 2.160 Å, respectively) in a binuclear bidentate mode (**Figures 29b** and **c**); in contrast, only one oxygen atom from –COOH of PFOA chelates to the Fe of Ht ($d_{O–Fe}$ = 1.999 Å). The relative adsorption energy produced for PFOA-Fh and PFOA-Ht was -1.81 and -1.28 eV, respectively. This result suggests that adsorption of PFOA by both forms of iron oxide is spontaneous and thermodynamically stable [Xu et al., 2012], though PFOA adsorption by Fh is more favorable than by Ht.

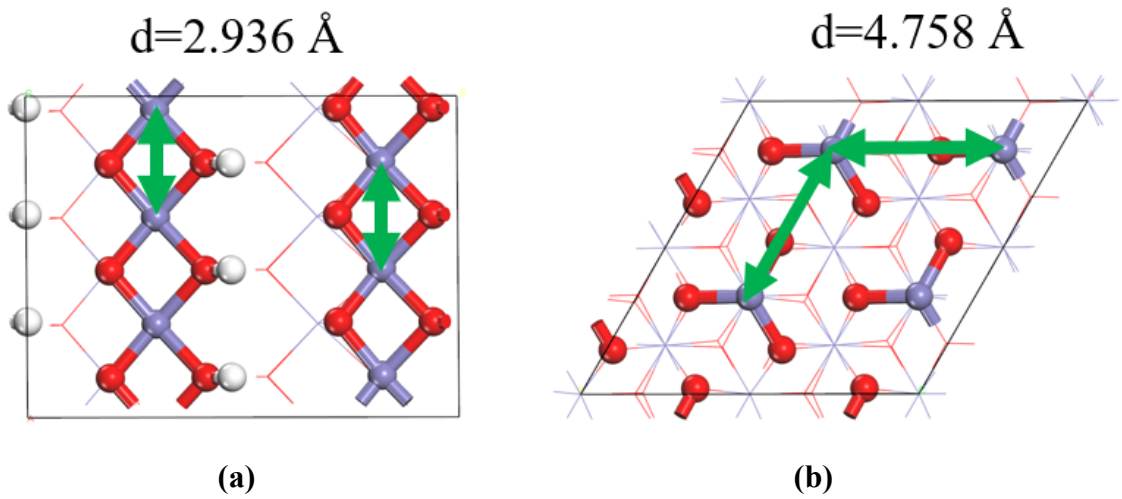

Figure 38. Calculated iron atom structures of ferrihydrite **(a)** and hematite **(b)**. Blue: Fe; Red: O; Light grey: H.

Furthermore, we hypothesized that the different PFOA adsorption structures for Fh and Ht may result in different electron transfer processes. To test this hypothesis, the density of states (DOS) was calculated to analyze the electron interactions between the iron oxide surfaces and PFOA. As shown in **Figure 39**, upon PFOA adsorption, the iron oxide surfaces are spin-paired with the asymmetric majority states of Fe atoms and the minority states of O atoms, which is attributed to the binding of Fe atoms on the surface of the iron oxides with PFOA. **Figure 40** shows the molecular orbitals and electron distributions of PFOA, where the highest occupied molecule orbital (HOMO) and the lowest un-occupied molecular orbital (LUMO) are found in the oxygen p orbitals and the carbon p orbitals, respectively. **Figure 40** also reveals that the most electron-deficiency or electron-enrichment (i.e., the most charge density difference) is found at the carboxyl head group of PFOA, which is prone to acting as an adsorption site and/or to transferring electrons to the photocatalysts.

Figure 41 compares energy levels of the HOMO and LUMO of PFOA adsorbed on Fh and Ht with energy levels of VB and CB of Fh and Ht. The smaller energy gap between the HOMO and VB or LUMO and CB for Fh results in more favorable electron transfer from PFOA to Fh than Ht, accounting for the observed higher photocatalytic activity of Fh over Ht [Zhao et al., 2013].

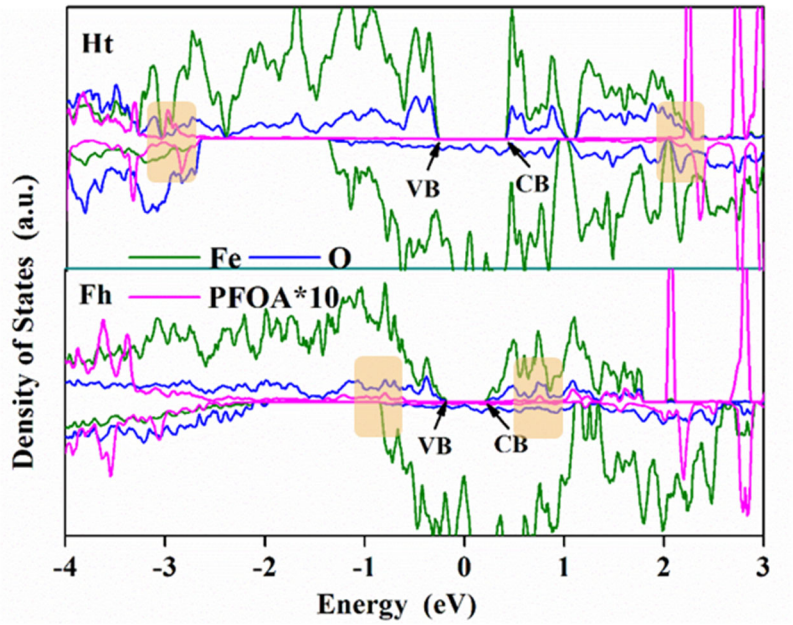

Figure 39. The density of states of PFOA-loaded hematite and ferrihydrite. For clarity, the local contributions have been scaled up by a factor of 10.

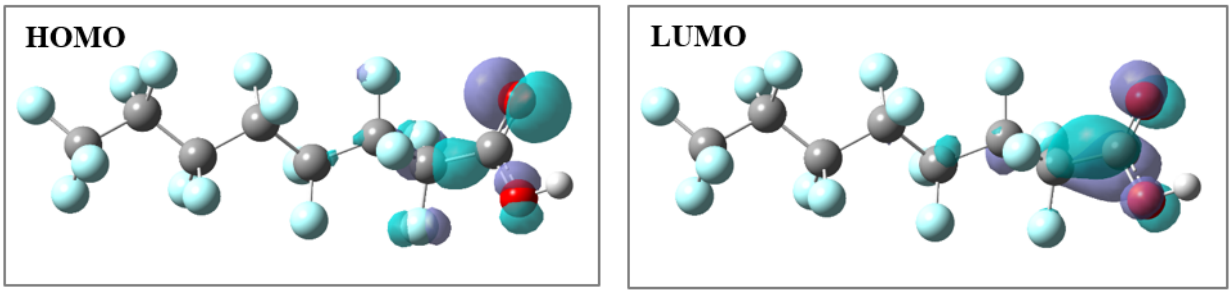

Figure 40. Molecular orbitals and electron distributions of PFOA. Green: negative phase; Purple: positive phase; Light blue: F; Dark grey: C; Red: O; and light grey: H; HOMO: the highest occupied molecule orbital; and LUMO: the lowest un-occupied molecular orbital.

	eV	
Fh	VB: -0.20	CB: 0.20
Adsorbed PFOA on Fh	HOMO: -0.75	LOMO: 0.80
Ht	VB: -0.25	CB: 0.42
Adsorbed PFOA on Ht	HOMO: -2.60	LOMO: 2.20

Less difference: Conducive to e transfer

More difference: Less favorable to e transfer

Figure 41. Comparing energy levels of the highest occupied molecule orbital (HOMO) and the lowest un-occupied molecular orbital (LUMO) of PFOA adsorbed on Fh and Ht with energy levels of valence band (VB) and conduction band (CB). The smaller band gap between the respective HOMO and VB or LUMO and CB is more conducive to electron transfer from PFOA to the photocatalysts.

The charge density difference in conjunction with the Bader charge were further studied to trace down the electron transfer behaviors. The exchange and transfer of electrons take place between the surface Fe atoms and –COOH of PFOA molecules (**Figure 42**). Under solar light irradiation, the adsorbed PFOA on the Fh surface obtains excess electrons. These electrons are delocalized around the neighboring Fe atoms, and accumulated mainly at the nearest Fe atoms or those bonded with the PFOA. According to the calculated electron transfer in the Bader charge, about 0.47 e could transfer from PFOA to Fe atoms on the surface of Fh, while only 0.35 e to Fe atoms on the surface of Ht.

These theoretical calculations elucidate the molecular level mechanisms for the greater photocatalytic degradation of PFOA by Fh in FeO/CS than by Ht in the neat iron oxide.

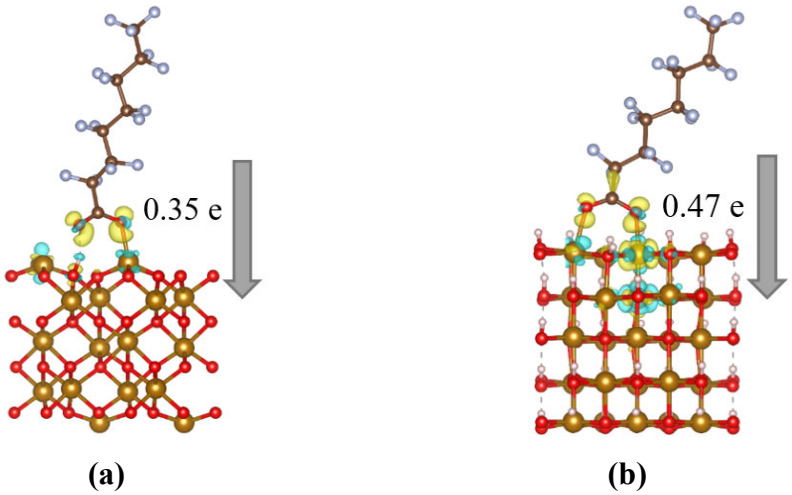

Figure 42. **(a)** The charge density difference of PFOA-laden hematite; and **(c)** The charge density difference of PFOA-laden ferrihydrite. The yellow and blue iso-surfaces represent charge accumulation and depletion in the space, respectively.

4.3.5. Role of hydroxyl radical in PFOA photodegradation by FeO/CS

Researches have had the notion that $^{\bullet}$OH is ineffective for directly attacking PFOA or PFOS. However, recent works on PFOA degradation in the photo-Fenton or homogenous Fe(III)-catalyzed photolysis systems, electrochemical systems, and persulfate mechanochemical systems, $^{\bullet}$OH is deemed to contribute to PFOA degradation.

Radical capture experiments and electron paramagnetic resonance (EPR) analysis were carried out to understand the role of $^{\bullet}$OH in the PFOA photocatalytic degradation process. **Figure 43** compares the PFOA photodegradation extents after 4 h of the solar irradiation in the presence or absence of isopropyl alcohol (ISA), a known $^{\bullet}$OH scavenger. The presence of ISA decreased the PFOA degradation from 94% to 22%. In addition, the scavenger almost ceased defluorination of PFOA (not shown). The results indicate that $^{\bullet}$OH played an important role in the PFOA decomposition by FeO/CS.

Figure 44. Electron paramagnetic resonance (EPR) spectra of DMPO–$^{\bullet}$OH adducts produced by FeO/CS(1:1) under air or argon conditions. When exposed to air, a weak $^{\bullet}$OH signal (four-line with an intensity ratio of nearly 1:2:2:1) was observed in the system of FeO/CS(1:1) without PFOA. However, when PFOA was added in the system, a much stronger $^{\bullet}$OH signal occurred,

indicating that the presence of PFOA enhanced ˙OH generation under the atmospheric condition. In contrast, under the argon condition, both systems showed a weak ˙OH signal, indicating that O_2 is critical for ˙OH generation. In the FeO/CS system, there are two possible pathways to generate ˙OH: 1) direct photolysis of Fe(III), and 2) reaction between Fe(II) and dissolved O_2 through a sequential molecular oxygen activation pathway. Based on the EPR data, the Fe(II) induced molecular oxygen activation is the main pathway of ˙OH generation.

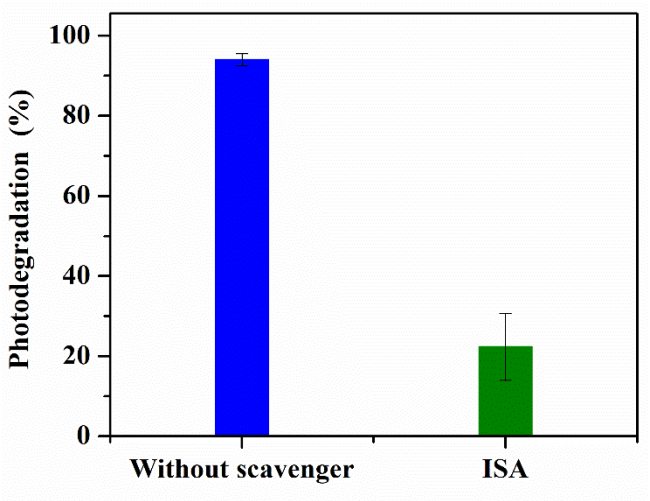

Figure 43. PFOA removal rate in the FeO/CS with or without isopropyl alcohol (ISA). Experimental conditions: dosage = 1.0 g L^{-1}, initial PFOA = 200 μg L^{-1}, pH = 7.0 ± 0.1, reaction time = 4 h, initial ISA = 10 mM.

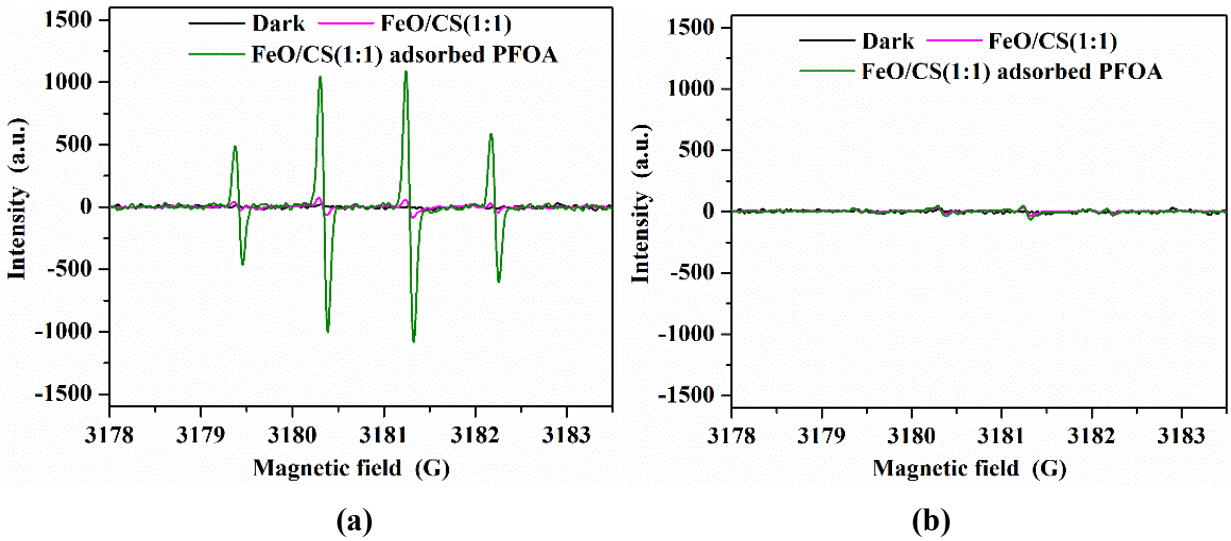

Figure 44. Electron paramagnetic resonance (EPR) spectra of DMPO–•OH adducts produced by FeO/CS(1:1) under air **(a)** or Ar **(b)** after solar light irradiation for 20 min.

As was the case in the photodegradation of PFOA by Fe/TNTs@AC (**Section 4.1.5**), following the head decarboxylation, the resulting C_7F_{15}˙ is believed to further decompose the perfluorinated alcohol ($C_7F_{15}OH$) by reacting with ˙OH or H_2O, and then undergo further decarboxylation and

defluorination. Here, DFT calculations were performed to investigate the reactions between $C_7F_{15}^{\bullet}$ and $^{\bullet}OH$ or H_2O, where the corresponding frontier molecular orbitals (HOMO and LUMO), change of Gibbs free energy at 298.15 K, and the reaction enthalpy were calculated.

As presented in **Figure 45**, the HOMO of the $C_7F_{15}^{\bullet}$ when combined with $^{\bullet}OH$ was found lower than that combined with H_2O. The narrower energy gap between HOMO–LUMO, the smaller energy required for excitation according to the frontier molecular orbital theory. Moreover, the production of perfluorinated alcohol ($C_7F_{15}OH$) initiated by $^{\bullet}OH$ exhibited a thermodynamic barrier of 268.1 KJ/mol, which is much lower than that triggered by H_2O (613.2 KJ/mol). Meanwhile, the reaction of $C_7F_{15}^{\bullet}$ with H_2O showed a reaction enthalpy change of 580.3 KJ/mol, which is much higher than that (221.2 KJ/mol) of $^{\bullet}OH$ mediated reaction. These results suggest that $C_7F_{15}^{\bullet}$ is more prone to reacting with $^{\bullet}OH$ than H_2O from the perspective of thermodynamic driving force under the solar light irradiation.

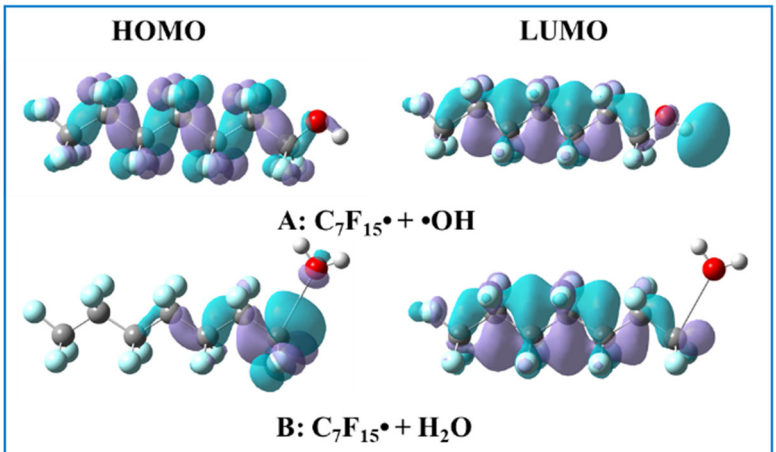

$C_7F_{15}OH$ production pathway	ΔGibbs free energy (KJ/mol)	ΔEnthalpy (KJ/mol)
A	268.1	221.2
B	613.2	580.3

Figure 45. The iso-surface plots of frontier orbitals of $C_7F_{15}^{\bullet}$ when combined with $^{\bullet}OH$ or H_2O, change in Gibbs free energy and calculated reaction enthalpy change for $C_7F_{15}OH$ production induced by $^{\bullet}OH$ or H_2O possible pathway of PFOA degradation.

4.3.6. Intermediate products and reaction pathway in PFOA photodegradation by FeO/CS

Figure 46 shows mass chromatograms for various organic by-products formed after 4 h of the photochemical decomposition of PFOA in the FeO/CS(1:1) and neat FeO systems obtained using the LC-QTOF-MS system. Six shorter-chain (C_2–C_7) perfluorinated carboxylic acids were identified according to the mass spectra and retention times in both systems, including $C_6F_{13}COOH$ (PFHpA), $C_5F_{11}COOH$ (PFHxA), C_4F_9COOH (PFPeA), C_3F_7COOH (PFBA), C_2F_5COOH (PFPrA), and CF_3COOH (TFA). The degradation intermediates are similar to those in the Fe/TNTs@AC and those reported in the literature for other iron-based photocatalytic processes. However, no peak of PFOA disappeared in the FeO/CS(1:1) system, while it remained in neat FeO system. In addition, the peak intensity of intermediates in the FeO/CS(1:1) system was

generally higher than that in the neat FeO system, which confirmed that FeO/CS(1:1) offers much greater photodegradation activity for PFOA than the neat FeO.

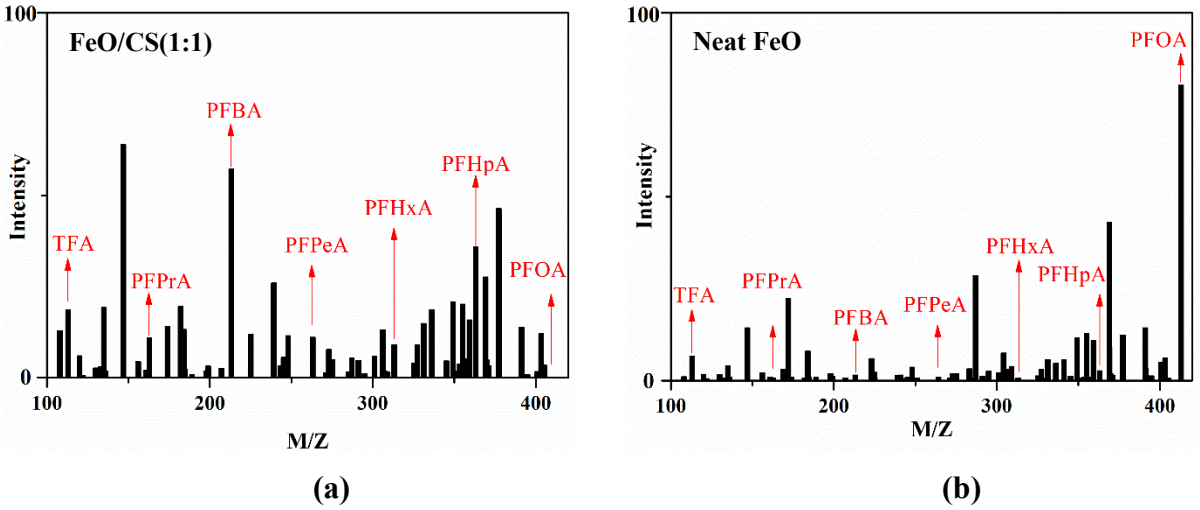

Figure 46. ESI/MS spectra of the ion peaks assigned as by-products of PFOA photodegradation by FeO/CS(1:1) **(a)** and neat FeO **(b)** after 4 h of simulated solar light irradiation. Experimental conditions: material dosage = 1.0 g L^{-1}, initial [PFOA] = 200 μg L^{-1}, pH = 7.0 ± 0.1, reaction time = 4 h. The negative-ion mode was used and the scan range was 100-410.

Based on the reaction by-products and theoretical calculations, the possible pathway of PFOA photodegradation in the FeO/CS system is proposed (**Figure 47**). First, PFOA is adsorbed with both head and tail attached on the surface of FeO/CS, where the head is adsorbed in the binuclear bidentate mode. Under solar light irradiation, the photo-excited electrons transfer from PFOA to Fe(III) to yield Fe(II) and the unstable organic free radical ($C_7F_{15}COO^{\bullet}$), which undergoes the Kolbe decarboxylation reaction to form $C_7F_{15}^{\bullet}$. On the other hand, the resulting Fe(II) ions activate molecular oxygen to produce $^{\bullet}OH$ radicals, which react with $C_7F_{15}\bullet$ to form $C_7F_{15}OH$. The perfluorinated alcohol is rather unstable and undergoes defluorination with one fluorine converted into fluoride and generation of $C_6F_{13}COF$, which further decomposes into the shorter chain $C_6F_{13}COOH$ with the cleavage of another fluorine. Then, the shorter-chain by-product may undergo the same cycle, each eliminating one CF_2 unit.

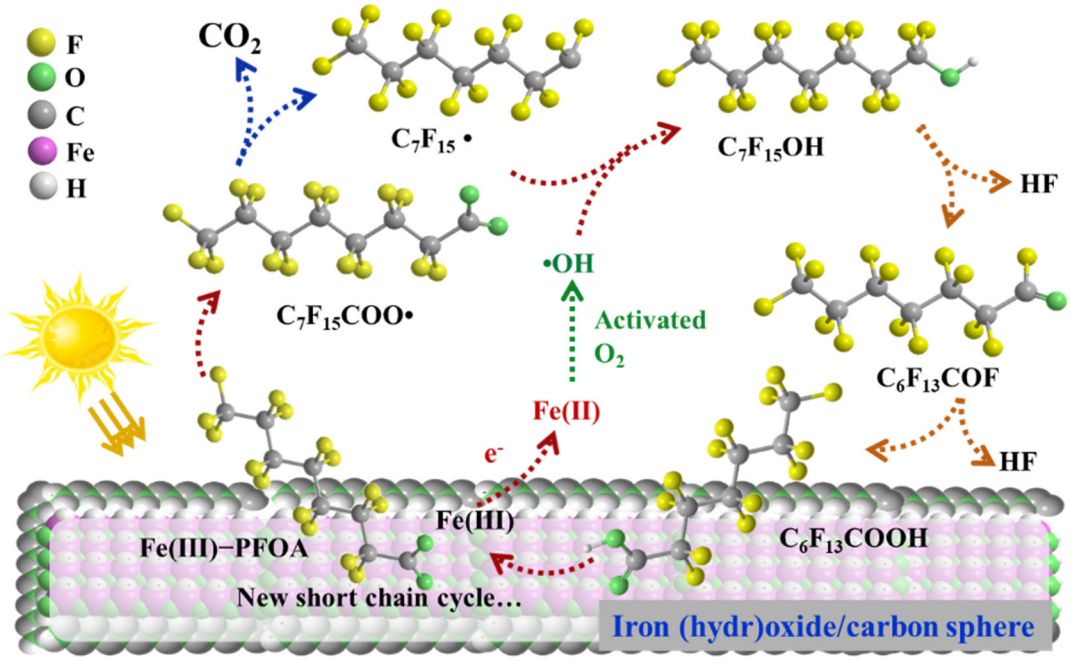

Figure 47. Proposed pathway for photocatalytic degradation of PFOA by FeO/CS.

4.4. Results and Discussion: Soil Treatment

4.4.1. Extraction of PFAS from the Willow Grove field soil

Table 4 summarizes the PFOA and PFOS concentrations detected in the field soil. PFOS was found to be the main PFAS in the field soil, with a concentration of 1507.7 ± 37.6 ng g^{-1}. Likewise, PFOA was also detected but with a much lower concentration (21.4 ± 6.8 ng g^{-1}). The extraction results indicate that PFOS should be the major concern at this DoD site, which is consistent with the past usage and the fact that PFOS is more persistent in the environment than PFOA.

Table 4. Concentrations of PFOA and PFOS in the soil of the Willow Grove site.

Compounds	Concentration (ng g^{-1})	SD
PFOS	1507.7	37.6
PFOA	21.4	6.8

4.4.2. Batch desorption and successive desorption of PFOS from Willow Grove soil

Figure 48 compares the equilibrium desorption extents of PFOS using the following desorbing reagents: Corexit EC9500A at 50, 180, 300 and 500 mg L^{-1}, SPC1000 at 50, 180, 300, and 500 mg L^{-1}, Dispersant with 1 wt.% NaCl, and DI water. All the dispersant concentrations are higher than the respective critical micelle concentrations (CMC), e.g., the apparent CMC value for Corexit EC9500A was reported to be 22.5 mg L^{-1} [Gong et al., 2014]. Generally, the PFOS desorption efficiency followed the order of: Corexit EC9500 > Corexit EC9500 + 1% NaCl > DI water > SPC1000 > SPC1000 + 1% NaCl. While Corexit EC9500 was able to effectively desorb PFOS

from the field soil, SPC1000 actually inhibited the desorption process. The inhibitive effect of SPC1000 is attributed to the dual-mode and concentration-dependent effects of surfactants, namely, surfactants may partition between the soil and the aqueous phase and the adsorbed surfactants may increase the adsorption of hydrophobic compounds via adsolubilization [Gong et al., 2014]. It is also noteworthy that the presence of 1 wt.% NaCl inhibited PFOS desorption in both dispersant systems. Like surfactants, NaCl may have some contrasting effects on the sorption or desorption of PFOS. On the one hand, Cl^- anions may help elute PFOS due to competitive adsorption for the anion exchange sites on the soil, on the other hand, Na^+ cations can enhance PFOS uptake by suppressing the negative soil surface potential.

At a dosage of 50 mg L^{-1}, Corexit EC9500 was able to partition ~64% of soil-sorbed PFOS into the solution phase. Increasing the dispersant concentration from 50 mg L^{-1} to 300 mg L^{-1} increased the PFOS desorption extent to 77%, indicating the low concentrations of the dispersant can effectively desorb PFOS from soil. To our knowledge, this is the first study of the type.

It should be noted that the desorption was not exhaustive because of the limitation of the batch system, where desorbed PFOS remained in the aqueous phase, preventing further desorption. When the tests were carried out in the successive desorption mode (i.e., replacing the eluent with fresh dispersant solution after each batch), >90% of PFOS was desorbed at a dispersant concentration of 300 mg L^{-1} (**Figure 49**). The desorption reached equilibrium in 1 h for every run and the amount of PFOS desorbed in three runs were 75%, 12%, and 3.5%, respectively. From a soil remediation viewpoint, the residual (~10%) PFOS is hardly bioavailable, and thus, the dispersant washing may meet the treatment goal. In practice, the soil washing can be conducted either in situ by sprinkling the dispersant solution through the soil bed or through a column/tank flushing configuration. As such, more efficient PFOS elution can be achieved using much lower dispersant concentration than in the batch experiments.

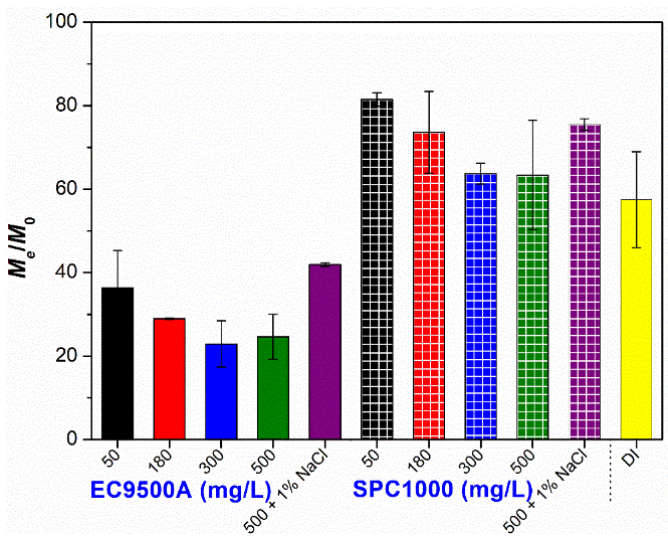

Figure 48. Batch equilibrium desorption of PFOS from the Willow Grove Soil using two common oil dispersants (Corexit EC9500A and SPC1000) at various concentrations and with or without NaCl. Experimental conditions: soil mass = 2 g, solution volume = 40 mL, pH = 7 ± 0.2, temperature = 22 ± 1 ºC, equilibrium time = 24 h. Error bars refer to standard deviation of triplicates. (M_e is the mass of PFOS remaining in soil at equilibrium, and M_0 is the initial mass).

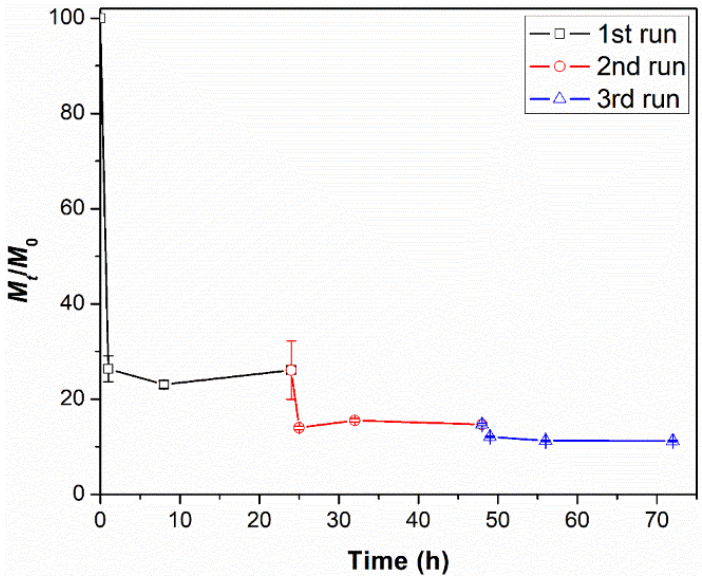

Figure 49. Successive desorption of PFOS from the Willow Grove soil using Corexit EC9500A dispersant solution. Experimental conditions: mass of soil = 2 g, solution volume = 40 mL, dispersant concentration = 300 mg L^{-1}, pH = 7 ± 0.2, temperature = 22 ± 1 ºC. (M_t is the mass of PFOS remaining at time t, and M_0 is the initial mass).

Typically, oil dispersants are mixtures of anionic and nonionic surfactants and solvents. Oil dispersants are able to lower the oil-water interfacial tension, thereby breaking surface oil slicks into fine droplets and facilitating dispersion and dissolution of hydrophobic compounds into the water column [Gong et al., 2014]. Corexit EC9500A contains two nonionic surfactants (48%) and an anionic surfactant (35%) in an aqueous hydrocarbon solvent (17%) [Gong et al., 2014]. **Table 5** shows salient surfactant compositions of the dispersant. Corexit EC9500A has been listed as an EPA-approved dispersant and have been most widely used in coping will oil spills, and low concentrations of the dispersant is believed to show minimal adverse environmental effects.

Compared to other soil washing agents, especially organic solvents such as methanol, Corexit EC9500A is not only much more cost-effective, but also much "greener".

Table 5. Characteristics of surfactant compositions in the oil dispersant Corexit EC9500A.

Surfactants	Ionic property	Molecular formula	Molecular weight (g/mol)	Critical micelle concentration (CMC) (mg L^{-1})	Chemical structure
Polyoxyethylene (20) sorbitan monooleate (Tween 80)	Neutral	$C_{64}H_{124}O_{26}$	1310	14 (Yeom et al., 1995)	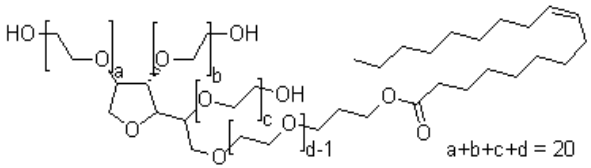
Polyoxyethylene(20) sorbitan trioleate (Tween 85)	Neutral	$C_{60}H_{108}O_8 \cdot (C_2H_4O)_n$		23 (Wan and Lee, 1974)	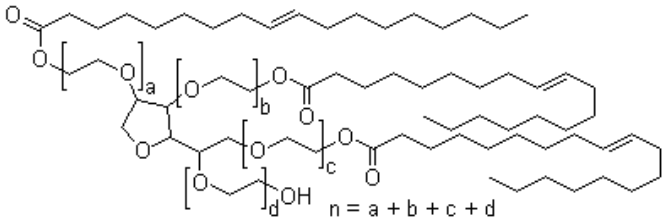
Sodium dioctyl sulfosuccinate (SDSS)	Anionic	$C_{20}H_{37}NaO_7S$	444.56	578 (Yehia, 1992)	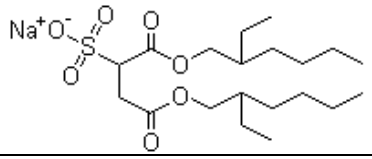

4.4.3. Re-adsorption of desorbed PFOS by Ga/TNTs@AC

Figure 50 shows re-adsorption kinetics of PFOS from the spent dispersant using Ga/TNTs@AC (Ga = 2 wt.%). Although the desorption rate appeared slower compared to that in the DI water system, >98% of PFOS was reloaded on the photocatalyst within 4 h of contact time. Further increasing the material dosage to 10 g L^{-1} resulted in faster and complete removal of PFOS from the spent dispersant solution. The highly effective adsorption enables the PFOS to be photodegraded subsequently through the same "Concentrate-&-Destroy" strategy, and allows for reuse of the treated dispersant solution in another cycle of desorption.

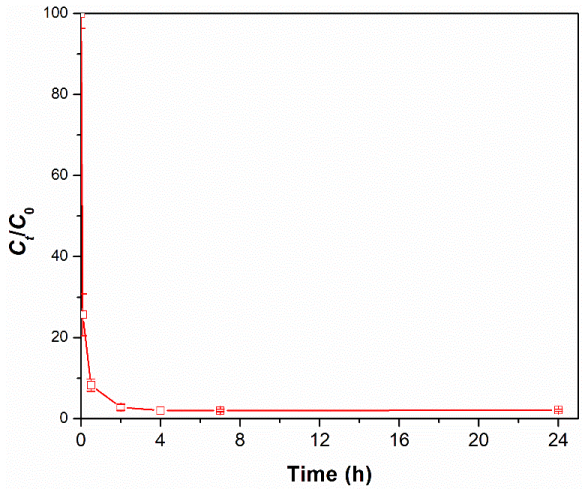

Figure 50. Re-adsorption of desorbed PFOS by 2%-Ga/TNTs@AC. Experimental conditions: mass of soil = 2 g, solution volume = 40 mL, Corexit EC9500A = 300 mg L^{-1}, material dosage = 5 g L^{-1}, pH = 7 ± 0.2, temperature = 22 ± 1 ºC.

Figure 51 compares the desorption efficiencies of fresh and treated dispersant solution (replenished with 10% fresh Corexit EC9500A) in the batch desorption systems. While the fresh dispersant eluted 77% of PFOS from the filed soil, the recycled solution eluted 54% of PFOS desorption, which is quite promising despite some inhibitive matrix effects from some dissolved soil components.

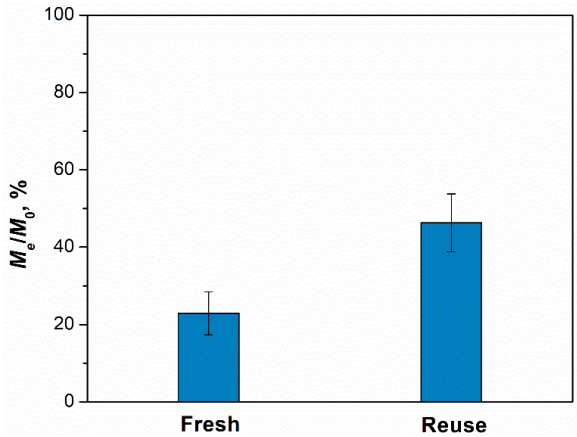

Figure 51. Equilibrium desorption of PFOS from the Willow Grove soil using fresh or recycled Corexit EC9500A. Experimental conditions: mass of soil = 2 g, solution volume = 40 mL, pH = 7 ± 0.2, temperature = 22 ± 1 ºC. M_e is the mass of PFOS remaining at equilibrium, and M_0 is the initial mass.

4.4.4. Photodegradation of re-adsorbed PFOS by Ga/TNTs@AC

Figure 52 shows that Ga/TNTs@AC degraded ~18% of the pre-loaded PFOS when the adsorption was carried out using 5 g L^{-1} of the photocatalyst, and the degradation was elevated to 30% when 10 g L^{-1} was used to adsorb the PFOS from the spent dispersant solution. The much lower degradation than in the DI water system can be attributed to: 1) the unnecessary use of too high concentration of the dispersant and inhibition from the adsorbed dispersant, 2) inhibition from some dissolved components or suspended solids, especially DOM, and 3) competition of other photo-degradable co-solutes including other PFAS. Nonetheless, 13% and 20% of PFOS were completely mineralized in the two systems, respectively.

Follow-on studies are needed to refine the dispersant recipe (at lower concentrations) and the soil washing design to minimize the dispersant need and to identify specific factors inhibiting the re-adsorption and photodegradation. In addition, different measures can be explored to enhance the photodegradation of PFOS under complex water matrix conditions, such as pretreating the PFOS-laden material including simple rising using DI water, optimizing photodegradation chemistry, adding some other photosensitizers, and modestly elevating the degradation temperature.

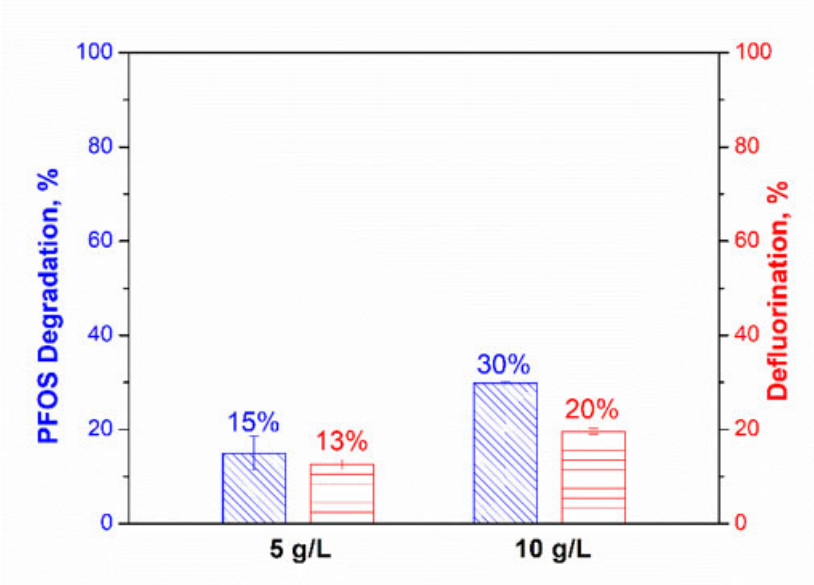

Figure 52. Degradation and defluorination of desorbed PFOS using Ga/TNTs@AC (Ga = 2 wt.%). Experimental conditions: mass of soil = 2 g, solution volume = 40 mL, Corexit EC9500 = 300 mg L^{-1}, materials dosage = 5–10 g L^{-1}, UV irradiation = 4 h, pH = 7 ± 0.2, temperature = 22 ± 1 ºC. UV: λ = 254 nm, intesntiy = 21 mW cm^{-2}.

4.5. Preliminary Process Design and Cost Analysis

Figure 53 presents a conceptualized schematic of the "Concentrate-&-Destroy" process for treating PFAS in IDW water or soil extracts. First, PFAS in water are concentrated on metal-doped TNTs@AC (M/TNTs@AC) via common fixed-bed adsorption; Second, the PFAS-loaded adsorptive photocatalyst is subjected to UV or solar light to destroy the pre-sorbed PFAS, which also regenerates the material; and Third, the photo-regenerated material is reused in another cycle of adsorption/photodegradation.

Accordingly, a preliminary order of magnitude cost analysis was carried out, which includes the material synthesis costs, adsorption costs, and photodegradation costs.

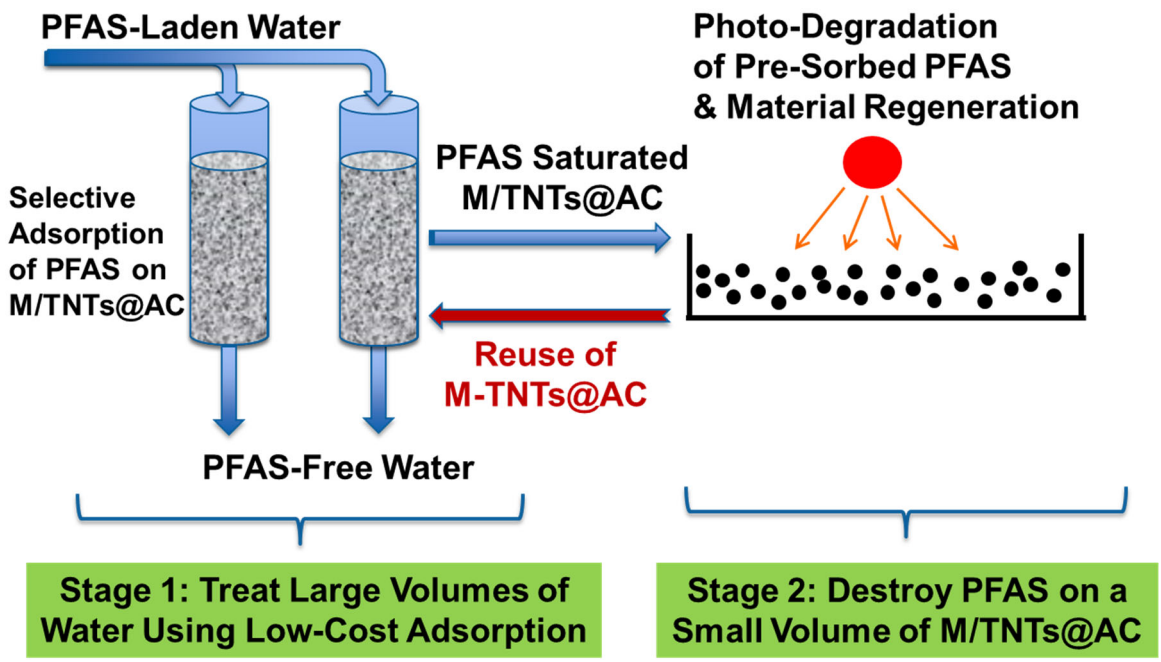

Figure 53. A conceptualized schematic diagram of the "Concentrate & Destroy" process for adsorption and destruction of PFAS in IDW water.

Assuming a treatment capacity of 0.1 MGD and PFOA being the sole target contaminant (initial PFOA = 100 µg/L), then the daily mass of PFOA to be removed is:

$$\text{Daily PFOA Mass Loading} = \frac{0.1 \times 10^6 \text{ gal}}{\text{d}} \times \frac{3.78 \text{ L}}{\text{gal}} \times \frac{100 \text{ µg}}{\text{L}} \times \frac{\text{g}}{10^6 \text{ µg}} = 37.8 \text{ g/d}$$

Based on the experimental data, the adsorption isotherm of PFOA adsorption by Fe-TNTs@AC follows the Langmuir model,

$$q_e = \frac{4.32 \times C_e}{1 + 0.049 \times C_e} \tag{17}$$

where q_e (mg/g) is the equilibrium uptake of PFOA and C_e (mg/L) is the aqueous concentration of PFOA at equilibrium. Consider a sharp breakthrough, where $C_e = C_0 = 0.1$ mg/L, then $q_e = 0.43$ mg/g upon full saturation of the material bed in the column.

The daily mass of Fe-TNTs@AC needed = PFOA Mass Loading/q_e = 37800 mg/d ÷ 0.43 mg/g = 87907 g/d = **88 kg/d**, or **0.88 kg per 1000 gal** of water treated.

Based on the bench-scale reusability test data, the same material may be used for at least 10 cycles. Consider a safety factor of 10% for unused bed and 20% for material replenishment, then the material demand is reduced to 0.88 kg/1000 gal ÷ 10 × 1.3 = **0.114 kg material/1000 gal.**

4.5.1. Costs for Fe/TNTs@AC synthesis

Costs of raw materials and chemicals. The raw materials used for preparing Fe/TNTs@AC included commercial activated carbon (AC, Filtrasorb®-400), commercial P25 (TiO_2), $FeCl_2$ (powder), commercial NaOH and tap water. **Table 6** gives the breakdown of the material costs per unit mass based on the commercial prices in the industrial grade. In the estimate, we considered a lifetime of 2 years for the AC and TiO_2, which is less than half of the designed lifetime (5 years) due to more frequent handling (photodegradation and loading/unloading abration). Assuing a service runtime of 10 days for Fe/TNTs@AC, and 250 days of operation per year, then the same materials can be reused 49 times during the lifetime (consider 10% replenishment each time). NaOH (solution) can be reused at least 10 times (with 10% replenishment each batch). AC, P25, and $FeCl_2$ are applied at the same ratio as in the bench-scale synthesis (AC:P25:Fe = 50:50:1, mass ratio). Water used for synthesis and material washing is estimated at 10-gallon water per kg material. Based on the bench-scale synthesis, 1.2 g AC and 1.2 g P25 could yield about 2.0 g Fe/TNTs@AC. **Table 6** shows that the total cost of the raw materials per kg of Fe/TNTs@AC is **$0.16**.

Table 6. Estimated costs of raw materials for synthesizing 1 kg of Fe/TNTs@AC.

Type of Material	Price	Quantity per kg material	Supplier/Source	Total Cost/kg Material
Filtrasorb®-400	$1700/ton	0.6/49*1.1 kg	Calgon Carbon Co.	$0.02
NaOH	$500/ton	0.6/10*1.1 kg	Alibaba	$0.03
P25, TiO_2	$2120/ton	0.6/49*1.1 kg	Wuhu Loman Chemical Co.	$0.03
$FeCl_2$	$5000/ton	0.01 kg	Famouschem Tech. Co.	$0.05
Industrial Water	$3.38/kGal	10 Gal		$0.03
Total				**$0.16**

Equipment and energy costs. The energy and equipment costs for Fe/TNTs@AC synthesis are estimated based on a production capacity of 5 kg per batch. To minimize the energy cost during synthesis, the furnace capacity shall be compatible with the material synthesis scale. In this case, a Nabertherm™ tube furnace (11.5kW) is considered, with an estimated equipment cost of $60,000 including all necessary parts and accessories, independent gas supply system, and a 5-year

warranty. According to the manufacturer, the equipment is designed to serve for at least 100,000 hours at 1100 °C, or $0.6/h. Consider a hydrothermal treatment time of 20 h per batch, then **the normalized equipment cost per kg of Fe/TNTs@AC** is:

$0.6/h × 20 h ÷ 5 = **$2.40**

Consider an average electrical rate of $0.13 per kWh, then the **energy cost** for 1 kg material is:

11.5kW × 20 h × $0.13/kWh ÷ 5 = **$5.98**

Nitrogen gas is also required in last step (3 hour) of synthesis. Based on our experience, one cylinder of high purity nitrogen gas ($65, Air Gas Co. Georgia) can support 15 batches of synthesis (2 mL per min). Hence, the gas cost per kg of Fe/TNTs@AC is:

$65 ÷ 15 ÷ 5 = **$0.87**

Taken together, **the total cost for preparing 1 kg of Fe/TNTs@AC** is:

$0.16 (Raw materials) + $2.40 (Equipment) + $5.98 (Energy) + $0.87 (Gas) = **$9.41/kg**

Given that the most cost is due to energy consumption, the cost may be cut down when the hydrothermal treatment and the calcination times are optimized.

When normalized to 1000 gal of water treated, the material synthesis cost is:

0.114 kg-material/1000 gal × $9.41/kg-material = **$1.07 per 1000 gallons of water**

4.5.2. Costs for PFOA adsorption

Conceptulalized fixed-bed column design and cost estimates. To facilitate a preliminary cost estimate for the adsorption process, a conceptualized fixed-bed column operation is designed following the U.S. Army Corps of Engineers' Adsorption Design Guide (DG 1110-1-2, No. 1110-1-2 1 Mar 2001).

Consider using two identical cylindrical vessels, which will be operated alternately (i.e., one in operation and the other in stand-by or photodegradation).

The bulk volume of each Fe/TNTs@AC bed is calculated via:

$$V_b = \frac{(MUR \times COP)}{\rho} = \frac{(88 \times 10)}{635} = 1.39\ m^3 = 1.39 \times 264 = 366\ gal \quad (18)$$

where MUR is the material usage rate (88 kg/d), COP is the material change out period (or service run time = 10 days), and ρ is the bulk density of the material (635 kg/m^3).

Empty Bed Contact Time (EBCT) is then calculated to be:

$$EBCT = \frac{V_b}{Q} = \frac{366}{70} = 5.2\ min \quad (19)$$

where Q is the volumetric flowrate (70 gal/min). The EBCT is in the typical range of 2-20 min.

Consider a bed height (H_b) of 1.5 m, then the cross-sectional area of the bed is:

$$A = \frac{V_b}{H_b} = \frac{1.39\ m^3}{1.5\ m} = 0.93\ m^2 \tag{20}$$

Subsequebtly, the column diameter is determined by:

$$D = \sqrt{\frac{A \times 4}{3.14}} = \sqrt{\frac{0.93 \times 4}{3.14}} = 1.18\ m \tag{21}$$

Use the standard diameter of 1.0 m, then the cross-sectional area and the design bed height are adjusted to

$$A = \pi 0.5^2 = \mathbf{0.785\ m^2} \text{ or } \mathbf{8.45\ ft^2} \tag{22}$$

$$H_b = \frac{V_b}{A} = \frac{1.39\ m^3}{0.785\ m^2} = 1.8\ m \tag{23}$$

The total column height is then

$$H_{total} = H_b(1.8) + Bed\ expansion\ (65\% H_b) + Inlet\ (1.0\ m) + Underdrain\ (0.5\ m) = \mathbf{4.5\ m} \tag{24}$$

Then the total vessel volume (TVV) for each column bed is

$$TVV = A \times H_{total} = 0.785 \times 4.5 = \mathbf{3.5\ m^3} \text{ or } \mathbf{924\ gal} \tag{25}$$

The single fiberglass pressure vessel cost is then estimated per the correlation equation by Wilbert et al. (1999),

$$Log\ C_{vessel} = 3.446 + 0.562 \times \log(TVV) = 3.446 + 0.562 \times \log(3.5) \tag{26}$$

Thus, C_{vessel} = \$5,646, which is is then converted to the 2018 dollars using the Chemical Engineering Plant Cost Index (CEPCI). In this case, the scaling factor for 2018 dollars is ~1.6, and hence, **C_v for the two vessels** is 1.6 x 5646 x 2 = **\$18,067** in 2018 dollars.

$$\text{First time material purchase cost} = 88\frac{\text{kg}}{\text{d}} \times 10\ \text{d} \times \frac{9.4\$}{\text{kg}} \times 1.5 \times 2 = \$24{,}816 \tag{27}$$

where the factor 1.5 is for 50% extra and 2 is for the two columns.

To calculate the headloss, the sperfacial liquid velocity (SLV) is calculated by

$$SLV = \frac{Q}{A} = \frac{70 gal/min}{0.93\ m^2}\frac{1 m^3}{264 gal}\frac{60\ min}{1\ h} = 17.1\ m/h \tag{28}$$

According to the manufacture data, the downflow headloss through the Filtrasorb 400 is ~45 mbar/m, thus the headloss through the bed is:

$$h_b = 45\frac{mbar}{m} \times 1.8\ m = 81 mbar\frac{14.5\ psi}{bar}\frac{1\ bar}{1000\ mbar} = 1.175\ psi \tag{29}$$

Considering the particle size may be smaller due to abrasion and pipeline headloss, we give a 2 times higher safety factor, then the design headloss for pump selection is

$$h_b = 2 \times 1.175 = 2.35\ psi \tag{30}$$

As such, the flowrate x pressure for the pump is:

$$Q \times h_b = 70\ gpm \times 2.35\ psi = 165\ (HP) \tag{31}$$

Based on the Q×h_b value, two standard centrifugal pumps are selected, each costing $2,500 (Garret, 1989, and current market price). Then the total pump cost is:

$$\boldsymbol{Total\ pump\ cost} = 2500 \times 2 = \$5{,}000 \tag{32}$$

Total capital investment (TCI). The total capital investment can be estimated based on historical data and the method by Sorrels et al. (2018), using the cost data above for the vessels, Fe/TNTS@AC, and pumps as the base purchased equipment cost. The typical lifetime for carbon adsorbers is 15 to 25 years (Sorrels et al., 2018), and we choose the average of 20 years for the capital investiment in this estimate. **Table 7** presents the itemized capital cost estimates.

Thus the annual total capital investiment per 1,000 gal of water is **$0.24/kgal.**

Table 7. Itemized capital costs for the adorpion of PFOA using Fe/TNTs@AC.

Cost Item	Estimated Cost
Direct Costs	
Purchased equipment costs	
Adsorber vessels and carbon	$42,883
Pumps	$5,000
Sum=A	$47,883
Instrumentation, 0.1 A	$0
Freight, 0.05 A	$2,394
Purchased equipment cost (B)	**$50,277**
Direct installation costs	
Foundation & supports, 0.08 B	$4,022
Handling & erectino, 0.14 B	$7,039
Electrical, 0.04B	$2,011
Piping, 0.02B	$1,006
Insulation for ductwork, 0.01 B	$503
Painting, 0.01 B	$503
Direct installation costs	**$15,083**
*Site work and miscellaneous	**$6,000**
*Buildings and concrete	**$20,500**
Total Direct Costs (DC)	**$91,860**
Indirect Costs (installation)	
Engineering, 0.10 B	$5,028
Construction and field expenses, 0.05 B	$2,514
Start-up, 0.02 B	$1,006
Performance test, 0.01 B	$503
Total Indirect Cost (IC)	**$9,050**
Contractor Fees, 0.10 (DC+IC)	**$10,091**
Contingencies (C), CF (DC+IC+contractor Fees), CF=0.1	**$11,100**
Total Capital Investment (TCI)	**$122,101**
Total Capital Investment (TCI) Per Year	**$6,105**
Gallons of water treated per year (250 days operation)	**$25,200,000**
Total Capital Investment (TCI) Per 1,000 Gallons of Water Treated	**$0.24**

* Esimated based on the cost data by Rubel (2003), which were deducted by 50% assuming that no permernant building is needed for the DoD sites. The purpose of the building is to protect

the equipment from freezing or overheating not for operator comfort.

Operating costs. The primary operating costs include: 1) Treatment chemical costs, 2) Operating labor costs, 3) Utility costs, 4) Replacement adsorbent/photocatalyst costs, and 5) Replacement parts and miscellaneous materials.

In this estimate, the method by Rubel (2003) is used, who estimated the cost for an ion exchange process. The following design parameters or conditions are considered:

Flowrate = 70 gpm
Annual average utilization = 250 days
Number of material synthesis per year = 6
Numer of photodegradation = 6
Operator annual salary = $35,000
Overhead and fringe benefits = 30%
Available manhours per year = 2,000/man

The chemicals are mainly used in the material synthesis, and have been included in the material cost (captical cost and material replacement cost below). Likewise, the material replacement costs are also included in the material synthesis.

One parttime operator is needed, and **Table 8** gives the cost breakdowns for the labor.

Table 8. Cost breakdowns for operating labor costs.

Cost Breakdowns	Hours	Estimated Cost
Number of hours on material synthesis/year: 8 × 5 hr = 40 hr	60	
Number of hours on photodegradation/year: 24 × 4 hr = 24 hr	96	
Number of hours on routine operation/year: 250 × 1.5 = 500 hr	375	
Number of hours on extra tasks/year: 50 × 1 hr = 50 hr	50	
Total plant operator time	**581**	
Operator hourly rate: $35,000/2,000 hr		$18
30% (overhead and fringe benefits)		$5
Total operator rate per hour		**$23**
Total annual operator cost		**$13,218**
Annual water treated:		
250/365 × (70 gpm) × 1,440 min/day × 365 days/year = 25,200,000		
Operator cost per 1000 gal water treated		**$0.52**

The utility cost is mainly due to electric cost. The treatment units are expected to act as heat sinks maintaining an insulated building at a temperature near that of the raw water. In cold climates, the building should have an auxiliary heat source to prevent pipes from freezing if water is not flowing (Rubel, 2003). The cost covers the the following functions: 1) Pumps, 2) Instrumentation and alarms, 3) Lighting, and 4) Convenience receptacle.

Electric utility rates may vary considerably with local climate and geographic conditions. In August 2001, the rates varied from $0.03 to $0.20/KWH, and the electric utility cost can range from $0.001 to $0.01 per 1,000 gal water under normal conditions (Rubel, 2003).

Based on the historical data, we use the cap value of **$0.01 per 1,000 gal water** as a

conservative estimate for the **utility cost** in this design.

Finally, an operating allowance of **$0.01/1,000 gal of treated water** is added to cover the **replacement parts and miscellaneous material costs** (Rubel, 2003). Parts and miscellaneous materials include small consumables such a pump, diaphragms, seals, and replacement pump heads, which should be kept in stock in the treatment plant to prevent extended plant shutdown in the event a part is required. Also included are consumables such as chemicals, laboratory reagents (and glassware), and record keeping supplies (Rubel, 2003).

Consequenlty, **Table 9** summarizes the itemized operating costs for the adsorption of PFOA.

Table 9. Summary of itemized operating costs per 1,000 gal of water treated by adsorption.

Operating Cost Items	Estimated Cost ($ per 1,000 gal water)
Fe/TNTs@AC synthesis	$1.07
Operator labor	$0.52
Utility	$0.01
Replacement parts and consumables	$0.01
Total plant operating cost	**$1.61**

The total adsorption treatment cost = $0.24 (Captical) + $1.61 (Operating) = **$1.85/1,000 gal. water**

4.5.3 Costs for photocatalytic degradation/destruction of PFOA

UV system equipment costs. The UV system is designed based on the EPA manual (EPA, 2014) and available Aquionics LED UV Systems designed for disinfection of municipal wastewater. The photodegradation of the pre-concentrated PFOA can also be envisioned as a regeneration system for the adsorptive photocatalyst.

The photodegradation will be carried out once every 10 days of service run. Thus, the volume of the material to be treated will be 880 kg or 1.39 m^3 per bulk bed volume (Eqn. 18). Consider adding 10 bed volumes of water to facilitate the photodegradation, then the total volume of the Fe/TNTs@AC and water mixture shall be

$$\text{Volume of photocatalyst and water mixture for UV treatment } = 13.9\ m^3\ or\ 3670\ gal \quad (33)$$

According to the bench-scale data, ~90% of pre-adsorbed PFOA can be degraded in 4 h of UV irradiation at an energy input of 21 mW/cm^2, or ~6 h for 100% PFOA degradation. To shorten the exposure time, two Aquionics Berson InLine® UV-Systems will be operated in parallel, which offer an average UV intensity of 170 mW/cm^2. Based on the equivalent irradiance intensity, and assuming the bench-scale photodegradation efficiency can be linearly scaled up, then the irradiation time is shortened to

$$6\ \text{h} \times 21\ \text{mW/cm}^2 \div 170\ \text{mW/cm}^2 \times 1.2\ = 0.89\ \text{h} \quad (34)$$

where the factor 1.2 accounts for a 20% safety factor.

Accoridng to our communication with Aquionics, the UV unit can be easily modified to include an axial mixing to keep the particles suspended. The interior volume (IV) is ~0.1 m^3, and given the hydraulic residence time (HRT) of 0.89 h, the feeding flowrate for each reactor is,

$$Flowrate\ for\ each\ photoreactor = \frac{IV}{HRT} = \frac{0.1}{0.89} = 0.11\frac{m^3}{h}\ or\ 0.49\ gpm \quad (35)$$

Then the time to complete the photodegradation is,

$$Time\ for\ each\ photodegradation\ run = \frac{3670\ gal}{0.49\times 2\ gpm}\frac{1\ hr}{60\ min} = 62.4\ \text{hr} \quad (36)$$

Table 10 lists itemized costs of the UV systems and the ancillaries according to the company quotation and the cost data from EPA (2014). In addition, two Cole-Parmer Peristaltic Pumps shall be used two feed the reactor, each costing $1,895.

Table 10. Capital cost breakdowns for the photodegradation system.

Cost Element	Lifetime	Unit Cost	Quantity	Total Cost
UV Unit + Control Panel	20 yr	$75,000	2	$150,000
Mixer blades and Reactor Midification	20 yr	$3,750	2	$7,500
Total UV System				**$157,500**
Pumps	10	$1,895	2	**$3,790**
Total Annual Cost				**$8,254**
Cost Per 1,000 gal Water				**$0.33**

Notes: a) No spare UV unit or pump is needed as one unit can also fullfil the tasks with time doubled during a potential down time.

Photodergadation operating costs. The labor cost has been included in **Table 8**. The main operating cost for the photodegradation system is then due to the energy consumption, which can be calculated as follows:

$$\textbf{UV degradation Energy Cost } (\$/\textbf{1000 gallons water}) = 1000 \times \frac{\text{E} \times \text{F}}{25200000} \quad (37)$$

where E is the annual power consumption (kWh) (including sensors and lamps), and F is the electricity rate ($/kWh). The maximum electricity consumption of the UV unit is ~2.5 kW. The annual operating hours are

$$Annual\ photodegradation\ operating\ time = 24\ (total\ numer\ of\ runs) \times 62.4\ hr\ per\ run = 1498\ hr \quad (38)$$

Then cost per 1000 gal of water is

$$Annual\ power\ cost\ per\ 1000\ gal\ water = 2 \times 2.5\ kW \times \frac{1497\ h}{yr} \times \frac{\$0.13}{kWh} \times \frac{1}{25200} = \$0.04 \quad (39)$$

Consider another $0.01/1.000 gal for the pumps, then the total energy cost for the photodegradation will be **$0.05 per 1000 gallons water**.

Therefore, the total cost for the photodegradation phase is

$$\boldsymbol{Total\ photodegradation\ cost} = \$0.33\ (Capital) + \$0.05(Operating) = \boldsymbol{\$0.38\ per\ 1000\ gal\ water} \quad (40)$$

Therefore, **the overall treatment cost** is $1.85 (Adsorption) + $0.38 (Photodegradation)

= **$2.23 per 1,000 gal of water**

The process is expected completely decompose PFOA (100% degraded and 62% mineralized) and generates no PFOA-laden waste residuals (water or solid).

Cost comparison with incineration and landfill. The photodegradation also regenerates the material for repeated uses, representing a great cost saving. For instance, if activated carbon is used and then incinerated after one time saturation run, it would need not only at least 10 times more of the adsorbent material (880 kg/d), but also a very high incineration cost for the PFOA-laden AC. According to the literature report, the cost for a small scale incineration plant is about $1,026 per ton of solid/hazardous waste (https://wteinternational.com/cost-of-incineration-plant/). Thus, the cost for using incineration in this 0.1 MGD design would be

$$Incineration\ cost\ for\ treating\ spent\ AC = \frac{880\ kg}{1\ d}\frac{250\ d}{1\ yr}\frac{\$1.026}{1\ kg}\frac{1\ yr}{25200\ gal} = \frac{\$9.0}{1{,}000 gal} \quad (41)$$

Thus, incineration of the spent material would cost *24 times* more than the photocatalytic regeneration and resue of the material. Overall, the carbon adsorption followed by incineration would cost 9.1 timers more than the "Adsorption-&-Photodegradation" process.

When compared to landfill treatment of the FPOA-laden AC, the treatment cost ranges from $0.27 to $0.46 per kg depending on the nature of hazardous materials and methods of excavation (https://frtr.gov/matrix2/section4/4-29.html). Taking the mean value ($0.365/kg) as an example, the disposal cost would be

$$Landfill\ cost\ for\ treating\ spent\ AC = \frac{880\ kg}{1\ d}\frac{250\ d}{1\ yr}\frac{\$0.365}{1\ kg}\frac{1\ yr}{25200\ gal} = \frac{\$3.2}{1{,}000 gal} \quad (42)$$

Thus, landfill disposal of the spent material would cost 8.4 *times* more than the photocatalytic regeneration and reuse of the material. Overall, the carbon adsorption followed by landfill would cost 6.5 timers more than the "Adsorption-&-Photodegradation" process. Moreover, the ladnfilled PFAS may still leach into the environment.

In conclusion, the "Concentrate-&-Destory" process by Fe/TNTs@AC is much more cost-effective than current practices for complete degradation or destruction of PFOA, or likely other PFAS in water.

5. Conclusions and Implications for Future Research

In this SEED project, we proposed and extensively tested a novel innovative "Concentrate-&-Destroy" strategy for cost-effective and complete destruction of PFAS in IDWs. The key findings are summarized as follows:

- Three reusable adsorptive photocatalysts were prepared based on low-cost and well-accepted commercial materials (AC and TiO_2);
- As an adsorbent, the materials can effectively adsorb/concentrate PFAS from water through commonly used reactor configurations (fixed-bed column or batch reactor); as a photocatalyst, the materials can rapidly and completely degrade PFOA and PFOS under UV or solar light;
- The carbon and metal modifications of TNTs or iron oxide not only facilitate selective adsorption of PFAS, but greatly enhance the photocatalytic degradation;
- The *in situ* efficient photodegradation of PFAS also regenerates the materials, allowing for repeated uses of the photocatalysts without incurring costly chemical regeneration and without generation of waste residuals;
- Dilute Corexit EC9500A can serve as an effective, safe and low-cost extractant for removing PFOS and PFOA from field soil, and the "Concentrate-&-Destroy" technique can be applied to treat the spent dispersant solution so as to reuse the solution and destroy the PFAS.

The "Concentrate-&-Destroy" strategy offers some unprecedented advantages over conventional approaches, such as adsorption, landfill and incineration, to treat persistent organic pollutants, including:

- It treats low concentrations of PFAS in large volumes of water using low-cost and easy-to-operate adsorption process, and then completely destroys the concentrated PFAS *in situ* through highly efficient photocatalytic approach, representing significant cost savings;
- Based on a preliminary cost analysis for a hypothetical 0.1 MGD treatment system, the overall cost for the "Concentrate-&-Destroy" process is $2.23 for complete degradation of PFOA in 1,000 gal of water, which is 9.1 and 6.5 times lower than AC adsorption followed by incineration and landfill, respectively.
- It eliminates the need for costly and toxic chemical/solvents for regeneration, and generates little or no process waste residual;
- The system can be easily applied on site and is easier to operate, and can be made mobile and "deployed easily, minimizing the spatial footprint and mobilization time and effort";
- It holds the potential to achieve "unrestricted disposal, discharge, and/or reuse of IDW on-site" upon some follow-on studies, and will greatly aid DoD Remedial Project Managers in more effective management of the PFAS-contaminated sites.

This intensive SEED effort directly addressed the SERDP's critical need to develop "more cost-effective and efficient technologies for treatment of IDW from PFAS investigations". The findings provide compelling evidence for a brand new strategy for "green", cost-effective and

efficient destruction of PFAS. The "Concentrate-&-Destroy" strategy meets the DoD's preference "for destructive technologies" "so as to avoid potential future environmental liability" associated with PFAS.

Based on the findings, we anticipate that the new technology will potentially equip the DoD Remedial Project Managers with a powerful on-site treatment approach in treating PFAS at hundreds of the DoD sites. To this end, the following follow-on research activities are warranted:

- ✓ The adsorptive photocatalysts can be further optimized in terms of selectivity for PFAS and photoactivity by tuning the parent materials, the dopants, and synthesis conditions towards more efficient mineralization of PFAS, especially for PFAS in soil extracts;
- ✓ Composite materials that are more reactive under solar light should be further explored;
- ✓ Further investigations are needed to test the effectiveness under DoD field water/soil conditions to identify potential inhibitions of the water matrix and find out ways to overcome these inhibitive effects and to optimize the water chemistry conditions;
- ✓ Pilot-scale experiments should be carried out to facilitate more realistic assessment of the technical and economic effectiveness and to guide field application design;
- ✓ Desorption of PFAS from soil can be further optimized by adjusting the solution recipe and chemistry to facilitate more efficient desorption of PFAS and to promote subsequent photodegradation;
- ✓ Water chemistry conditions can be optimized to promote photocatalytic degradation of more persistent PFAS or PFAS from the dispersant solutions, including addition of proper photosensitizers and elevation of reaction temperature; and
- ✓ To promote earliest possible field adoption, various technology transition/transfer measures should be taken immediately following the pilot-testing, first towards the DoD end users, and then the market at large (e.g., landfill leachate and groundwater sites).

6. Literature Cited

Backe, W.J., Day, T.C., Field, J.A. (2013) Zwitterionic, cationic, and anionic fluorinated chemicals in aqueous film forming foam formulations and groundwater from US military bases by nonaqueous large-volume injection HPLC-MS/MS. Environmental Science & Technology 47(10), 5226-5234.

Bahnemann, D.W., Hilgendorff, M., Memming, B. (1997) Charge carrier dynamics at TiO_2 particles: reactivity of free and trapped holes. The Journal of Physical Chemistry B 101, 4265-4275.

Birben, N.C., Uyguner-Demirel, C.S., Kavurmaci, S.S., Gürkan, Y.Y., Turkten, N., Cinar, Z., Bekbolet, M. (2017) Application of Fe-doped TiO_2 specimens for the solar photocatalytic degradation of humic acid. Catalysis Today 281, 78-84.

Casalongue, H.S., Kaya, S., Viswanathan, V., Miller, D.J., Friebel, D., Hansen, H.A., Nørskov, J.K., Nilsson, A., Ogasawara, H. (2013) Direct observation of the oxygenated species during oxygen reduction on a platinum fuel cell cathode. Nature Communications 4, 2817.

Chandiran, A.K., Sauvage, F., Etgar, L., Graetzel, M. (2011) Ga^{3+} and Y^{3+} cationic substitution in mesoporous TiO_2 photoanodes for photovoltaic applications. The Journal of Physical Chemistry C 115(18), 9232-9240.

Chen, J., Zhang, P., Liu, J. (2007) Photodegradation of perfluorooctanoic acid by 185 nm vacuum ultraviolet light. Journal of Environmental Sciences 19(4), 387-390.

Chen, M., Lo, S., Lee, Y., Huang, C. (2015) Photocatalytic decomposition of perfluorooctanoic acid by transition-metal modified titanium dioxide. Journal of Hazardous Materials 288, 168-175.

Chen, Q., Zhou, W., Du, G., Peng, L. (2002) Trititanate nanotubes made via a single alkali treatment. Advanced Materials 14(17), 1208-1211.

Chen, Y., Lo, S., Kuo, J. (2011) Effects of titanate nanotubes synthesized by a microwave hydrothermal method on photocatalytic decomposition of perfluorooctanoic acid. Water Research 45(14), 4131-4140.

Cheng, J., Liang, X., Yang, S., Hu, Y. (2014) Photochemical defluorination of aqueous perfluorooctanoic acid (PFOA) by VUV/Fe^{3+} system. Chemical Engineering Journal 239, 242-249.

Chou, W., Lin, Z. (2019) Bayesian evaluation of a physiologically based pharmacokinetic (PBPK) model for perfluorooctane sulfonate (PFOS) to characterize the interspecies uncertainty between mice, rats, monkeys, and humans: Development and performance verification. Environment International 129, 408-422.

Deng, S., Nie, Y., Du, Z., Huang, Q., Meng, P., Wang, B., Huang, J., Yu, G. (2015) Enhanced adsorption of perfluorooctane sulfonate andperfluorooctanoate by bamboo-derived granular activated carbon. Journal of Hazardous Materials 282, 150-157.

Deng, S., Niu, L., Wang, B., Huang, J., Yu, G. (2013) Adsorption of perfluorinatedcompounds on an aminated rice husk prepared by atom transfer radical poly-merization. Chemosphere 91, 124-130.

Deng, S., Yu, Q., Huang, J., Yu, G. (2010) Removal of perfluorooctane sulfonate from wastewater by anion exchange resins: effects of resin properties and solution chemistry. Water Research 44, 5188-5195.

Deng, S., Zhang, Q., Nie, Y., Wei, H., Wang, B., Huang, J., Yu, G., Xing, B. (2012) Sorption mechanisms of perfluorinated compounds on carbon nanotubes. Environmental Pollution

168, 138-144.
Deshpande, A.S., Shchukin, D.G., Ustinovich, E., Antonietti, M., Caruso, R.A. (2005) Titania and mixed titania/aluminum, gallium, or indium oxide spheres: sol–gel/template synthesis and photocatalytic properties. Advanced Functional Materials 15, 239-245.
Dillert, R., Bahnemann, D., Hidaka, H. (2007) Light-induced degradation of perfluorocarboxylic acids in the presence of titanium dioxide. Chemosphere 67, 785-792.
Du, Z., Deng, S., Bei, Y., Huang, Q., Wang, B., Huang, J. Yu, G. (2014) Adsorption behavior and mechanism of perfluorinated compounds on various adsorbents-a review. Journal of Hazardous Materials 274, 443-454.
Duan, J., Liu, W., Zhao, X., Han, Y., O'Reilly, S., Zhao, D. (2018) Study of residual oil in Bay Jimmy sediment 5 years after the Deepwater Horizon oil spill: Persistence of sediment retained oil hydrocarbons and effect of dispersants on desorption. Science of the Total Environment 618, 1244-1253.
Dudley, L.A. (2012) Removal of Perfluorinated Compounds by Powdered Activated Carbon, Superfine Powder Activated Carbon, and Anion Exchange Resin. Thesis submitted to the Graduate Faculty of the North Carolina State University, US.
Espana, V.A.A., Mallavarapu, M., Naidu, R. (2015) Treatment technologies for aqueous perfluorooctane sulfonate (PFOS) and Perfluorooctanoate (PFOA): A critical review with an emphasis on field testing. Environtal Technology & Innovation 4, 168-181.
Gao, X., Chorover, J. (2012) Adsorption of perfluorooctanoic acid and perfluorooctanesulfonic acid to iron oxide surfaces as studied by flow-through ATR-FTIR spectroscopy. Environmental Chemistry 9(2), 148-157.
Gatto, S., Sansotera, M., Persico, F., Gola, M., Pirola, C., Panzeri, W., Navarrini, W., Bianchi, C.L. (2015) Surface fluorination on TiO_2 catalyst induced by photodegradation of perfluorooctanoic acid. Catalysis Today 241, 8-14.
Gong, Y., Wang, L., Liu, J., Tang, J., Zhao, D. (2016) Removal of aqueous perfluorooctanoic acid (PFOA) using starch-stabilized magnetite nanoparticles. Science of the Total Environment 562, 191-200.
Gong, Y., Zhao, X., O'Reilly, S.E., Qian, T., Zhao, D. (2014) Effects of oil dispersant and oil on sorption and desorption of phenanthrene with Gulf Coast marine sediments. Environmental Pollution 185, 240-249.
Higgins, C.P., Field, J.A., Criddle, C.S., Luthy, R.G. (2005) Quantitative determination of perfluorochemicals in sediments and domestic sludge. Environmental Science & Technology 39, 3946-3956.
Hori, H, Yamamoto, A., Hayakawa, E., Taniyasu, S., Yamashita, N., Kutsuna, S., Kiatagawa, H., Arakawa, T. (2005) Efficient decomposition of environmentally persistent perfluorocarboxylic acids by use of persulfate as a photochemical oxidant. Environtal Science & Technology 39, 2383-2388.
Hu, X.C., Andrews, D.Q., Lindstrom, A.B., Bruton, T.A., Schaider, L.A., Grandjean, P., Lohmann, R., Carignan, C.C., Blum, A., Balan, S.A., Higgins, C.P., Sunderland, E.M. (2016) Detection of poly-and perfluoroalkyl substances (PFASs) in US drinking water linked to industrial sites, military fire training areas, and wastewater treatment plants. Environmental Science & Technology Letters 3, 344-350.
Ismail, A.A., Abdelfattah, I., Faisal, M., Helal, A. (2018) Efficient photodecomposition of herbicide imazapyr over mesoporous Ga_2O_3-TiO_2 nanocomposites. Journal of Hazardous Materials 342, 519-526.

Jia, Z., Peng, K., Li, Y., Zhu, R. (2011) Preparation and application of novel magnetically separable γ-Fe_2O_3/activated carbon sphere adsorbent. Materials Science and Engineering: B 176, 861-865.
Kerisit, S., Zarzycki, P., Rosso, K.M. (2015) Computational molecular simulation of the oxidative adsorption of ferrous iron at the hematite (001)–water interface. The Journal of Physical Chemistry C 119, 9242-9252.
Land, M., de Wit, C.A., Bignert, A., Cousins, I.T., Herzke, D., Johansson, J.H., Martin, J.W. (2018) What is the effect of phasing out long-chain per-and polyfluoroalkyl substances on the concentrations of perfluoroalkyl acids and their precursors in the environment? A systematic review. Environmental Evidence 7(1), 4.
Li, F., Du, P., Liu, W., Li, X., Ji, H., Duan, J., Zhao, D. (2018) Hydrothermal synthesis of graphene grafted titania/titanate nanosheets for photocatalytic degradation of 4-chlorophenol: Solar-light-driven photocatalytic activity and computational chemistry analysis. Chemical Engineering Journal 331, 685-694.
Li, F., Duan, J., Tian, S., Ji, H., Zhu, Y., Wei, Z., Zhao, D. (2020) Short-chain per-and polyfluoroalkyl substances in aquatic systems: Occurrence, impacts and treatment. Chemical Engineering Journal 380, 122506.
Liang, X., Cheng, J., Yang, C., Yang, S. (2016) Factors influencing aqueous perfluorooctanoic acid (PFOA) photodecomposition by VUV irradiation in the presence of ferric ions. Chemical Engineering Journal 298, 291-299.
Liu, J., Zhu, R., Chen, Q., Zhou, H., Liang, X., Ma, L., Parker, S.C. (2019) The significant effect of photo-catalyzed redox reactions on the immobilization of chromium by hematite. Chemical Geology 524, 228-236.
Liu, K., Zhang, S., Hu, X., Zhang, K., Roy, A., Yu, G. (2015) Understanding the adsorption of PFOA on MIL-101 (Cr)-based anionic-exchange metal–organic frameworks: comparing DFT calculations with aqueous sorption experiments. Environmental Science & Technology 49, 8657-8665.
Liu, W., Cai, Z., Zhao, X., Wang, T., Li, F., Zhao, D. (2016) High-capacity and photoregenerable composite material for efficient adsorption and degradation of phenanthrene in water. Environmental Science & Technology 50, 11174-11183.
Ma, J., Li, F., Qian, T., Liu, H., Liu, W., Zhao, D. (2017) Natural organic matter resistant powder activated charcoal supported titanate nanotubes for adsorption of Pb (II). Chemical Engineering Journal 315, 191-200.
Mao, Y., Wong, S. (2006) Size-and shape-dependent transformation of nanosized titanate into analogous anatase titania nanostructures. Journal of the American Chemical Society 128, 8217-8226.
Martin, J.W., Asher, B.J., Beesoon, S., Benskin, J.P., Ross, M.S. (2010) PFOS or PreFOS? Are perfluorooctane sulfonate precursors (PreFOS) important determinants of human and environmental perfluorooctane sulfonate (PFOS) exposure? Journal of Environmental Monitoring 12, 1979-2004.
Moody, C.A., Field, J.A. (2000) Perfluorinated surfactants and the environmental implications of their use in fire-fighting foams. Environmental Science & Technology 34, 3864-3870.
Mulligan, C., Yong, R., Gibbs, B. (2001) Surfactant-enhanced remediation of contaminated soil: A review. Engineering Geology, 60, 371-380.
Noerpel, M.R., Lee, S.S., Lenhart, J.J. (2016) X-ray analyses of lead adsorption on the (001), (110), and (012) hematite surfaces. Environmental Science & Technology 50, 12283-12291.

Ochoa-Herrera, V., Sierra-Alvarez, R. (2008) Removal of perfluorinated surfactants by sorption onto granular activated carbon, zeolite and sludge. Chemosphere 72, 1588-1593.
Ohno, M., Ito, M., Ohkura, R., Kose, T., Okuda, T., Nakai, S., Kawata, K., Nishijima, W. (2014) Photochemical decomposition of perfluorooctanoic acid mediated by iron in strongly acidic conditions. Journal of Hazardous Materials 268, 150-155.
Pan, G., Jia, C., Zhao, D., You, C., Chen, H., Jiang, G. (2009) Effect of cationic and anionic surfactants on the sorption and desorption of perfluorooctane sulfonate (PFOS) on natural sediments. Environmental Pollution 157, 325-330.
Panchangam, S.C., Lin, Y., Shaik, K.L., Lin, C. (2009) Decomposition of perfluorocarboxylic acids by heterogeneous photocatalysis in acidic aqueous medium. Chemosphere, 77, 242-248.
Panchangam, S.C., Yellatur, C.S., Yang, J.S., Loka, S.S., Lin, A.Y.C., Vemula, V. (2018) Facile fabrication of TiO_2-graphene nanocomposites (TGNCs) for the efficient photocatalytic oxidation of perfluorooctanoic acid (PFOA). Journal of Environmental Chemical Engineering 6, 6359-6369.
Pancras, T., Plaisier, W., Barbier, A. (2013) Challenges of PFOS remediation. Proceedings of the AquaConCoil Conference, Barcelona, ES, 2013.
Paterson, L., Kennedy, T.S., Sweeney, D. (2008) Remediation of perfluorinated alkyl compounds at a former fire fighting training area. Proceedings of the Remediation Technologies Symposium, Banff, AB, 2008.
Place, B.J., Field, J.A. (2012) Identification of novel fluorochemicals in aqueous film-forming foams used by the US military. Environtal Science & Technology 46, 7120-7127.
Pradhan, G.K., Parida, K. (2011) Fabrication, growth mechanism, and characterization of α-Fe_2O_3 nanorods. ACS applied materials & interfaces 3(2), 317-323.
Peng, Y.P., Chen, H., Huang, C.P. (2017) The synergistic effect of photoelectrochemical (PEC) reactions exemplified by concurrent perfluorooctanoic acid (PFOA) degradation and hydrogen generation over carbon and nitrogen codoped TiO_2 nanotube arrays (CN-TNTAs) photoelectrode. Applied Catalysis B: Environmental 209, 437-446.
Quiñones, D.H., Rey, A., Álvarez, P.M., Beltrán, F.J., Plucinski, P.K. (2014) Enhanced activity and reusability of TiO_2 loaded magnetic activated carbon for solar photocatalytic ozonation. Applied Catalysis B: Environmental 144, 96-106.
Rey, A., Quiñones, D.H., Álvarez, P.M., Beltrán, F.J., Plucinski, P.K. (2012) Simulated solar-light assisted photocatalytic ozonation of metoprolol over titania-coated magnetic activated carbon. Applied Catalysis B: Environmental 111, 246-253.
Schaefer, T., Dlugogorski, B., Kennedy, E. (2008) Sealability properties of fluorine-free fire-fighting foams (FfreeF). Fire Technoloy, 44, 297-309.
Schwertmann, U., Friedl, J., Stanjek, H. (1999) From Fe (III) ions to ferrihydrite and then to hematite. Journal of colloid and interface science. Journal of Colloid and Interface Science 209, 215-223.
SEDRP (2016) FY 2017 Statement of Need: In situ and ex situ remediation of per and polyfluoroalkyl substance contaminated groundwater. SON Number: ERSON-18-C2, October 27, 2016.
SERDP (2017) FY 2018 Statement of Need: Innovative approaches for treatment of waste derived from per- and polyfluoroalkyl substance (PFAS) subsurface investigations. SON Number: ERSON-18-L1, September 14, 2017.
Seredych, M., Bandosz, T.J. (2011) Removal of dibenzothiophenes from model diesel fuel on

sulfur rich activated carbons. Applied Catalysis B: Environmental 106, 133-141.
Shan, G., Yang, L., Zhao, J., Liu, N., Cui, H., Zhong, W., Zhu, L. (2019) Identification and quantification of perfluorooctane sulfonamide isomers by liquid chromatography-tandem mass spectrometry. Journal of Chromatography A 1594, 65-71.
Shao, T., Zhang, P., Jin, L., Li, Z. (2013) Photocatalytic decomposition of perfluorooctanoic acid in pure water and sewage water by nanostructured gallium oxide. Applied Catalysis B: Environmental 142, 654-661.
Sivula, K., Le Formal, F., Grätzel, M. (2011) Solar water splitting: progress using hematite (α-Fe_2O_3) photoelectrodes. ChemSusChem 4, 432-449.
Sleiman, N., Deluchat, V., Wazne, M., Mallet, M., Courtin-Nomade, A., Kazpard, V., Baudu, M. (2017) Phosphate removal from aqueous solutions using zero valent iron (ZVI): Influence of solution composition and ZVI aging. Colloids and Surfaces A: Physicochemical and Engineering Aspects 514, 1-10.
Sorrels, J.L., Baynham, A., Randall, D.D. and Schaffner, K.S., 2018. Carbon Adsorbers.USEPA.
Sun, X., Li, Y. (2003) Synthesis and characterization of ion-exchangeable titanate nanotubes. Chemistry–A European Journal 9, 2229-2238.
Tang, H., Xiang, Q., Lei, M., Yan, J., Zhu, L., Zou, J. (2012) Efficient degradation of perfluorooctanoic acid by UV–Fenton process. Chemical Engineering Journal 184, 156-162.
Thrower, P.A. (1996) Chemistry & physics of carbon. CRC Press, Marcel Dekker, NY.
USDOE (2017) Water and Wastewater Annual Price Escalation Rates for Selected Cities across the United States. DOE/EE-1670 7781.
Vecitis, C.D., Park, H., Cheng, J., Mader, B.T., Hoffmann, M.R. (2009) Treatment technologies for aqueous perfluorooctanesulfonate (PFOS) and perfluorooctanoate (PFOA). Frontiers of Environmental Science & Engineering in China 3(2), 129-151.
Voelker, B.M., Morel, F.M., Sulzberger, B. (1997) Iron redox cycling in surface waters: effects of humic substances and light. Environmental Science & Technology 31, 1004-1011.
Wang, S., Yang, Q., Chen, F., Sun, J., Luo, K., Yao, F., Wang, X., Wang, D., Li, X., Zeng, G. (2017) Photocatalytic degradation of perfluorooctanoic acid and perfluorooctane sulfonate in water: a critical review. Chemical Engineering Journal 328, 927-942.
Wang, Y., Sun, H., Ang, H.M., Tadé, M.O., Wang, S. (2014) Magnetic Fe_3O_4/carbon sphere/cobalt composites for catalytic oxidation of phenol solutions with sulfate radicals. Chemical Engineering Journal 245, 1-9.
Wang, Y., Zhang, P. (2011) Photocatalytic decomposition of perfluorooctanoic acid (PFOA) by TiO_2 in the presence of oxalic acid. Journal of Hazardous Materials 192, 1869-1875.
Wang, Y., Zhang, P., Pan, G., Chen, H. (2008) Ferric ion mediated photochemical decomposition of perfluorooctanoic acid (PFOA) by 254 nm UV light. Journal of Hazardous Materials 160, 181-186.
Wei, Z., Luo, S., Xiao, R., Khalfin, R., Semiat, R. (2017). Characterization and quantification of chromate adsorption by layered porous iron oxyhydroxide: An experimental and theoretical study. Journal of hazardous materials 338, 472-481.
Wojcieszak, D., Mazur, M., Kaczmarek, D., Domaradzki, J. (2017) Influence of doping with Co, Cu, Ce and Fe on structure and photocatalytic activity of TiO_2 nanoparticles. Materials Science-Poland 35, 725-732.
Wu, H., Wu, G., Wang, L. (2015) Peculiar porous α-Fe_2O_3, γ-Fe_2O_3 and Fe_3O_4 nanospheres: facile synthesis and electromagnetic properties. Powder Technology 269, 443-451.
Xiao, F., Li, W., Fang, L., Wang, D. (2016) Synthesis of akageneite (beta-FeOOH)/reduced

graphene oxide nanocomposites for oxidative decomposition of 2-chlorophenol by Fenton-like reaction. Journal of Hazardous Materials 308, 11-20.
Xie, Y., Qian, D., Wu, D., Ma, X. (2011) Magnetic halloysite nanotubes/iron oxide composites for the adsorption of dyes. Chemical Engineering Journal 168, 959-963.
Xu, P., Zeng, G.M., Huang, D.L., Lai, C., Zhao, M.H., Wei, Z., Li, N.J., Huang, C., Xie, G.X. (2012) Adsorption of Pb (II) by iron oxide nanoparticles immobilized Phanerochaete chrysosporium: equilibrium, kinetic, thermodynamic and mechanisms analysis. Chemical Engineering Journal 203, 423-431.
Xu, T., Zhu, R., Shang, H., Xia, Y., Liu, X., Zhang, L. (2019) Photochemical behavior of ferrihydrite-oxalate system: Interfacial reaction mechanism and charge transfer process. Water Research 159, 10-19.
Xu, T., Zhu, R., Zhu, G., Zhu, J., Liang, X., Zhu, Y., He, H. (2017) Mechanisms for the enhanced photo-Fenton activity of ferrihydrite modified with $BiVO_4$ at neutral pH. Applied Catalysis B: Environmental 212, 50-58.
Yang, H., Sun, C., Qiao, S., Zou, J., Liu, G., Smith, S.C., Cheng, H., Lu, G. (2008) Anatase TiO_2 single crystals with a large percentage of reactive facets. Nature 453, 638.
Yao, Y., Sack, T.U., Volchek, K., Brown, C.E. (2015) PFC-contaminated soil and its remediation strategies: A review. Proceedings of the 30th AMOP Techical Seminar, Environment Canada, Ottawa, ON 314-339.
Yu, Q., Zhang, R., Deng, S., Huang, J., Yu, G. (2009) Sorption of perfluorooctane sul-fonate and perfluorooctanoate on activated carbons and resin: kinetic and isotherm study. Water Research 43, 1150-1158.
Zhang, K., Huang, J., Yu, G., Zhang, Q., Deng, S., Wang, B. (2013) Destruction of perfluorooctane sulfonate (PFOS) and perfluorooctanoic acid (PFOA) by ball milling. Environmental Science & Technology 47, 6471-6477.
Zhang, Q., Deng, S., Yu, G., Huang, J. (2011) Removal of perfluorooctane sulfonate fromaqueous solution by crosslinked chitosan beads: Sorption kinetics and uptakemechanism. Bioresource Technology 102, 2265-2271.
Zhang, X., Lei, L. (2008) Preparation of photocatalytic Fe_2O_3–TiO_2 coatings in one step by metal organic chemical vapor deposition. Applied Surface Science 254(8), 2406-2412.
Zhang, Z., Wang, C.-C., Zakaria, R., Ying, J.Y. (1998) Role of particle size in nanocrystalline TiO2-based photocatalysts. The Journal of Physical Chemistry B 102(52), 10871-10878.
Zhao, C., Hu, G., Hou, D., Yu, L., Zhao, Y., Wang, J., Cao, A., Zhai, Y. (2018a) Study on the effects of cations and anions on the removal of perfluorooctane sulphonate by nanofiltration membrane. Separation and Purification Technology 202, 385-396.
Zhao, D., Cheng, J., Vecitis, C.D., Hoffmann, M.R. (2011) Sorption of perfluorochemicals to granular activated carbon in the presence of ultrasound. The Journal of Physical Chemistry A 115, 2250-2257.
Zhao, D., Liu, W. (2018) Novel high-capacity and photo-regenerable materials for efficient removal of polycyclic aromatic hydrocarbons from water U.S. Patent pending (62/452,648)
Zhao, K., Zhang, L., Wang, J., Li, Q., He, W., Yin, J.J. (2013) Surface structure-dependent molecular oxygen activation of BiOCl single-crystalline nanosheets. Journal of the American Chemical Society 135, 15750-15753.
Zhao, X., Du, P., Cai, Z., Wang, T., Fu, J., Liu, W. (2018b) Photocatalysis of bisphenol A by an easy-settling titania/titanate composite: Effects of water chemistry factors, degradation pathway and theoretical calculation. Environmental Pollution 232, 580-590.

Zhou, M., Yu, J., Cheng, B. (2006) Effects of Fe-doping on the photocatalytic activity of mesoporous TiO_2 powders prepared by an ultrasonic method. Journal of Hazardous Materials 137, 1838-1847.
Zhou, M., Yu, J., Cheng, B., Yu, H. (2005) Preparation and photocatalytic activity of Fe-doped mesoporous titanium dioxide nanocrystalline photocatalysts. Materials Chemistry and Physics 93, 159-163.

7. Appendices

7.1. Publications and Presentations

Under this intensieve study, two peer-reviewed journal papers have been publsihed, which have caught great media attention, three papers are under peer review, and three more papers are to be submitted within the next three months.

The study also resulted in one U.S. Patent application filed (62/452,648), one Ph.D. dissertation, four invited presentations, and four other presentaion at various national/international meetings or institutions. One presentation received the Best Oral Presentation Award at the 2019 ACS Spring National Meeting.

Peer reviewed journal papers:

[1] T. Xu, Y. Zhu, J. Duan, Y. Xia, T. Tong, L. Zhang, D. Zhao (2020) "Enhanced photocatalytic degradation of perfluorooctanoic acid using carbon-modified bismuth phosphate composite: Effectiveness, material synergy and roles of carbon" *Chemical Engineering Journal*, 395, 124991.

[2] J. Xu, Z. Liu, D. Zhao, N. Gao, X. Fu (2020) "Enhanced adsorption of perfluorooctanoic acid (PFOA) from water by granular activated carbon supported magnetite nanoparticles", *Science of The Total Environment*, 723, 137757.

[3] F. Li, J. Duan, S. Tian, H. Ji, Y. Zhu, Z. Wei, D. Zhao (2020) "Short-chain per- and polyfluoroalkyl substances in aquatic systems: occurrence, impacts and treatment" *Chemical Engineering Journal*, 380 (1), 122506.

[4] Z. Wei, T. Xu, D. Zhao (2019) "Treatment of per- and polyfluoroalkyl substances in landfill leachate: Status, chemistry and prospects" *Environmental Science: Water Research & Technology*, 5, 1814–1835. (**2019 Best Paper of the Journal**)

[5] T. Xu, H. Ji, Y. Gu, T. Tong, Y. Xia, L. Zhang, D. Zhao (2020) "Enhanced adsorption and photocatalytic degradation of perfluorooctanoic acid in water using iron (hydr)oxides/carbon sphere composite" *Chemical Engineering Journal*, 388, 124230.

[6] F. Li, W. Liu, X. Cheng, M. Boersma, Z. Wei, K. He, L. Blaney, D. Zhao (2019) "Concentration and destruction of perfluorooctanoic acid using a new adsorptive photocatalyst" *Water Research*, (In revision, to be resubmitted in May 2020)

[7] Z. Wei, F. Li, D. Zhao (2020) "Adsorption and photodegradation of perfluorooctanoic acid in water using a new class of indium-doped, carbon-modified titanate nanotubes" *Chemosphere*, (In final revision, to be submitted in May 2020)

[8] Y. Zhu, F. Li, T. Xu, D. Zhao (2020) "Adsorption and photodegradation of perfluorooctane sulfonate in water using a new class of gallium-doped, carbon-modified titanate nanotubes" *J. Harzardous Materials*, (In final revision, to be submitted in May 2020)

[9] J. Duan, Y. Zhu, T. Xu, and D. Zhao (2020) "Desorption and photodegradation of PFOS from a DoD site soil using oil dispersant and an adsorptive photocatalyst" *Chemosphere*, (In preparation, target submission in July 2020)

U.S. Patent:

[1] Zhao D. and Liu W. "Novel high-capacity and photo-regenerable materials for efficient removal of polycyclic aromatic hydrocarbons and PFAS from water" *US Patent* Application Number: 62/452,648

Dissertation

[1]. Li, F. (2019) A New Class of Adsorptive Photocatalysts for Enhanced Adsorption and Destruction of 4-chlorophenol and perfluorooctanoic acid (Ph.D. Dissertation). Auburn University.

Major Presentations:

[1] Li F. and Zhao D. (2019) "A new adsorptive photocatalyst for highly efficient adsorption and degradation of perfluorooctanoic acid (PFOA)" Oral presentation, The ACS Spring 2019 National Meeting, Orlando, FL, March 31 – April 4, 2019. This presentation received the **Best Oral Presentation Award.**

[2] Xu T. and Zhao D. (2019) "A new composite photocatalyst for efficient adsorption and photodegradation of perfluorooctanoic acid from water under solar light" Poster presentation, The ACS Spring 2019 National Meeting, Orlando, FL, March 31 – April 4, 2019.

[3] Zhao D., Li F., and Xu T. (2018) "A cost-effective technology for rapid and complete destruction of Per- and Polyfluoroalkyl Substances (PFAS)" Oral and Poster presentation, 2018 SERDP-ESTCP Symposium, Washington DC, November 27-29, 2018.

[4] Zhao D. et al. (2019) "Concentrate-&-Destroy: a new strategy for enhanced adsorption and destruction of per- and polyfluoroalkyl substances (PFAS) using photo-catalytically modified activated carbon (Me/TNTs@AC)" Invited seminar, Center of Environmental Toxicology and Biotechnology, Sun Yat-sen University, Guangzhou, China, July 11, 2019.

[5] Zhao D. (2019) "Concentrate-&-Destroy: a new strategy for enhanced adsorption and destruction of per- and polyfluoroalkyl substances (PFAS) using photo-catalytically modified activated carbon (Me/TNTs@AC)" Invited seminar, College of Environmental Science and Engineering, Sun Yat-sen University, Guangzhou, China, July 8, 2019.

[6] Zhao D. (2019) "Concentrate-&-Destroy: a new strategy for enhanced adsorption and destruction of PFOA and PFOS using photo-catalytically modified activated carbon (Me/TNTs@AC)" Invited seminar, Beijing University of Civil Engineering and Architecture, Beijing, China, July 4, 2019.

[7] Zhao D. (2019) "A novel concentrate-&-destroy process for efficient removal and degradation of per- and polyfluoroalkyl substances (PFAS) in water and soil using an innovative photocatalyst" Invited seminar, South China Normal University, Guangzhou, China, May 30, 2019.

[8] Li F. and Zhao D. (2018) "A high-capacity and photoregenerable composite material for efficient adsorption and photodegradation of persistent organic pollutants" 2018 Auburn Research Faculty Symposium, Auburn University, AL, October 23, 2018.

[9] Ji H. and Zhao D. (2018) “A new class of carbon-modified indium oxide nanoparticles for adsorption and photodegradation of perfluorooctanoic acid (PFOA) in water” 2018 Auburn Research Faculty Symposium, Auburn University, AL, October 23, 2018.

7.2. Supporting QA/QC Data

Table A1. QA/QC data for PFOA analyzed by LC-MS/MS at University of Maryland Baltimore County. The values in parentheses are the acceptable ranges.

QA/QC	Isotope dilution (water)	SPE (water)	Liquid extraction (solids)
Extracted Internal Standard (EIS, M8PFOA)	100%	89 ± 7%	64.4 ± 14%
Method Blank (MB)	< 0.06 µg/L	< 0.006 µg/L	< 0.6 ng/g
Laboratory Control Samples (LCS, 5 µg/L)	4.69 µg/L (3.5-6.5 µg/L)	4.40 µg/L (3.5-6.5 µg/L)	4.64 µg/L (3.5-6.5 µg/L)
Matrix Spike (MS, 5 µg/L)	-	3.67 µg/L (3.5-6.5 µg/L)	4.80 µg/L (3.5-6.5 µg/L)
Matrix Spike Duplicate (MSD, 5 µg/L)	-	4.07 µg/L (3.5-6.5 µg/L)	4.55 µg/L (3.5-6.5 µg/L)
Matrix Duplicate (MD, 5 µg/L)	4.92 µg/L (3.5-6.5 µg/L)	-	-
Post-spike (spiked at 0.2 µg/L)	0.23 µg/L (0.14-0.26 µg/L)	-	-
Spike Recovery (PFOA, n = 3)	100%	84 ± 13%	-
Matrix effects (RSD of MPFOA)	22.1% (< 30%)	16.5% (< 30%)	23.6% (< 30%)

"-" Means not measured.

Table A2. QA/QC data for PFOS analyzed by LC-MS/MS at University of Maryland Baltimore County. The values in parentheses are the acceptable ranges. Note, the linear-PFOS isomer was used here.

QA/QC	Isotope dilution (water)	SPE (water)	Liquid extraction (solids)
Extracted Internal Standard (EIS, M8PFOS)	100%	85 ± 5%	73.9 ± 9.7%
Method Blank (MB)	< 0.03 µg/L	< 0.003 µg/L	< 0.3 ng/g
Laboratory Control Samples (LCS, 5 µg/L)	4.97 µg/L (3.5-6.5 µg/L)	4.39 µg/L (3.5-6.5 µg/L)	4.24 µg/L (3.5-6.5 µg/L)
Matrix Spike (MS, 5 µg/L)	-	4.28 µg/L (3.5-6.5 µg/L)	5.24 µg/L (3.5-6.5 µg/L)
Matrix Spike Duplicate (MSD, 5 µg/L)	-	3.95 µg/L (3.5-6.5 µg/L)	4.95 µg/L (3.5-6.5 µg/L)
Matrix Duplicate (MD, 5 µg/L)	5.07 µg/L (3.5-6.5 µg/L)	-	-
Post-spike (spiked at 0.1 µg/L)	0.11 µg/L (0.07-0.13 µg/L)	-	-
Spike Recovery (PFOS, n = 3)	100%	91 ± 8%	-
Matrix effects (RSD of MPFOS)	12.9% (< 30%)	7.4% (< 30%)	13.6% (< 30%)

"-" Means not measured.

Table A3. QA/QC data for PFOA analyzed by QTOF at Auburn University. The values in parentheses are the acceptable ranges.

QA/QC	Isotope dilution (water)
Extracted Internal Standard (EIS, M8PFOA)	100%
Method Blank (MB)	< 1 µg/L
Laboratory Control Samples (LCS, 10 µg/L)	9.78 µg/L (7-13 µg/L)
Matrix Spike (MS, 10 µg/L)	9.43 (7-13 µg/L)
Matrix Spike Duplicate (MSD, 10 µg/L)	9.98 µg/L (7-13 µg/L)
Spike Recovery (PFOA, 1-100 µg/L)	93.2-102.7%
Matrix effects (RSD of M8PFOA)	23.7% (< 30%)

Table A4. QA/QC data for PFOS analyzed by QTOF at Auburn University. The values in parentheses are the acceptable ranges.

QA/QC	Isotope dilution (water)
Extracted Internal Standard (EIS, M8PFOS)	100%
Method Blank (MB)	< 1 µg/L
Laboratory Control Samples (LCS, 10 µg/L)	9.92 µg/L (7-13 µg/L)
Matrix Spike (MS, 10 µg/L)	10.34 µg/L (7-13 µg/L)
Matrix Spike Duplicate (MSD, 10 µg/L)	10.50 µg/L (7-13 µg/L)
Spike Recovery (PFOS, 1-90 µg/L)	99.6-129.7%
Matrix effects (RSD of M8PFOS)	6.2% (< 30%)

7.3. Data Used in Various Figures Related to PFOA, PFOS and F^- Concentrations.

Figure 53.

(a) Defluorination of PFOA by Fe/TNTs@AC at defferent calcination temperatures.

850 Fe/TNTs@AC.

Time (h)	F^- in solution ($\mu g\ L^{-1}$)		Volume of liquid (mL)		Defluorination (%)			Standard Error
	D1	D2	D1	D2	D1	D2	Average	
1	27	34	5.4	5.6	5.3	6.9	6.1	1.14
2	41	39	5.5	8.8	8.2	12.4	10.3	2.97
3	39	55	7.5	8.3	10.6	16.6	13.6	4.23
4	48	51	7.3	9.4	12.7	17.3	15.0	3.25

650 Fe/TNTs@AC

Time (h)	F^- in solution ($\mu g\ L^{-1}$)		Volume of liquid (mL)		Defluorination (%)			Standard Error
	D1	D2	D1	D2	D1	D2	Average	
1	39	51	11.0	10.7	15.6	19.7	17.7	2.90
2	69	77	11.9	11.7	29.8	32.7	31.2	2.03
3	97	105	11.4	12.3	39.9	46.8	43.3	4.84
4	135	164	10.4	9.6	50.7	57.1	53.9	4.49

550 Fe/TNTs@AC

Time (h)	F^- in solution ($\mu g\ L^{-1}$)		Volume of liquid (mL)		Defluorination (%)			Standard Error
	D1	D2	D1	D2	D1	D2	Average	
1	92	95	9.3	8.2	28.3	28.3	29.6	1.84
2	170	103	7.3	9.0	33.5	33.5	39.3	8.20
3	219	215	6.4	6.7	52.1	52.1	51.4	1.06
4	152	166	10.9	10.7	64.4	64.4	62.2	3.18

300 Fe/TNTs@AC

Time (h)	F^- in solution ($\mu g\ L^{-1}$)		Volume of liquid (mL)		Defluorination (%)			Standard Error
	D1	D2	D1	D2	D1	D2	Average	
1	41	7.1	7.8	7.1	11.6	15.7	13.7	2.90
2	101	10.5	5.9	10.5	21.7	24.7	23.2	2.12
3	95	10.5	8.1	10.5	27.9	34.7	31.3	4.79
4	121	7.5	7.9	7.5	34.6	41.1	37.8	4.56

(b) Defluorination of PFOA by Fe/TNTs@AC with defferent Fe contents.

5% Fe/TNTs@AC

Time (h)	F^- in solution ($\mu g\ L^{-1}$)		Volume of liquid (mL)		Defluorination (%)			Error
	D1	D2	D1	D2	D1	D2	Average	
1	38	47	6.8	6.4	9.3	10.9	10.1	1.13
2	55	51	6.1	8.8	12.12	16.3	14.2	2.94
3	71	60	8.0	6.8	20.5	14.7	17.6	4.10
4	64	81	7.6	7.7	17.7	22.5	20.1	3.39

3% Fe/TNTs@AC

Time (h)	F^- in solution ($\mu g\ L^{-1}$)		Volume of liquid (mL)		Defluorination (%)			Error
	D1	D2	D1	D2	D1	D2	Average	
1	48	51	9.5	10.0	16.5	18.4	17.5	1.34
2	105	95	8.9	10.6	34	36.4	35.2	1.70
3	124	131	10.0	10.1	44.7	47.9	46.3	2.26
4	141	165	10.6	9.7	53.9	57.8	55.9	2.76

1% Fe/TNTs@AC

Time (h)	F^- in solution ($\mu g\ L^{-1}$)		Volume of liquid (mL)		Defluorination (%)			Error
	D1	D2	D1	D2	D1	D2	Average	
1	92	95	9.3	8.2	30.9	28.3	29.6	1.84
2	170	103	7.3	9.0	45.1	33.5	39.3	8.20
3	219	215	6.4	6.7	50.6	52.1	51.4	1.06
4	152	166	10.9	10.7	59.9	64.4	62.2	3.18

0.5% Fe/TNTs@AC

Time (h)	F^- in solution ($\mu g\ L^{-1}$)		Volume of liquid (mL)		Defluorination (%)			Error
	D1	D2	D1	D2	D1	D2	Average	
1	47	51	8.6	10.1	14.6	18.6	16.6	2.83
2	64	77	11.6	10.6	26.8	29.6	28.2	1.98
3	83	96	11.5	11.4	34.6	39.8	37.2	3.68
4	107	121	10.6	10.2	41.1	44.5	42.8	2.40

Notes:

a) The 550 Fe/TNTs@AC and 1% Fe/TNTs@AC refer to the same material in the report, which was obtained at 550 °C calcination temperature and 1% Fe content.

b) F_0: Initial mass of fluorine in PFOA, which was calculated as: $100\,\frac{\mu g}{L} \times 0.04\ L \times (15 \times 19)/414 \approx 2.75\ \mu g$.

c) Defluorination was calculated as: F^- in solution × Volume of liquid / F_0 ×100%.
d) All experiments were duplicated and D1 and D2 stand for Duplicates No.1 and Duplicates No.2, respectively.
e) The error was calculated as a nominal standard deviation based on the function STDEV.S built in Excel to show the data reproducibility:

$$\text{stdev. s} = \sqrt{\frac{\Sigma(D - Daverage)^2}{(n-1)}}$$

where D: Data, Daverage: average of data, n = number of samples.

Figure 54.

(a) Adsorption kinetics of PFOA by Fe/TNTs@AC, AC and treated AC.

Fe/TNTs@AC

Time (min)	PFOA concentration (μg L^{-1})			C_t/C_0 (%)			Error
	C_0	C_{t1}[a]	C_{t2}[a]	D1	D2	Average	
5	100	2.2	5.2	2.2	5.2	3.7	1.06
10	100	2.3	3.6	2.3	3.6	2.95	0.46
30	100	2	2.6	2	2.6	2.3	0.21
60	100	1.4	1.2	1.4	1.2	1.3	0.07

[a] Analyzed by LC-MS/MS at University of Maryland Baltimore County.

AC

Time (min)	PFOA concentration (μg L^{-1})			C_t/C_0 (%)			Error
	C_0	C_{t1}[a]	C_{t2}[a]	D1	D2	Average	
5	100	73.70	73.50	73.70	73.50	73.60	0.14
30	100	51.50	57.50	51.50	57.50	54.50	4.24
120	100	26.70	26.30	26.70	26.30	26.50	0.28

a) [a] Analyzed by LC-MS/MS at University of Maryland Baltimore County.
b) C_t and C_0 refer to PFOA concentratin at time 0 and t, respectively.

Treated-AC

Time (min)	PFOA concentration (μg L^{-1})			C_t/C_0 (%)			Error
	C_0	C_{t1}[a]	C_{t2}[a]	D1	D2	Average	
5	100	43.70	39.70	43.70	39.70	41.70	2.83
30	100	25.70	26.50	25.70	26.50	26.10	0.57
120	100	13.60	19.30	13.60	19.30	16.45	4.03

[a] Analyzed by LC-MS/MS at University of Maryland Baltimore County.

(b) Photodegradation kinetics of PFOA by Fe/TNTs@AC.

Time (h)	PFOA concentration[a] (μg L^{-1})		Volume of extractant (mL)		Recovery (%)		M_t/M_0 (%)			Error
	D1	D2	D1	D2	D1	D2	D1	D2	Average	
1	64.8	62.5	27.1	34.2	100	100	43.9	53.5	48.7	6.79
2	26.9	59.4	62.2	24.4	103	85	40.6	42.6	41.6	0.71
3	24.1	24.3	56.8	62.5	86	102	39.8	37.2	38.5	0.92
4	19.0	26.1	26.2	16.5	109	89	11.4	12.1	11.75	0.25

a) [a] Analyzed by LC-MS/MS at University of Maryland Baltimore County.
b) M_0 is the initial mass of PFOA in the system, and M_t is the mass of PFOA remaining at time t, which was calculated by: PFOA concentration in extractant × Volume of extractant / Recovery Efficiency (%). Recovery efficiency was measured by spiking M8PFOA in the samples as internal standard.

(c) Defluorination kinetics of PFOA by Fe/TNTs@AC.

Time (h)	F^- in solution (μg L^{-1})		Volume of liquid (mL)		Defluorination (%)			Error
	D1	D2	D1	D2	D1	D2	Average	
1	92	95	9.3	8.2	30.9	28.3	29.6	1.84
2	170	103	7.3	9.0	45.1	33.5	39.3	8.20
3	219	215	6.4	6.7	50.6	52.1	51.4	1.06
4	152	166	10.9	10.7	59.9	64.4	62.2	3.18

Figure 55.

(a) Adsorption kinetics of PFOS by Fe/TNTs@AC.

Time (min)	PFOA concentration (μg L^{-1})			C_t/C_0 (%)			Error
	C_0	C_{t1}[a]	C_{t2}[a]	D1	D2	Average	
5	100	0.7	0.7	0.7	0.7	0.7	0.00
10	100	1.1	0.5	1.1	0.5	0.8	0.21
30	100	1.8	0.6	1.8	0.6	1.2	0.42
60	100	0.5	2.2	0.5	2.2	1.3	0.60

[a] Analyzed by LC-MS/MS at University of Maryland Baltimore County.

(b) Photodegradation kinetics of PFOS by Fe/TNTs@AC.

Time (h)	PFOS concentration[a] (μg L^{-1})		Volume of extractant (mL)		Recovery (%)		M_t/M_0 (%)			Error
	D1	D2	D1	D2	D1	D2	D1	D2	Average	
1	94.7	105	25.3	29.3	116	125	51.6	61.6	56.6	7.07
2	98.5	92	14.8	15.4	89	110	41	32.2	36.6	3.11
3	71.7	63	11.5	12.2	91	84	22.6	22.8	22.7	0.07
4	27.0	28	17.3	18.1	100	100	11.7	12.7	12.2	0.35

a) [a] Analyzed by LC-MS/MS at University of Maryland Baltimore County.
b) M_0 is the initial mass of PFOS in the system, and M_t is the mass of PFOS remaining at time t, which was calculated by: PFOS concentration in extractant × Volume of extractant / Recovery Efficiency (%). Recovery efficiency was measured by spiking M8PFOS in the samples as internal standard.

(c) Defluorination kinetics of PFOS by Fe/TNTs@AC.

Time (h)	F^- in solution (μg L^{-1})		Volume of liquid (mL)		Defluorination (%)			Error
	D1	D2	D1	D2	D1	D2	Average	
1	65	111	5.8	4.3	14.5	18.3	16.4	2.69
2	81	99	8.6	7.7	26.9	29.5	28.2	1.84
3	113	117	8.7	8.7	37.9	39.6	38.8	1.20
4	124	141	9.5	8.6	45.4	47.1	46.2	1.19

a) F_0: Initial mass of fluorine in PFOS, which was calculated as: $100\,\frac{\mu g}{L} \times 0.04\ L \times (17 \times 19)/500 \approx 2.58\ \mu g$.
b) Defluorination was calculated as: F^- in solution × Volume of liquid / F_0 ×100%.

Figure 56. Reusing Fe/TNTs@AC in six consecutive cycles of adsorption-photodegradation of PFOA.

PFOA removal.

Cycle	PFOA concentration (μg L^{-1})			PFOA removal (%)			Error
	C_0	C_{t1}[a]	C_{t2}[a]	D1	D2	Average	
fresh	100	1.4	1.2	98.6	98.8	98.7	0.07
1	100	0.6	0.8	99.4	99.2	99.3	0.07
2	100	0.6	0.3	99.4	99.7	99.55	0.11
3	100	0.6	0.7	99.4	99.3	99.35	0.04
4	100	0.7	0.6	99.3	99.4	99.35	0.04
5	100	0.6	0.9	99.4	99.1	99.25	0.11

a) [a] Analyzed by LC-MS/MS at University of Maryland Baltimore County.
b) PFOA removal is calculated as: 100 - C_t/C_0 (%)

Defluorination.

Cycle	F^- in solution (μg L^{-1})		Volume of liquid (mL)		Defluorination (%)			Error
	D1	D2	D1	D2	D1	D2	Average	
fresh	145	148	11.8	11.9	61.8	63.9	62.9	1.49
1	217	245	7.8	7.1	61.1	63.3	62.2	1.56
2	171	132	9.2	12.5	56.7	59.9	58.3	2.22
3	125	213	14.8	9.0	66.8	69.8	68.3	2.06
4	181	169	8.9	9.1	58.5	55.9	57.2	1.80
5	148	166	11.0	10.4	59.0	62.6	60.8	2.56

a) F_0: Initial mass of fluorine in PFOA, which was calculated as: $100\,\frac{\mu g}{L} \times 0.04\ L \times (15 \times 19)/414 \approx 2.75\ \mu g$.
b) Defluorination was calculated by: F^- in solution × Volume of liquid / F_0 ×100%

Figure 57.

(a) Effects of dissolved organic matters (DOM) on PFOA photodegradation using Fe/TNTs@AC.

DOM (mg L^{-1})	F^- in solution (μg L^{-1})		Volume of liquid (mL)		Defluorination (%)			Error
	D1	D2	D1	D2	D1	D2	Average	
0	71	74	19.4	17.9	49.8	47.9	48.9	1.34
0.5	112	139	8.9	7.7	36.3	38.9	37.6	1.84
1	36	87	18.9	9.0	24.7	28.3	26.5	2.55

(b) Effects of ionic strength (NaCl or $CaCl_2$) on PFOA photodegradation using Fe/TNTs@AC.

Ion strength (mM)		F^- in solution (μg L^{-1})		Volume of liquid (mL)		Defluorination (%)			Error
		D1	D2	D1	D2	D1	D2	Average	
NaCl	0	71	74	19.4	17.9	49.8	47.9	48.9	1.34
	1	70	145	17.7	9.2	44.9	48.4	46.6	2.51
	10	112	144	10.3	9.3	41.7	48.5	45.1	4.81
$CaCl_2$	1	169	162	6.6	7.6	40.3	44.8	42.6	3.18
	10	30	107	28.1	8.8	30.5	34.3	32.4	2.69

a) F_0: Initial mass of fluorine in PFOA is calculated as: $100\frac{\mu g}{L} \times 0.04\ L \times (15 \times 19)/414 \approx 2.75\ \mu g$.
b) Defluorination was calculated as: F^- in solution × Volume of liquid / F_0 ×100%

Figure 58. Effects of temperature on PFOA photodegradation using Fe/TNTs@AC.

Temperature (°C)	F^- in solution (μg L^{-1})		Volume of liquid (mL)		Defluorination (%)			Error
	D1	D2	D1	D2	D1	D2	Average	
23	71	74	19.4	17.9	49.8	47.9	48.9	1.34
65	168	168	10.8	11.2	65.8	68.4	67.1	1.84

a) F_0: Initial mass of fluorine in PFOA, which was calculated as: $100\frac{\mu g}{L} \times 0.04\ L \times (15 \times 19)/414 \approx 2.75\ \mu g$.
b) Defluorination was calculated as: F^- in solution × Volume of liquid / F_0 ×100%

Figure 59. Effect of material dosage on the mineralization of PFOA using Fe/TNTs@AC.

Dosage ($g\ L^{-1}$)	F^- in solution ($\mu g\ L^{-1}$)		Volume of liquid (mL)		Defluorination (%)			Error
	D1	D2	D1	D2	D1	D2	Average	
1	125	195	7.4	6.4	33.5	45.0	39.3	8.13
2	71	74	19.4	17.9	49.8	47.9	48.9	1.34
5	165	98	11.9	19.1	70.9	67.8	69.4	2.19
10	156	106	11.8	18.2	66.8	69.8	68.3	2.06

a) F_0: Initial mass of fluorine in PFOA, which was calculated as: $100\,\frac{\mu g}{L} \times 0.04\ L \times (15 \times 19)/414 \approx 2.75\ \mu g$.
b) Defluorination was calculated as: F^- in solution × Volume of liquid / F_0 ×100%

Figure 60. Adsorption and photodegradation of PFOS from the Willow Grove groundwater using Fe/TNTs@AC.

Adsorption

PFOS concentration ($\mu g\ L^{-1}$)			C_t/C_0 (%)			Error
C_0	C_{t1}[a]	C_{t2}[a]	D1	D2	Average	
96.1	<1.0	<1.0	99	99	99	0

a) [a] Analyzed by LC-MS/MS at University of Maryland Baltimore County.
b) " < number" means detected but not able to quantify.

Photodegradation

PFOS concentration[a] ($\mu g\ L^{-1}$)		Volume of extractant (mL)		Recover (%)		100 - M_t/M_0 (%)			Error
D1	D2	D1	D2	D1	D2	D1	D2	Average	
105	104.3	16.3	24.0	111	138	59.3	52.3	55.8	4.9

[a] Analyzed by LC-MS/MS at University of Maryland Baltimore County.

Note:
a) The initial total PFOS concentration in the groundwater was 96.1 μg/L (Linear PFOS = 57.3 μg/L, and Branched PFOS = 38.8 μg/L).
b) PFOS photodegradation (%) was calculated as: (1 - Average M_t/M_0) x 100%.

Figure 26(b). Adsorption kinetics of PFOS by Ga/TNTS@AC and AC.

Material	Time (min)	PFOS concentration ($\mu g\ L^{-1}$)			C_t/C_0 (%)			Error
		C_0	C_{t1}[a]	C_{t2}[a]	D1	D2	Average	
Ga/TNTS@AC	5	100	3.5	<1.0	3.5	<1.0	1.8	1.3
	10	100	<1.1	<1.0	<1.0	<1.0	<1.0	<1.0
	30	100	<1.0	<1.0	<1.0	<1.0	<1.0	<1.0
	60	100	<1.0	<1.0	<1.0	<1.0	<1.0	<1.0
AC	240	100	<0.5	<0.5	<0.5	<0.5	<0.5	<0.5

[a] Analyzed by LC-MS/MS at University of Maryland Baltimore County.
" <number" means detected but not able to quantify.

Figure 27(a). Photodegradation of PFOS by Ga/TNTs@AC.

Time (h)	PFOS concentration[a] ($\mu g\ L^{-1}$)		Volume of extractant (mL)		Recovery (%)		M_t/M_0 (%)			Error
	D1	D2	D1	D2	D1	D2	D1	D2	Average	
1	110.4	107.7	17.3	23.0	113.2	123.5	42.2	50.1	46.2	5.63
2	63.0	67.8	21.0	18.5	84.1	117.6	39.3	26.6	32.9	8.95
3	65.0	64.1	20.0	20.0	117.4	119.9	27.7	26.7	27.2	0.67
4	49.8	65.3	19.5	20.5	106.5	122.5	22.8	27.3	25.0	3.19

a) [a] Analyzed by LC-MS/MS at University of Maryland Baltimore County.
b) M_0 is the initial mass of PFOS in the system, and M_t is the PFOS mass remaining at time t: PFOS concentration in extractant × Volume of extractant / Recovery (%).
c) Recovery efficiency was measured using M8PFOS as the internal standard.

Figure 27(b). Defluorination of PFOS by Ga/TNTs@AC and neat AC.

Material	Time (h)	F^- in solution ($\mu g\ L^{-1}$)		Volume of liquid (mL)		Defluorination (%)			Error
		D1	D2	D1	D2	D1	D2	Average	
Ga/TNTS @AC	1	70.0	62.9	9.5	10.0	25.7	24.4	25.1	0.98
	2	183.3	183.1	5.9	6.7	41.9	47.5	44.7	3.98
	3	174.8	192.0	8.5	7.5	57.8	55.8	56.7	1.25
	4	166.6	175.1	10.0	10.0	64.5	67.8	66.2	2.32
AC	4	5.6	5.4	10.0	10.0	2.2	2.1	2.1	0.07

a) F_0: Initial mass of fluorine in PFOS, which was calculated by: $100\,\frac{\mu g}{L} \times 0.04\ L \times (17 \times 19)/500 \approx 2.58\,\mu g$.
b) Defluorination was calculated as: F^- in solution × Volume of liquid / F_0 ×100%.

Figure 28. Comparison of PFOS defluorination by Fe/TNTs@AC and Ga/TNTs@AC.

Material	F^- in solution ($\mu g\ L^{-1}$)		Volume of liquid (mL)		Defluorination (%)			Error
	D1	D2	D1	D2	D1	D2	Average	
Fe/TNTs@AC	124	141	9.5	8.6	45.4	47.1	46.2	1.19
Ga/TNTs@AC	145.3	144.3	10.0	10.0	56.2	55.9	56.0	0.17

a) F_0: Initial mass of fluorine in PFOS = 2.58 μg
b) Defluorination was calculated as: F^- in solution × Volume of liquid / F_0 ×100%.

Figure 33a.

Equilibrium adsorption of PFOA by CS, FeO, or FeO/CS after 4 h.

Material	PFOA ($\mu g\ L^{-1}$)			Adsorption efficiency (%)
	Initial	D1[a]	D2[a]	
CS	200	<LOD	<LOD	100
FeO	200	<LOD	<LOD	100
FeO/CS	200	<LOD	<LOD	100

a) [a] Analyzed by QTOF at Auburn University for preliminary material screening.
b) D1 and D2 are PFOA in the aqueous phase for duplicates 1 and 2, respectively.
c) " <LOD" means the value is lower than 1 $\mu g\ L^{-1}$.

Photodegradation of adsorbed PFOA by neat CS, FeO and FeO/CS after 4 h of solar light exposure.

Material	PFOA concentration ($\mu g\ L^{-1}$)			100 - C_t/C_0 (%)			Error
	C_0 [a]	C_{t1} [b]	C_{t2} [b]	D1	D2	Average	
CS	1280	145.0	154.6	9.4	3.4	6.40	3.00
FeO	1280	62.2	46.5	61.1	70.1	65.60	4.50
FeO/CS	1280	11.8	7.2	92.6	95.5	94.05	1.45

a) [a] Initial PFOA concentration, calculated by 200 $\mu g\ L^{-1}$ × 40 mL × 4 / 25 mL.
b) [b] analyzed by QTOF at Auburn University for preliminary material comparison.
c) D1 and D2 are PFOA in the aqueous phase for duplicates 1 and 2, respectively.
d) C_0 and C_t are PFOA concentration in the aqueous phase at time 0 and t, respectively.
e) [c] Diluted 8 times before analysis by QTOF.

Figure 33b. Defluorination kinetics of PFOA by neat CS, FeO and FeO/CS at various Fe/C molar ratios under solar light irradiation.

	Time (h)	F^- in solution ($\mu g\ L^{-1}$)		Defluorination (%)			Error
		D1	D2	D1	D2	Average	
FeO/CS (1:1)	1	126.9	118.1	14.5	13.5	14.00	0.5
	2	226.3	182.2	25.8	20.8	23.30	2.5
	3	361.1	317.0	41.2	36.2	38.70	2.5
	4	523.2	479.2	59.7	54.6	57.15	2.55
FeO/CS (0.5:1)	1	51.6	47.2	5.9	5.4	5.65	0.25
	2	103.6	108.0	11.8	12.3	12.05	0.25
	3	163.7	181.3	18.7	20.7	19.70	1.00
	4	234.2	238.6	26.7	27.2	26.95	0.25
FeO/CS (0.25:1)	1	15.7	11.3	1.8	1.3	1.55	0.25
	2	38.2	31.5	4.4	3.6	4.00	0.40
	3	60.0	51.2	6.8	5.8	6.30	0.50
	4	81.6	72.7	9.3	8.3	8.80	0.50
FeO/CS (0.125:1)	1	<LOD	1.6	0.0	0.2	0.10	0.10
	2	6.9	9.1	0.8	1.0	0.90	0.10
	3	15.7	17.9	1.8	2.0	1.90	0.10
	4	22.3	24.5	2.5	2.8	2.65	0.15
FeO	1	2.9	7.3	0.3	0.8	0.55	0.25
	2	11.3	15.7	1.3	1.8	1.55	0.25
	3	15.7	20.1	1.8	2.3	2.05	0.25
	4	21.9	26.3	2.5	3.0	2.75	0.25
CS	1	<LOD	<LOD	0	0	0	0
	2	<LOD	<LOD	0	0	0	0
	3	<LOD	<LOD	0	0	0	0
	4	<LOD	<LOD	0	0	0	0

a) Initial F concentration in PFOA (200 $\mu g\ L^{-1}$) after concentrated by 6.4 times was 876.8 $\mu g\ L^{-1}$.
b) D1 and D2 are F^- in the aqueous phase for duplicates 1 and 2, respectively.
c) LOD of the IC system for fluoride was 1 $\mu g\ L^{-1}$.

Figure 43. PFOA removal rate by FeO/CS(1:1) with or without isopropyl alcohol (ISA).

	PFOA concentration ($\mu g\ L^{-1}$)			100 - C_t/C_0 (%)			Error
	C_0 [a]	C_{t1} [b]	C_{t2} [b]	D1	D2	Average	
Without ISA	1280	11.8	7.2	92.6	95.5	94.05	1.45
With ISA	1280	55.4	68.8	30.7	14.0	22.35	8.35

a) [a] Initial PFOA concentration was calculated as 200 μg L^{-1} × 40 mL × 4 / 25 mL.
b) [b] Analyzed by QTOF at Auburn University.
c) D1 and D2 are PFOA in the aqueous phase for duplicates 1 and 2, respectively.
d) C_0 and C_t are PFOA concentration in the aqueous phase at time 0 and t, respectively.
e) [c] Diluted by 8 (without ISA) or 16 times (with ISA) before analysis by QTOF.

Figure 48. Batch equilibrium desorption of PFOS from the Willow Grove Soil using two common oil dispersants (Corexit EC9500A and SPC1000) at various concentrations and with or without NaCl.

Dispersant	D1[a] (μg L^{-1})	D2[a] (μg L^{-1})	M_e/M_0 in D1 (%)	M_e/M_0 in D2 (%)	Average	Error
EC9500 50 mg/L	47.5	38.9	30.0	42.7	36.3	9.0
EC9500 180 mg/L	48.3	48.1	28.8	29.1	28.9	0.2
EC9500 300 mg/L	55.0	49.6	19.0	26.8	22.9	5.5
EC9500 500 mg/L	39.6	39.2	41.6	42.2	41.9	0.4
EC9500 500 mg/L + 1% NaCl	21.6	25.7	68.1	62.2	65.1	4.2
SPC 1000 50 mg/L	13.4	11.8	80.3	82.6	81.5	1.6
SPC 1000 180 mg/L	22.6	13.2	66.7	80.5	73.6	9.8
SPC 1000 300 mg/L	25.8	23.4	61.9	65.5	63.7	2.5
SPC 1000 500 mg/L	31.2	18.6	54.1	72.6	63.3	13.1
EC9500 500 mg/L + 1% NaCl	17.3	16.0	74.5	76.5	75.5	1.4
DI	23.4	34.4	65.6	49.3	57.4	11.5

a) [a] Analyzed by QTOF at Auburn University.
b) D1 and D2 are PFOS in the aqueous phase for duplicates 1 and 2, respectively.
c) M_e/M_0 (%): relative PFOS mass remaining at equilibrium.
d) Initial PFOS in soil = 1507.7 ± 37.6 ng g^{-1}.

Figure 49. Successive desorption of PFOS from the Willow Grove soil using Corexit EC9500A dispersant solution.

Successive run	Time (h)	D1[a] (μg L^{-1})	D2[a] (μg L^{-1})	M_t/M_0 in D1 (%)	M_t/M_0 in D2 (%)	Average	Error
	1	33.2	35.4	28.3	24.5	26.4	2.7
1	8	36.1	35.5	22.5	23.7	23.1	0.8
	24	32.4	36.4	30.4	21.8	26.1	6.1
	25	5.7	5.5	13.8	14.3	14.0	0.3
2	32	5.0	4.8	15.3	15.8	15.5	0.4
	48	5.2	5.4	14.9	14.5	14.7	0.3
	49	1.3	1.2	12.0	12.2	12.1	0.2
3	56	1.6	1.5	11.2	11.4	11.3	0.2
	72	1.7	1.6	11.1	11.4	11.3	0.2

a) [a] Analyzed by QTOF at Auburn University.
b) D1 and D2 are PFOS in the aqueous phase for duplicates 1 and 2, respectively.
c) M_0 and M_t are PFOS mass remaining at time 0 and t, respectively.
d) Initial PFOS in soil = 1507.7 ± 37.6 ng g^{-1}.

Figure 50. Re-adsorption of desorbed PFOS by 2%-Ga/TNTs@AC.

Time (h)	D1[a] (μg L^{-1})	D2[a] (μg L^{-1})	C_t/C_0 in D1 (%)	C_t/C_0 In D2 (%)	Average	Error
0	33.2	35.4	100	100	100	0
0.08	7.5	10.0	22.0	29.3	25.6	5.2
0.5	3.2	2.5	9.3	7.2	8.3	1.5
2	1.2	0.8	3.4	2.3	2.8	0.8
4	0.7	0.7	2.0	2.0	2.0	0.0
7	0.8	0.6	2.2	1.8	2.0	0.3
24	0.8	0.6	2.3	1.9	2.1	0.3

a) [a] Analyzed by QTOF at Auburn University.
b) D1 and D2 are PFOS in the aqueous phase for duplicates 1 and 2, respectively.
c) C_0 and C_t are PFOS concentration in the aqueous phase at time 0 and t, respectively.

Figure 51. Equilibrium desorption of PFOS from the Willow Grove soil using fresh or recycled Corexit EC9500A.

	D1[a] (μg L^{-1})	D2[a] (μg L^{-1})	M_e/M_0 in D1 (%)	M_e/M_0 in D2 (%)	Average	Error
Fresh	55.0	49.6	19.0	26.8	22.9	5.5
Reuse	20.0	16.4	41.0	51.6	46.3	7.5

a) [a] Analyzed by QTOF at Auburn University.
b) D1 and D2 are PFOS in the aqueous phase for duplicates 1 and 2, respectively.
c) M_0 and M_e are PFOS mass remaining at time 0 and equilibrium, respectively.
d) Initial PFOS in soil = 1507.7 ± 37.6 ng g^{-1}.

Figure 52.

Degradation of desorbed PFOS using Ga/TNTs@AC (Ga = 2 wt.%).

Material dosage	PFOS concentration (μg L^{-1})		100 - M_t/M_0 (%)			Error
	M_{t1}[a]	M_{t2}[a]	D1	D2	Average	
5 g/L	18.3	19.4	17.5	12.4	14.95	3.61
10 g/L	15.5	15.6	30.0	29.6	29.8	0.28

a) [a] Analyzed by QTOF at Auburn University.
b) D1 and D2 are PFOS in the aqueous phase for duplicates 1 and 2, respectively.
c) M_0 and M_t are PFOS mass remaining at time 0 and t, respectively.

Defluorination of desorbed PFOS using Ga/TNTs@AC (Ga = 2 wt.%).

Material dosage	F^- in solution (μg L^{-1})		100 - C_t/C_0 (%)			Error
	C_{t1}[b]	C_{t2}[b]	D1	D2	Average	
5 g/L	17	16	13.3	11.8	12.55	1.06
10 g/L	27	26	20.0	19.2	19.6	0.57

a) D1 and D2 are PFOS in the aqueous phase for duplicates 1 and 2, respectively.
b) C_0 and C_t are F^- in solution at time 0 and t, respectively.